

# Investigating effects of sinusoidal stimulation on the retinal circuitry using a novel high-density micro-electrode array

Dissertation

zur Erlangung des Grades eines  
Doktors der Naturwissenschaften

der Mathematisch-Naturwissenschaftlichen Fakultät  
und  
der Medizinischen Fakultät  
der Eberhard Karls Universität Tübingen

vorgelegt von

**Florian Jetter**

aus Tübingen, Deutschland

März, 2020



Tag der mündlichen Prüfung: 09.12.2020

Dekan der Math.-Nat. Fakultät: Prof. Dr. T. Stehle

Dekan der Medizinischen Fakultät: Prof. Dr. B. Pichler

1. Berichterstatter: Prof. Dr. Günther Zeck

2. Berichterstatter: Prof. Dr. Cornelius Schwarz

Prüfungskommission:  
Prof. Dr. Günther Zeck  
Prof. Dr. Cornelius Schwarz  
Prof. Dr. Boris Hofmann  
Prof. Dr. Philipp Berens





# Erklärung / Declaration

Ich erkläre, dass ich die zur Promotion eingereichte Arbeit mit dem Titel ***Investigating effects of sinusoidal stimulation on the retinal circuitry using a novel high-density micro-electrode array*** selbstständig verfasst, nur die angegebenen Quellen und Hilfsmittel benutzt und wörtlich oder inhaltlich übernommene Stellen als solche gekennzeichnet habe. Ich versichere an Eides statt, dass diese Angaben wahr sind und dass ich nichts verschwiegen habe. Mir ist bekannt, dass die falsche Abgabe einer Versicherung an Eides statt mit Freiheitsstrafe bis zu drei Jahren oder mit Geldstrafe bestraft wird.

*I hereby declare that I have produced the work entitled **Investigating effects of sinusoidal stimulation on the retinal circuitry using a novel high-density micro-electrode array**, submitted for the award of a doctorate, on my own (without external help), have used only the sources and aids indicated and have marked passages included from other works, whether verbatim or in content, as such. I swear upon oath that these statements are true and that I have not concealed anything. I am aware that making a false declaration under oath is punishable by a term of imprisonment of up to three years or by a fine.*

Tübingen, den

Datum / Date

Unterschrift / Signature



# Abstract

In this work we used a novel complementary metal-oxide-semiconductor-microelectrode array (CMOS-MEA) system for electrically inducing and recording of extracellular retinal activity. The initial goal was to control signaling of specific cellular sub-populations, or functional circuits within the retina in order to increase information content as well as spatial and temporal resolution of electrically-projected images on the retina. This was done in order to enhance performance of retinal implants and electroceuticals in general. The CMOS-MEA was selected as a tool due to its capabilities of simultaneous stimulation and recording, and its high imaging quality. This work can be split into two distinct parts: In the first part properties of the CMOS-MEA system were explored. In the first experiment recording properties of the CMOS-MEA were explored, quantified and compared to other systems on the market. This work contributed to the publication “Electrical Imaging: Investigating Cellular Function at High Resolution” (Zeck, Jetter, et al. 2017). In the second experiment we tested the system’s light sensitivity and provided an explanation for induced artifacts. We also showed that artifacts induced by physiological light intensities can be suppressed sufficiently to allow extracting neuronal activity from the recorded signal. This work was published in “Optical Stimulation Effects on TiO<sub>2</sub> Sensor Dielectric Used in Capacitively-Coupled High-Density CMOS Microelectrode Array” (Bertotti, Jetter, Keil, et al. 2017). Finally we investigated properties of MEAs with native grown oxide layers compared to sputtered oxide-layers. We found that the capacitance of MEAs with native grown oxide is larger due to reduced oxide thickness, which was to be expected. Stimulation is still purely capacitive. We then obtained specific capacitance values for various frequencies.

In the second experimental part the system used to investigate effects of sinusoidal stimulation at different frequencies, intensities and durations on retinal ganglion cells (RGC). We selected three parameters vector-strength, reliability and spike rate to describe a cell’s response to sinusoidal stimulation. In the first experiment thresholds for these parameters were obtained by applying stimuli at different intensities. This was done for stimuli at 10 Hz, 25 Hz and 40 Hz. Next we tried to use observed differences in the preferred response phase between ON- and OFF-circuit RGCs in healthy mouse retina to sinusoidal stimulation to separately stimulate these circuits in blind retina. We continued to investigate effects of continuous stimulation of up to 10 min on blind mouse RGC populations. In the concluding experiment we showed that effects of stimulating with letter shaped electrodes was to large extends constrained to cells located directly above those electrodes. This experiment was designed as proof of principle and no quantitative

analysis was performed. Each of previously mentioned experiments was described in a separate subsection with its own abstract, results and discussion part. The final chapter concludes and discusses the results of all experiments in a larger context as well as highlight open questions and future work.

# Zusammenfassung

In dieser Arbeit verwendeten wir ein neuartiges CMOS-MEA System zur gleichzeitigen Stimulation und Aufnahme retinaler Ganglionzellaktivität. Die in dieser Arbeit durchgeführten Experimente lassen sich in zwei Bereiche unterteilen: Im ersten Teil wurden die Eigenschaften des CMOS Systems genauer untersucht. Dieser Teil beginnt mit einem Experiment zur genaueren Quantifizierung der Aufnahmequalität durch Bestimmung des Signal-Rausch-Verhältnisses anhand Messungen von Mäuseretina. Die Ergebnisse wurden als Teil von “Electrical Imaging: Investigating Cellular Function at High Resolution” veröffentlicht (Zeck, Jetter, et al. 2017). Im darauffolgenden Experiment wurde die Lichtsensitivität des Chips sowie deren Einfluss auf Messungen untersucht. Eine physikalische Erklärung beobachteter Effekte wurde präsentiert. Wir zeigten, dass diese Effekte auf die Messung unter physiologischen Lichtintensitäten durch den Einsatz verschiedener Filtertechniken hinreichend unterdrückt werden können und die Auswertung der Daten dadurch nur unwesentlich beeinträchtigt wird. Diese Ergebnisse wurden in der Veröffentlichung “Optical Stimulation Effects on TiO<sub>2</sub> Sensor Dielectric Used in Capacitively-Coupled High-Density CMOS Microelectrode Array” präsentiert (Bertotti, Jetter, Keil, et al. 2017). Schließlich untersuchten wir Unterschiede zwischen MEAs mit nativ gewachsener Oxidschicht und konventionellen CMOS-MEAs, welche eine 25 nm dicke Oxidschicht besitzen. Wie zu erwarten war fanden wir, dass MEAs mit nativem Oxid aufgrund der dünneren Schichtdicke eine erhöhte Kapazität besitzen. Trotz des Dickenunterschieds waren induzierte Stimulationsströme rein kapazitiv. Wir bestimmten zudem die spezifische Kapazität bei verschiedenen Frequenzen.

Im zweiten experimentellen Teil verwendeten wir das CMOS-MEA zur Untersuchung der Effekte sinusförmiger elektrischer Stimulation auf retinale Ganglienzellen (RGC) in der ex vivo Mäuseretina. Wir beschreiben die Effekte der Stimulation auf die Zellen durch die Parameter Vektorstärke, Zuverlässigkeit and Aktivität. Im ersten Experiment bestimmten wir Schwellwerte für jene Parameter bei 10 Hz, 25 Hz und 40 Hz indem wir Stimuli verschiedener Intensität applizierten und Schwellwertkurven erstellten. Im darauffolgenden Experiment versuchten wir beobachtete Unterschiede in der bevorzugten Antwortphase zwischen ON- und OFF-typ RGCs gesunder Mäuseretina zur selektiven Stimulation jener Schaltkreise in blinder Mäuseretina zu verwenden. Daraufhin untersuchten wir als nächstes Effekte kontinuierlich applizierter Sinusstimuli auf RGCs blinder Mäuseretina und beschrieben beobachtete Adaptationen. Das abschließende Experiment wurde als Machbarkeitsbeweis für die Anwendung von Sinusstimuli in Retinaimplantaten designt. Hierbei verwendeten wir buchstabenförmig angeordnete Elektroden zur

Applikation der Stimuli. Wir konnten beobachten, dass lediglich Zellen welche über den Stimulationflächen lagen aktiviert wurden. Jedes der beschriebenen Experimente wurde in einem separaten Unterkapitel beschrieben sowie Ergebnisse diskutiert. Im letzten Kapitel dieser Dissertation fassen wir die erzielten Ergebnisse zusammen und diskutieren sie experimentübergreifend. Die Thesis endet mit einem Ausblick auf zukünftige Entwicklungen in diesem Gebiet.

# Contents

<b>1</b>	<b>Introduction</b>	<b>1</b>
1.1	Motivation: The CMOS-MEA as a platform for investigating activity induced by electrical stimulation . . . . .	1
1.2	Retina . . . . .	2
1.3	Retinal Implants . . . . .	7
1.4	Electrical stimulation and extracellular recording . . . . .	9
<b>2</b>	<b>Material and Methods</b>	<b>15</b>
2.1	Biological components of the system . . . . .	15
2.1.1	Animal models . . . . .	15
2.1.2	Retina preparation . . . . .	16
2.2	Hardware . . . . .	16
2.2.1	The CMOS-MEA 5000 System . . . . .	16
2.2.2	Optical stimulation . . . . .	23
2.2.3	Stimulation current . . . . .	27
2.3	Data processing . . . . .	27
2.3.1	Artefact-reduction . . . . .	27
2.3.2	Spike-Sorting . . . . .	29
2.3.3	Circular statistics . . . . .	31
2.3.4	Reliability estimation . . . . .	33
<b>3</b>	<b>Results</b>	<b>35</b>
3.1	Electrical Imaging: Investigating Cellular Function at High Resolution . .	36
3.1.1	Abstract . . . . .	36
3.1.2	Materials and methods . . . . .	36
3.1.3	Results . . . . .	37
3.1.4	Discussion . . . . .	40
3.2	Effects of optical stimulation on CMOS-recordings . . . . .	41
3.2.1	Abstract . . . . .	42
3.2.2	Material and Methods . . . . .	42
3.2.3	Results . . . . .	43
3.2.4	Discussion . . . . .	45
3.3	CMOS MEAs with native oxide . . . . .	48
3.3.1	Material and methods . . . . .	48

3.3.2	Results . . . . .	48
3.3.3	Discussion . . . . .	51
3.4	Stimulus Response Relations to sinusoidal stimuli . . . . .	53
3.4.1	Abstract . . . . .	53
3.4.2	Material and Methods . . . . .	53
3.4.3	Results . . . . .	54
3.4.4	Chapter-discussion . . . . .	60
3.5	Circuit-specific stimulation . . . . .	66
3.5.1	Abstract . . . . .	66
3.5.2	Materials and Methods . . . . .	66
3.5.3	Results . . . . .	67
3.5.4	Chapter-discussion . . . . .	67
3.6	Effects of continuous sinusoidal stimulation . . . . .	70
3.6.1	Abstract . . . . .	71
3.6.2	Materials and Methods . . . . .	71
3.6.3	Results . . . . .	72
3.6.4	Chapter-discussion . . . . .	72
3.7	Encoding of letter-shaped objects . . . . .	78
3.7.1	Abstract . . . . .	78
3.7.2	Materials and Methods . . . . .	79
3.7.3	Results . . . . .	79
3.7.4	Chapter-discussion . . . . .	80
<b>4</b>	<b>Conclusion</b>	<b>83</b>
4.1	Summary of results . . . . .	83
4.2	CMOS-MEA as a neurotechnological tool . . . . .	84
4.3	Sinusoidal stimulation as a tool . . . . .	86
4.4	Outlook . . . . .	87
	<b>Statement of contributions</b>	<b>103</b>
	<b>Acknowledgements</b>	<b>107</b>
	<b>Appendix</b>	<b>109</b>



# Chapter 1

## Introduction

### 1.1 Motivation: The CMOS-MEA as a platform for investigating activity induced by electrical stimulation

Electroceuticals is a collective term for electrical medical devices which are implanted in the body to treat diseases or disorders (Famm et al. 2013). The name was derived to highlight the contrast to pharmaceuticals which rely on drugs. The functional principle of electroceuticals is based on the fact that most signaling processes in the human body use electrical signals. Electroceuticals therefore use electric fields to activate or inhibit specific cell populations. Examples for electroceuticals are therapies such as deep brain stimulation, sophisticated devices like retinal or cochlea implants, but also well-established devices like pacemakers. However in order to specifically address subpopulations of neurons within a certain region of the central or peripheral nervous system a good understanding of induced effects has to be developed beforehand. In this work we investigate capabilities of a CMOS-MEA for stimulation and simultaneous recoding of induced effects on neural coding which can serve as a platform for preclinical testing or basic research in this field.

Microelectrode arrays (MEA) are devices that consist of multiple electrodes which can be used for recording of neuronal activity and to apply electrical stimuli. In conventional MEAs every single electrode can be either used for recording or stimulation within the same experiment. As a result stimulation usually occurs with a loss in spatial coverage for recordings. However in recent years CMOS technology was adapted for use in MEA systems drastically increasing electrode numbers and densities. The first of these devices was invented by Eversmann et al. 2004 in 2003. Since then similar devices are used successfully by various groups (Frey et al. 2007; Ballini et al. 2014; Heer, Hafizovic, Franks, et al. 2006). Here we use a CMOS-MEA with two distinct interlaced sets of electrodes for recording and stimulation. We explore its imaging and stimulation capabilities and characterize its intrinsic physical properties.

## 1.2 Retina

The retina is a thin layer of tissue located at the inner back of our eye and is responsible for the detection of optical input, feature extraction and transmission of neuronal signals to higher brain regions. While the retina is of obvious interest and importance for the development of retinal implants, its intrinsic biological properties also make the retina an ideal tissue for investigating the effects of electrical stimulation on neurons in general. The most important advantages of the retina as a model system are:

- Cell-type diversity and layered cell-arrangement allow analysis of complex neural-networks in an controlled ex-vivo environment. There's no loss of regulatory feedback upon eye-extraction as optical data is only transmitted from the retina to the brain and not vice versa. This simplifies the experimental setup and avoids stress put on animals by in-vivo experiments.
- The retina's easy surgical accessibility simplifies extraction (see Section 2.1.2) yielding a high preparatory success-rate.
- The Retina can be kept alive in medium for several hours up to days. This allows long recording times and performing of multiple experiments using the same tissue slice. Common tissue slice-sizes used in this work are approximately one third of a retina per slice. This allows up to 6 independent experiments per sacrificed animal.

### Structure of the retina

Position and structure of the retina are schematically illustrated in Figure 1.1. The retina comprises five different signal-transducing cell-classes which are arranged in layers. Each of those cell-classes are listed in the following in subretinal to epiretinal order with their number of subtypes and their approximate total number of cells per mouse-retina.

- photoreceptors (PR), 3 subtypes, approx.  $10^8$  cells/retina
- horizontal cells (HC), no subtypes, approx.  $10^7$  cells/retina
- bipolar cells (BC), 15 subtypes (Shekhar et al. 2017), approx.  $10^7$  cells/retina
- amacrine cells(AC), 30 subtypes to 70 subtypes (estimation adapted from Masland 2012 and upper-limit estimation updated with recent results from Baden et al. 2016.), approx.  $10^7$  cells/retina
- retinal ganglion cells (RGC),  $\geq 32$  subtypes (Baden et al. 2016), approx.  $1.25 \times 10^6$  cells/retina

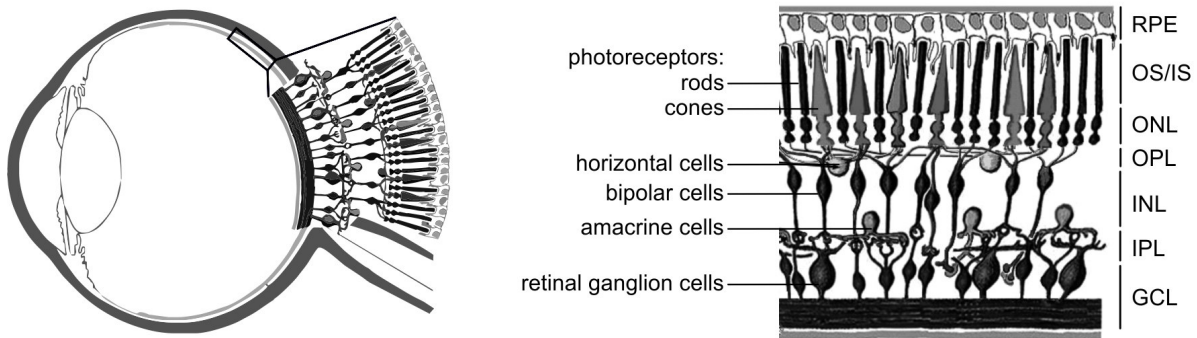


**Figure 1.1:** Schematic illustration of position of the retina in the eye (left) and the retina's layered structure (right). The retina is the innermost of three different tissue-layers of the eye. From outer to inner those are: sclera, choroid, retinal pigment epithelium, retina. The orientation of the retina is thus that the light first has to pass through the retina before it is absorbed and detected by the photoreceptors (PR). On the vertical axis the signal is transmitted from photoreceptors (rods and cones) via bipolar cells to the ganglion cells which then in turn transmit the signal to the brain. Horizontal signal transmission, modulation and feedback is provided by horizontal- and amacrine-cells. *Figure: Kolb et al. 2018*

Signal are transmitted in vertical direction by PRs, BCs and RGCs and in horizontal direction by HCs and ACs. Functional pathways are divided into ON and OFF pathway that respond to increases in illuminance with an increase (ON) or decrease (OFF) in RGC activity. The retina is limited by the retinal pigment epithelium (RPE) in sub-retinal direction and by the vitreous humour epiretinally. All different cell-types will be explained in more detail in this section. While the RPE is not part of the retina itself it will also be covered in this section due to its irreplaceable part of the visual system. For a full review on retinal cell-types see Masland 2011. We also want to highlight <https://webvision.med.utah.edu/> for offering a valuable collection of insightful articles on the retina. All numbers concerning abundance and density of cells in the mouse retina in this section are based on the work of Jeon, Strettoi, and H. Masland 1998 if not mentioned otherwise.

## Retinal pigment epithelium:

The RPE's importance for the visual perception is highlighted by its appearance in conjunction with PRs in every eye in the animal kingdom from insects, mollusca to higher vertebrates (D Lamb, Collin, and Pugh 2008). The most important tasks of the RPE are:

- Absorption of scattering light to increase spatial resolution.
- Phagocytosis of the constantly renewed outer segments of the PRs.
- Epithelial transport, i.e. the transport of nutrients, metabolites, etc. across the RPE. The RPE hereby also serves as blood-brain barrier.
- Contribution to the rods' visual cycle.
- Secretion of a large variety of factors and signaling molecules.

For a full review of the RPE see Strauss 2011.

## **Photoreceptors**

There are three different kinds of PRs in the mouse retina - rods and two types of cones. Rods contribute to approximately 97% to all PRs in the mouse retina and are mainly used for night vision and under dim light conditions. Animals like mice that are active during night therefore have a higher rod-to-cone ratio than diurnal animals. Rods were developed at later evolutionary staged than the cones. The rod-pathway therefore built-up on and feeds into the cone-pathway. This can either occur by gap-junction coupling between cones and rods or via signal transmission by rod-BCs. In the second scenario the BC output is modulated and fed into the cone-pathway by ACs. It is therefore sufficient to focus on the cone-pathway when analyzing the main properties of the signal-processing features of the retina. The remaining 3% of the PRs are cones. There are two different kind of cones in the mouse retina that differ in the wavelength sensitivity of their opsins. Genuine S cones express only S opsin with a wavelength-sensitivity peak at 360 nm while co-expressing cones express both S opsin and M opsin (peak-sensitivity at 508 nm) in a dorsal-ventral gradient (Applebury et al. 2000; Röhlich, Veen, and Szel 1994). A popular explanation for this gradient is the vertical separation into sky- and ground-components of the mouse's visual input. Short, blueish wavelengths are therefore predominant in the input to the ventral part of the retina, while the input to the dorsal part is shifted towards longer wavelengths. All PRs respond to absorption of photons by hyperpolarization, i.e. by a reduction of the glutamate release. The underlying reaction is called phototransduction (Kawamura 1995). PRs contact horizontal cells and bipolar cells in the outer nuclear layer (ONL).

## **Horizontal cells**

Horizontal-cells (HC) are located in the ONL between PRs and BPCs. While most of the mammals have two different types of HCs, mice and rats only have one type. HCs provide negative feedback between PRs. It has been proposed that HCs may also connect

to the dendrites of BCs, but this has yet to be confirmed (Herrmann et al. 2011). The role of HCs is to provide gain control which is a necessary pre-processing step for the inner retinal circuitry. HCs summarize the input over their dendritic field and subtract a proportional factor from the PRs' output. This ensures to keep the total input of the inner retinal circuitry within its functional range. It also increases the contrast between center and surround of illuminated spots also known as edge-enhancing.

## **Bipolar Cells**

There are 15 different types of BCs in the mouse retina. These BCs extract different components of the visual input. Every cone is connected to each of the different BC types. The only exceptions are the rod-BC which connects only to rods, and the blue cone BC which connects only to S-cones and is relevant for color-vision. As mentioned before the BCs encode different properties of the light input. These properties can be separated into ON/OFF and transient/sustained behavior. ON/OFF behavior is induced by the type of synapse expressed at the dendrites of the BCs while the transient/sustained behavior depends on the inactivation time of the corresponding ion-channels. The separation into ON and OFF pathway occurs in the outer plexiform layer (OPL) where the dendrites of BCs contact glutamate terminals of PRs. Modulation of the PR's glutamate release induces changes in the BCs' transmembrane-voltage. The sign of the voltage-change depends on the type of the BC's glutamate receptors. These receptors can be either ionotropic (glutamate release causes opening or closing of transmembrane ion channels) or metabotropic (glutamate release triggers signal-cascade within the cell). Cells with metabotropic receptors have a sign-inverted response, i.e. they respond to a decrease in glutamate release with an increase in the BC's transmembrane voltage and are therefore called ON-BCs. Cells with ionotropic receptors on the other hand have sign-conserving responses and are therefore called OFF-cells. BC axons contact retinal ganglion cell (RGC) dendrites at different depths of the inner plexiform layer (IPL). The depth of stratification depends on the type of information encoded in the BC. Functionality can be estimated based on two observations: First ON-cells have shorter axons while the axons of OFF-cells extend closer to the RGC layer. Second BCs with sustained responses to illuminance-changes contact RGCs closer to the edges of the IPL while transient BCs contact RGCs closer to the central part of the IPL. This is also illustrated in Figure 1.2.

## **Retinal ganglion cells**

RGCs form the final layer of signal processing neurons in the retina. RGCs contact BC axons in different layers of the IPL and thus combine the output of different types of BCs. In addition to that RGC input is also modulated by ACs. Clustering of RGCs in

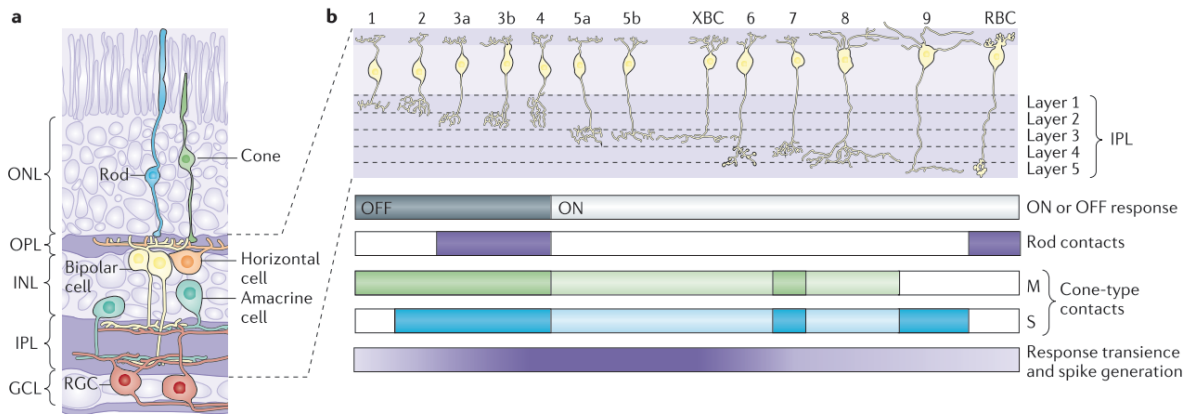


**Figure 1.2:** Illustration of the retinal circuitry (a) with focus on the stratification of BC axons (b). Different types of BCs stratify to different layers of the IPL. IPL layers therefore correlate with the distinct information patterns encoded by BCs. Axons of ON-BCs terminate in the upper, subretinal-sided layers of the IPL while axons of OFF-cells terminate in the lower, epiretinal-sided layers of the IPL. BCs with sustained response patterns to illumination-changes form synapses to RGCs in the outer layers while transient BCs form synapses in the central layers. Note that the two new types of BC discovered by Shekhar et al. 2017 were not yet included in this diagram. Source: (Euler et al. 2014)

types based on feature extraction revealed at least 33 different RGC types each encoding distinct features of the optical input (Baden et al. 2016). RGC output is encoded in action-potentials which allow high-velocity, low noise signal-transduction to the visual cortex. RGC axons exit the eye at the blind spot and form the optic nerve which transmits the neuronal output to higher brain-regions.

While the task of most RGC types is limited to signal-integration and transmission, a special RGC type which is in itself photosensitive also exists. These RGCs are called intrinsically photosensitive RGCs (ipRGC) as they contain melanopsin. ipRGCs regulate the pupillary reflex, adapt PR coupling to illuminance changes via dopamine regulation and control the circadian cycle by modulation of melatonin expression. The peak-sensitivity of these ipRGCs is in the blue regime around 480 nm (Do and Yau 2010).

## Amacrine cells

Amacrine cells are the most diverse and the experimentally hardest accessible of the retinal cell-classes. As a result they are also the least understood cell-class. ACs are of crucial importance to the specificity of the retina's ability to extract features from the optical input. They contact BCs, RGCs and other ACs and refine features extracted from BCs by putting them into context (Gollisch and Meister 2010). To perform this

task ACs do not only integrate signals laterally, but most of the ACs also integrate signals over multiple or even all layers of the IPL (MacNeil et al. 2004). The signal processing task of single AC types is very specific. Examples are the suppression of background motion-detection by widefield ACs or the direction selectivity of the starburst AC. ACs act inhibitory by GABA or glycine release and most of the AC types lack axons. The range of proposed AC types is huge and ranges from 30 subtypes to 70 subtypes (lower-bound estimation from Masland 2012 and upper-bound estimation from Baden et al. 2016).

## **1.3 Retinal Implants**

The interaction of the many different retinal cell-types provides humans with a remarkable ability perceive and respond to optical input outmatching any modern-day camera. However the leading causes of blindness in industrial countries are diseases affecting the retina. Diseases such as age-induced macula degeneration (AMD) or retinitis pigmentosa (RP) cause loss of vision by degeneration of PRs. Retinal implants take advantage of the remaining underlying cell-circuitry to restore visual percepts to patients with PR-degenerate retina. Most retinal implants rely on electrical stimulation to induce visual percepts. There are however also concepts for retinal prostheses which use neurotransmitter-releasing strategies (Safadi et al. 2003; Inayat et al. 2015) or optogenetic approaches (Doroudchi et al. 2011; Yan and Nirenberg 2018) to restore visual input. These approaches are in early developmental stages and non of them is close to application in patients. In this work we will therefore focus on approaches using electrical stimulation. For a full review on retinal prostheses see Cohen 2018. Electrical retinal implants can be classified depending on their positioning relative to the retina.

### **Epiretinal implants**

Epiretinal implants are mounted on the ILM of the retina close to the RGCs. Advantages are easy surgical accessibility, non-occluding of the retinal vasculature as well as simple monitoring of the implant through the patient's lens. Epiretinal stimulation affects RGCs directly as well as indirectly through BPC and AC excitation. Pulsed stimulation in epiretinal configuration also activates axons of passage indirectly stimulating off-center RGCs. As a result phosphenes of elliptic or arc-like shape are reported by patients (Luo et al. 2016; Nanduri et al. 2008). These effects might however be less dominant using long sinusoidal current pulses of 10 ms to 20 ms (Freeman et al. 2010). An example for an epiretinal implant is the Argus II Retinal Prosthesis System (Second Sight Medical Products, Inc., Sylmar, CA, USA) which is currently the only legally marketed retinal prostheses in the U.S.

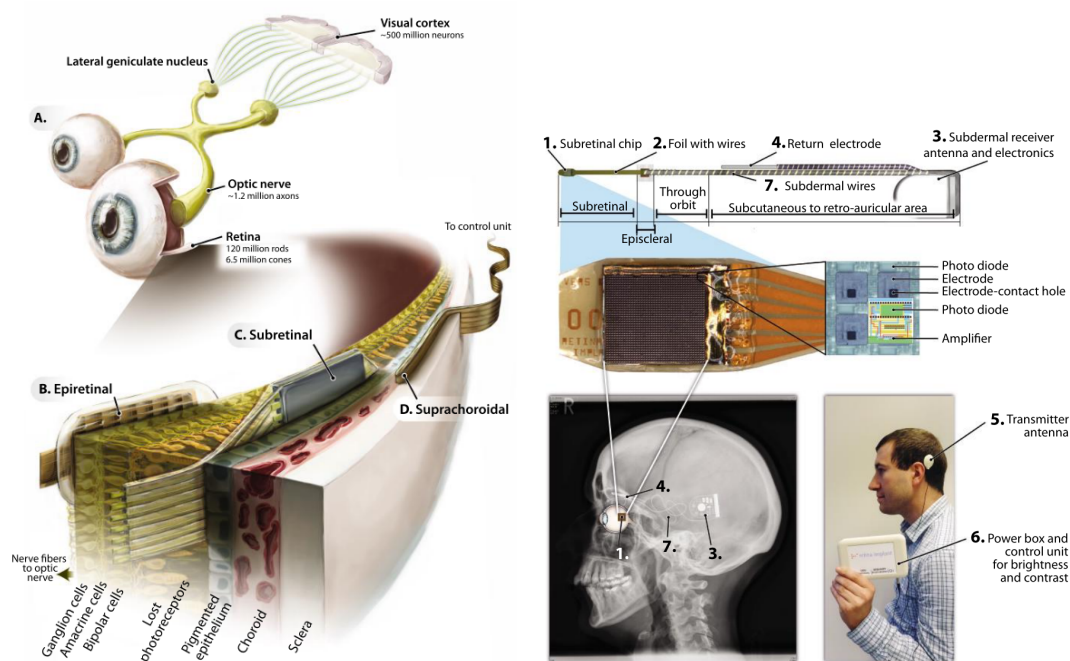


**Figure 1.3:** *Left:* Illustration of different retinal implants and where they are placed in the eye. Note that not only the chip itself but also the cable to the control unit have to be placed between the corresponding layers. *Right:* Alpha-IMS device (Retina Implant AG, Reutlingen, Germany) as an example of a subretinal implant. (1) Shows the chip which contains 1500 light-sensitive photodiodes and stimulation electrodes. Received optical stimuli are converted into an electrical voltage by photodiodes. These electrical stimuli are then amplified on-chip and applied to the retina. The chip is placed below the retina where PRs have been lost. Images projected onto the retina result in stimulation of the BPC network. These signals are then modulated by ACs, integrated by RGCs and transmitted to the visual cortex.

A receiver placed subdermally behind the ear powers and controls the electronic circuits (3). It receives power via a transmitter antenna coil (5), which is kept in place by a subdermal magnet. The receiver box connects to a subretinal foil with printed gold wires (2) using an implanted cable (7). (6) shows a battery box containing electronics which can be controlled by the patient to adjust brightness and contrast levels to the ambient light of the environment. *Source:* Zrenner 2013



## **Subretinal implants**

A second approach is to implant the prosthesis in the subretinal space between the RPE and the degenerate PR-layer. Stimulation electrodes are in close proximity to the neurons of the outer retina and provide a more precise stimulation than epiretinal implants which is closer to the natural circuitry activation provided by PRs. Additionally photosensors for subretinal implants are located directly over or close to the stimulation electrode in many implant designs (see e.g. examples at end of paragraph). This allows patients to use natural eye-movement to screen objects and helps preventing perceptual fading as experienced for statically projected images (Wilke et al. 2011). A drawback of this approach is that implants have to be very thin to fit into the subretinal space, they need to be tightly encapsulated and may partially block oxygen-transfer from choroidal to the retina (Linsenmeier and Zhang 2017). Examples for subretinal implants are the ALPHA AMS (Retina Implant AG., Reutlingen, Germany) (Stingl et al. 2013; Edwards et al. 2018) which has been approved for the European market and the Prima VRS (Pixium Vision, Paris, FR.) (Lorach et al. 2015) which is currently in clinical trial phase.

## **Suprachoroidal implants**

Implants can also be placed between sclera and choroid (Fujikado et al. 2016). This is surgically minimal invasive and reduces risks of infection or retinal detachment. The current profile of applied stimuli however spreads across the choroid reducing the overall spatial resolution of those implants. Suprachoroidal implants might still be a good approach to restore peripheral vision (Cohen 2018).

## **1.4 Electrical stimulation and extracellular recording**

As mentioned before electroceuticals use electrical currents to induce changes in the activity-patterns of neurons. For the retina RGCs form the last signal-processing layer of neurons. It is at the somata and axons of those neurons where the completely processed information exiting the eye can be obtained. Luckily the ganglion layer is well accessible after retina extraction and the activity of up to hundreds of RGCs and axons can be measured simultaneously using MEAs. RGCs use so-called action potentials (APs) to encode data transmitted to the visual cortex and it is the modulation of the extracellular potential caused by intracellular action potentials that is captured by MEA.

## The dynamics of action potentials

An AP is a stereotyped transmembrane-voltage pulse which originates in the RGC soma and is transmitted along its axon to the visual cortex. APs originate from the dynamics of voltage-gated ion-channels to changes in the transmembrane potential. These dynamics were first described in the nobel-price awarded work of Hodgkin and Huxley 1952 by Equations (1.1) - (1.4).

$$I = C_m \frac{dV_m}{dt} + \bar{g}_K n^4 (V_m - V_K) + \bar{g}_{Na} m^3 h (V_m - V_{Na}) + \bar{g}_l (V_m - V_l) \quad (1.1)$$

$$\frac{dn}{dt} = \alpha_n (V_m) (1 - n) - \beta_n (V_m) n \quad (1.2)$$

$$\frac{dm}{dt} = \alpha_m (V_m) (1 - m) - \beta_m (V_m) m \quad (1.3)$$

$$\frac{dh}{dt} = \alpha_h (V_m) (1 - h) - \beta_h (V_m) h \quad (1.4)$$

These equations are derived by describing a cell as a system of electrical components (see Figure 1.4). Main contributing ion-species for the dynamics of APs are  $\text{Na}^+$  and  $\text{K}^+$  and only those elements were taken into account for deriving those equations. In the following explanation of the equation's parameters the index  $i$  refers to  $\text{Na}^+$  and  $\text{K}^+$  respectively.  $V_m$  is the transmembrane voltage caused by different ion-concentrations in the intracellular and the extracellular medium.  $g_i = g_i(V, t)$  is the time- and voltage-dependent conductance of the corresponding ion-channels.  $V_i$  is the reversal potential or Nernst potential of the different ion-species.  $I$  is the current-density, and  $\alpha_i$  and  $\beta_i$  are voltage dependent rate parameters.  $n$ ,  $m$  and  $h$  are dimensionless parameters in the range of  $[0,1]$  that relate to the activation of  $\text{K}^+$  and  $\text{Na}^+$  channels and the inactivation of  $\text{Na}^+$  channels. The dynamics described by Equations (1.1) - (1.4) consist of the following consecutive and partially overlapping steps:

1. Depolarization of RGC  $V_m$  by  $\geq 20$  mV either by physiological input or stimulus induced.
2. Opening of  $\text{Na}^+$  channels &  $\text{Na}^+$  inflow  $\Rightarrow$  depolarizing current.
3. Opening of  $\text{K}^+$  channels &  $\text{K}^+$  outflow  $\Rightarrow$  hyperpolarizing current, also slow inactivation of  $\text{Na}^+$  channels.
4. Slow inactivation of  $\text{K}^+$  channels.
5. Ion-pumps restore initial state  $V_m \approx -65$  mV.

The right hand side of Figure 1.4 shows the model's prediction of the intracellular potential.

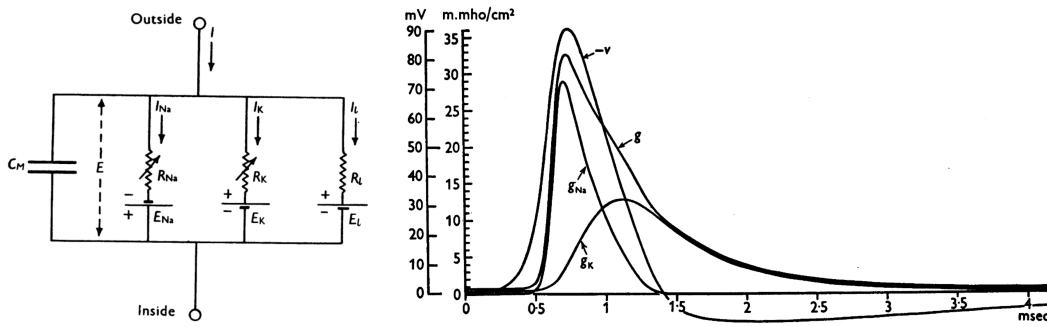


**Figure 1.4:** *Left:* Equivalent circuit diagram of a cell in the Hodgkin-Huxley-model. The cell membrane is described by a capacitance  $C_M$ .  $I_{Na}$  and  $I_K$  are ion-currents across the membrane,  $R_{Na}$  and  $R_K$  are the corresponding ion-channels while the batteries  $E_{Na}$  and  $E_K$  result from the ion-concentration gradient between intra- and extracellular medium.  $I_l$  is the leakage current over the membrane resistivity  $R_l$  driven by voltage  $E_l$ . *Right:* Dynamics of the transmembrane voltage and the conductivity of the ion-channels as predicted by the Hodgkin-Huxley-model. (Hodgkin and Huxley 1952)

## Extracellular recording of APs

APs can be recorded extracellularly by monitoring local potential changes induced by transmembrane ion-flow. This is performed by using either metal electrodes (traditional MEA) or transistors (CMOS-MEA). For conventional MEAs recorded signal shapes are slightly different to those recorded with CMOS-MEA due to intrinsic lowpass-filtering properties of the electrode-retina interface (Zeck, Jetter, et al. 2017). In our experimental setup recording is performed with a high-density CMOS-MEA. Once interfaced with the CMOS-MEA RGCs are usually as close as  $1\ \mu\text{m}$  to the electrodes. Local AP-induced potential changes couple capacitively across a thin oxide-layer into the gate-electrode of a metal-oxide-semiconductor field-effect transistor (MOSFET). This modulates the current-flow across the MOSFET and AP voltage amplitudes in the order of  $100\ \mu\text{V}$  with respect to the surrounding bath-potential can be resolved (We found common noise levels to be in the order of  $70\ \mu\text{V rms}$ \*. The term „resolved“ in this aspect refers to signal-amplitudes by which the signals can be distinguished from noise.).

## Evoking APs by electrical stimulation

The CMOS-MEA 5000 System used in our experimental setup provides stimulation electrodes interlaced on the same plane as the recording electrodes of the CMOS-MEA. This

---

\* C57BL/6J retina interfaced with CMOS-MEA,  $V_{\text{Source-Gate}} = -650\ \text{V}$ , frequency-band 300 Hz to 3000 Hz

subsection is meant to give an idea of the functional principles of electrical stimulation from a physical perspective. Figure 1.5 illustrates the setup with interfaced retina. To approximate the polarization effects of electrical stimulation on cells we take a simplified approach. A cell is approximated as a cylinder of height  $d_{\text{cell}}$  and orientation parallel to the z-axis of the system, e.g. orthogonal to the stimulation area. A stimulation-voltage  $V_s$  is applied between stimulation electrodes and reference electrode. The electric field between stimulation electrodes and reference electrode is assumed as homogeneous from the cell's perspective. The total resistivity between both electrodes is the sum of the medium's resistivity  $R_{\text{med}}$  and the retina's resistivity  $R_{\text{ret}}$ . Since  $R_{\text{ret}} \gg R_{\text{med}}$  we approximate  $R = R_{\text{med}} + R_{\text{ret}} \approx R_{\text{ret}}$  and the complete voltage drops across the thickness of the retina  $d_{\text{ret}}$ . The voltage drop across a single cell is then given by

$$\Delta V_{\text{cell}} = V_{\text{ret}} \frac{d_{\text{cell}}}{d_{\text{ret}}}.$$

We separate the cell into membrane and intracellular space (see Figure 1.5, right-hand side). The conductance of the intracellular medium should be much larger than the conductance of the membrane, so we assume for the cells resistivity  $R_{\text{membrane}} \gg R_{\text{intracellular}}$ . The voltage drop across a single membrane is then given by

$$\Delta V_{\text{membrane}} = \frac{\Delta V_{\text{cell}}}{2} = V_{\text{ret}} \frac{d_{\text{cell}}}{2d_{\text{ret}}}.$$

For capacitive stimulation the voltage drop across the retina is given by

$$\Delta V_{\text{ret}} = i_s \rho_{\text{ret}} d_{\text{ret}} = c_s \rho_{\text{ret}} d_{\text{ret}} \frac{dV_s}{dt}.$$

Putting everything together the relation between the voltage applied to the stimulation electrode and the resulting transmembrane voltage is given by

$$\Delta V_{\text{membrane}} = c_s \rho_{\text{ret}} \frac{d_{\text{cell}}}{2} \frac{dV_s}{dt}.$$

Note that the approximation is only valid if the electrical field perceived by the cell can be approximated as homogeneous. This is only the case if the total stimulation area below the cell is large compared to the cell's projective area, so  $A_{\text{stim,total}} \gg A_{\text{cell,projection}}$ . With a stimulation electrode pitch of  $32 \mu\text{m}$  and RGC soma diameters between  $20 \mu\text{m}$  to  $30 \mu\text{m}$  we estimate that this condition is true for the CMOS-MEA 5000 system for combined stimulation electrode areas  $A_{\text{stim}} \geq 4 \times 4$  and for RGCs centered above the stimulation area.

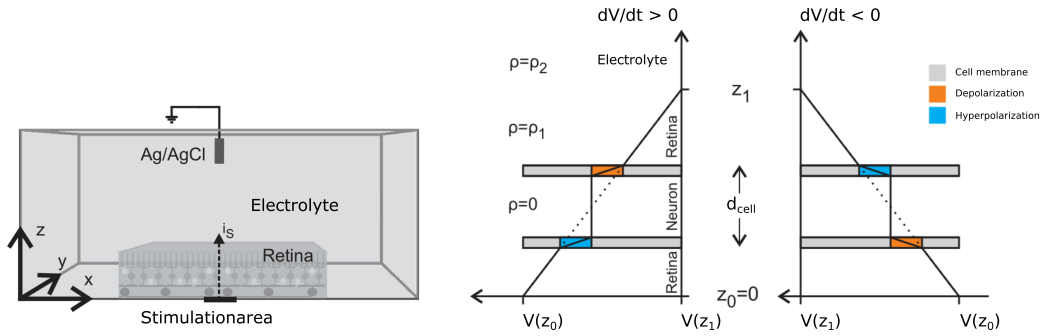


**Figure 1.5:** *Left:* Schematic illustration of the experimental setup used for electrical stimulation. Retina is placed on the CMOS-MEA in epiretinal configuration. Reference electrode is located in the electrolyte centered above the stimulation electrodes. Stimulation voltage is applied between stimulation electrodes and reference electrode. For the CMOS-system stimulation works purely capacitive, i.e. a current-flow is only induced when the applied stimulation voltage changes. Induced current flows in vertical direction along  $z$ -axis between oxide-layer and reference-ground.

*Right:* Polarization effects of electrical stimulation on the cell membrane for anodic (left) and cathodic (right) stimuli. The retina with specific resistivity  $\rho_0$  is interfaced with the CMOS-MEA at  $z_0$  and covered by an electrolyte ( $> z_1$ ) with specific resistivity  $\rho_2$ . Since  $\rho_{membrane} \gg \rho_{cytoplasm}$ , we approximate the intracellular resistivity  $\rho_{cytoplasm} = 0$ . The voltage drop across the cell is therefore reduced to the voltage drop across the cell-membranes. The sign of the transmembrane voltage depends on the sign of the voltage change  $\frac{dV}{dt}$  and the orientation of the membrane relative to the stimulation electrodes.

*Source: Eickenscheidt 2010*



# Chapter 2

## Material and Methods

### 2.1 Biological components of the system

It is unavoidable to perform experiments using acute tissue isolated from laboratory animals when interested in complex neural-networks such as the retina. While new methods like organs-on-chips and computer simulations offer promising alternatives which could replace tests on animals in some cases in the future, these methods are not in a mature state yet. Until then biological tissue extracted from animals offers the only way to closely simulate situations as experienced in human patients. This section aims at giving an introduction to the animal models used in this work and how the retina was prepared for experiments.

#### 2.1.1 Animal models

Various animal-lines for photoreceptor-degeneration are used in research to model different kinds of diseases. In retina research mouse and rat models for retinal degeneration (rd) diseases are common since murine lines are available with well-known time course of photoreceptor-degeneration. As this work is aiming at replacing common stimulus profiles for retina implants with more efficient and specific protocols, we used mouse models for PR degenerate retina diseases such as retinitis pigmentosa and age-induced macula degeneration. The mouse-models used were rd1 and rd10. In both models the gene encoding for the beta subunit of the rod phosphodiesterase 6 (Pde6b) is affected by nonsense-mutations (Chang et al. 2002). As a result both models are hallmarked by a progressive degeneration of rod PRs with a difference in the stages of retinal development when degeneration starts. In rd1 mice degeneration starts early and overlaps with retinal development. This however raises concerns that the wiring of the remaining cell-network is comparable to that of blind patients treated with retinal implants. In rd10 PR-degeneration starts at p18, when retinal neurogenesis is already completed, and is completed at p35 (Jae et al. 2013; Gargini et al. 2007). Preliminary experiments were

performed on rd1 for reasons of availability while later experiments were performed on rd10. Each experimental series was performed either on one type or the other and thus remains intrinsically consistent. The C57BL/6J mouse model (Charles River, Sulzfeld, Germany) was used as reference for healthy, wild-type mouse.

### **2.1.2 Retina preparation**

Retina preparation always followed the same protocol. Mice were dark adapted for 30 min, anesthetized by CO<sub>2</sub> and killed by cervical dislocation under dim red light (640 nm). After removal eyes were placed in a dish with carbogenated Ames medium (A 1420, Sigma Aldrich, Germany) under a dissecting microscope illuminated with dim red light. Eyes were hemisected, the vitreous body was carefully removed and the retina was peeled off the sclera. The retina was dissected into retinal portions, which extended well beyond the recording area of the electrode array. Retinal portions were mounted on the electrode array in epiretinal configuration (e.g. ganglion cell side facing the electrodes) and were used for recordings immediately. Before retina-preparation the CMOS-MEAs underwent the following treatment to achieve better adhesion of the retina. Tickopur R60 (Dr. H. Stamm GmbH, Germany) was heated to 80 °C and put into the culture chamber for 2 min. Chamber and chip surface were then rinsed with double-distilled water and dried with N<sub>2</sub> before coating the surface with poly-L-lysine hydrobromide (1 mg ml<sup>-1</sup> in ultra-pure water, 150 ku molecular weight; Sigma Aldrich, Germany). During recordings, retinae were constantly perfused with warm (35 °C to 37 °C) carbogenated Ames medium at a rate of about 5 ml min<sup>-1</sup>.

## **2.2 Hardware**

This section describes the hardware-setups used in the experiments covered in this work. Recording of neural activity and electrical stimulation was performed using the CMOS-MEA 5000 system, optical stimuli were applied combining the Rapp Optoelectronic  $\mu$ -Matrix system with the CoolLED pE-4000 system. These systems are introduced in this section in more detail.

### **2.2.1 The CMOS-MEA 5000 System**

Electrical recordings of extracellular ganglion-cell activity as well as electrical stimulation of retinal cells were performed with a high-density CMOS-based micro-electrode array called the CMOS-MEA 5000 System (Bertotti, Velychko, Dodel, Keil, Wolansky, Tillak,



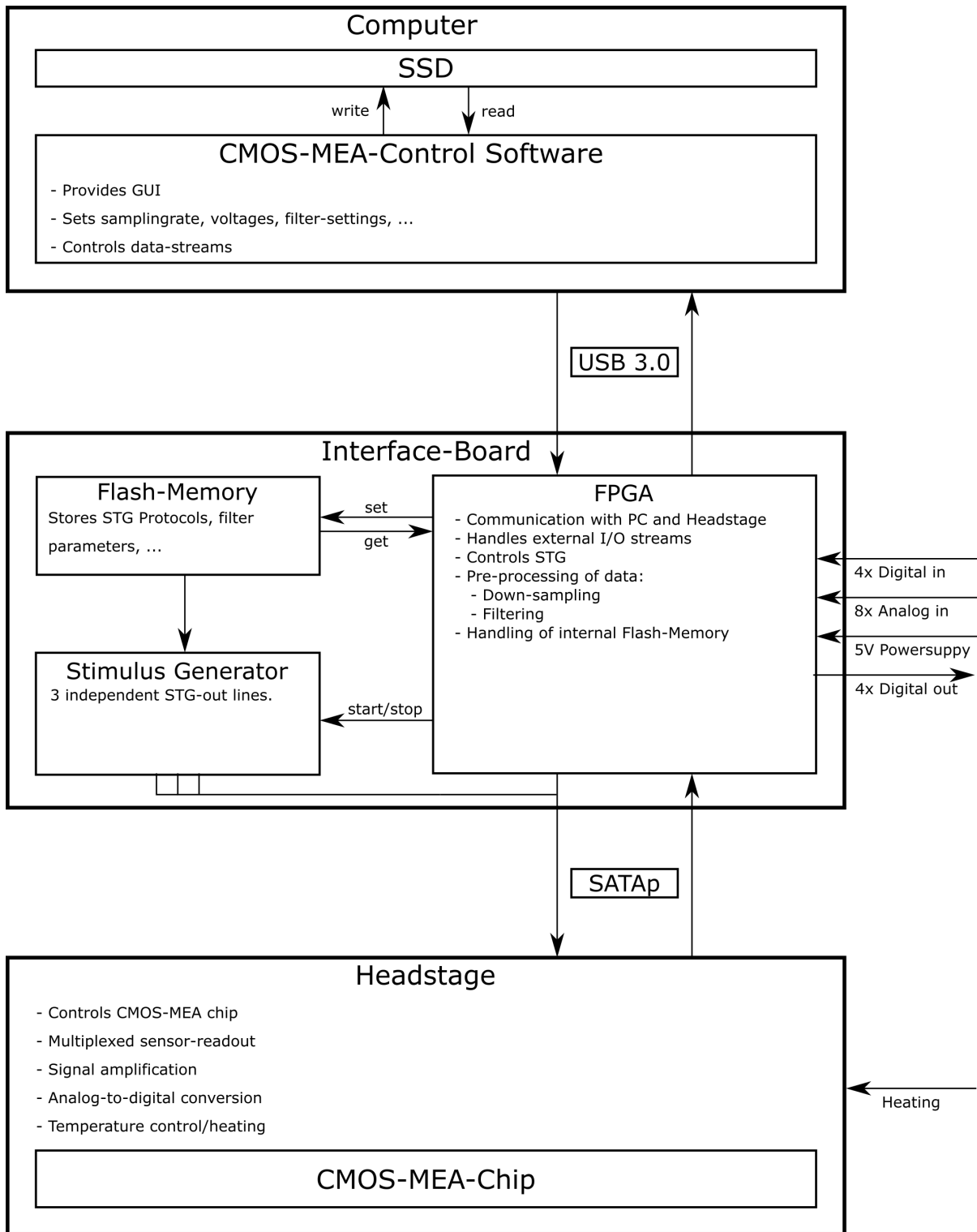


**Figure 2.1:** Simplified illustration of the signal flow within the CMOS-MEA 5000 system.

Schreiter, Grall, Jesinger, Röhler, et al. 2014). This systems allows simultaneous recording and stimulation of neuronal activity at high spatial and temporal resolution. The CMOS-MEA 5000 system consists of three major components: The CMOS-MEA chip, the Headstage (HS) and the Interface-Board (IB). While the signal flow is illustrated in Figure 2.1, the single components are covered in more detail in the following subsections in data-flow order from chip to PC.



**Figure 2.2:** Overview of the CMOS-MEA 5000's components. From top to bottom: Interface-Board, Headstage (with chip mounted), CMOS-MEA chip. Source: *MCS Multi-channel Systems*

### **The CMOS-MEA-Chip**

The CMOS-MEA chip contains  $65 \times 65$  recording electrodes and  $32 \times 32$  stimulation electrodes on an area of  $1 \text{ mm}^2$  (A  $2 \text{ mm}^2$  version of the chip also exists but was not used in this work. For this version electrode size is the same but the electrode pitch

is larger). The diameter of a single recording site is approximately  $8\ \mu\text{m}$  and the pitch between adjacent recording sites is  $16\ \mu\text{m}$ . In total they cover  $0.648\ \text{mm}^2$  which is 64,8% of the total area. CMOS-MEA electrodes are made of TiN and are covered by a thin Zr/TiO<sub>2</sub> layer. This layer protects the underlying CMOS-circuitry from chemical reactions, enhances the chip lifetime and guarantees purely capacitive coupling between electrodes and bath. The thickness of the oxide layer varied between 25 nm, 20 nm and a few nm in our experiments as a result of the on-going development process of the product (see Section 3.2). Recording electrodes act as gate-electrodes of MOSFET-sensors (see Figure 2.3). Voltage-changes above the electrode induce charge displacement along the recording electrode. This results in an electric field across the depletion region of the MOSFET which modulates its resistance and thus the current-flow. Current is then transformed into voltage to avoid a gradual decay of the recorded signal along the wires. All recording electrodes of one row share the same output line and are read out in a multiplexed manner. As a result only one recording-electrode per row can be active at the same time and other electrodes of the same row do not contribute to the row's output. On/Off-switching of active electrodes is achieved by keeping the output line on drain potential  $V_D$  while column-wise switching between two different source-potentials  $V_{S,ON}$  and  $V_{S,OFF}$ . The source-potential for non-active transistors  $V_{S,OFF}$  is equal to the drain-potential, i.e.  $V_{S,OFF} = V_D$ . As a result  $V_{SD} = 0V$  and current-flow across the transistors vanishes as does their contribution to the row's output. In our experiments the parameters for the active columns were set to  $V_{SD} = -600V$  and  $V_{SG} = -650V$ . Amplification and digitizing of the recorded data is performed on the HS and is not realized on the chip. Figure 2.3 a) explains the recording electrode circuit in more detail. The underlying circuitry of the stimulation electrodes is much simpler compared to the recording electrodes'. Each stimulation electrode is connected by a separate signal-line. The circuitry also includes two flip-flops for each stimulation electrode. This allows four different configurations: Each electrode can be either connected to one of three different STGs or be left on a floating potential. Configuration can be selected for each electrode independently. A diagram of the stimulation circuitry is shown in Figure 2.3 b).

## **The Headstage**

The HS handles the chip data-readout, applying of electrical stimuli, digitization and communication with the interface-board. It contains a specific holder for MEA-chips to directly connect to their gold-pads via metal pins and for a Ag/AgCl reference electrode. The HS reads out data from the chip's sensors in a row-wise multiplexed way at 25 kHz. This data is then amplified, converted into 14 bit ADU values and transmitted to the interface board via a SATAp link. Note however that no analog lowpass-filters are used before digitizing due to space and power-consumption/heat limitations on the chip. This results in aliasing of frequencies above 12.5 kHz which are folded into the spectrum between 0 kHz to 12.5 kHz and which results in an increase in the overall noise-level.

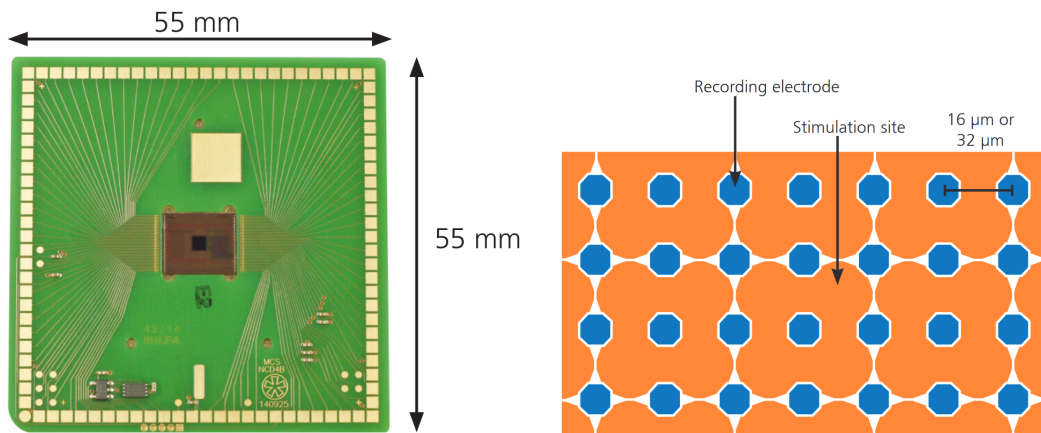


**Figure 2.3:** *Left:* Top view image of the CMOS-MEA chip ( $2 \times 2 \text{ mm}^2$  version). *Right:* Illustration of the electrode arrangement and the electrode pitch on the active area of the CMOS-MEA. Pitch between recording electrodes is  $16 \mu\text{m}$  and the pitch between adjacent stimulation electrodes is  $32 \mu\text{m}$ . Approximated diameter of recording electrodes is  $8 \mu\text{m}$ . *Source:* Multichannel Systems.

The headstage also contains a heating plate at the floor of the chip-holder which can be connected to an external controller and allows monitoring and controlling of the bath temperature.

## The Interface-Board

The interface-board (IB) is a computational unit that interfaces computer, HS and external sources. The IB exchanges and interprets commands with and from the CMOS-MEA control software, controls and accepts data from the HS, and handles input from or output to external sources. A USB 3.0 link is used for data-exchange with the computer. This exchange includes (preprocessed) sensor-data as well as commands from PC to IB. Commands can be used to change settings such as the sampling-rate or cutoff-frequencies for high- and low-pass filters, or to run automatic procedures such as adjusting ADC offset or calibrating sensors.

A SATAp link is used for communication with the HS. This link is used to transfer data from HS to IF as well as to send configuration information to the HS. This information includes voltage working-points for ADCs, bath-voltage and MOSFET working-voltages such as  $V_{\text{source-drain}}$ ,  $V_{\text{source-gate}}$  and  $V_{\text{source-bulk}}$ .

The IB contains a stimulus generator (STG) which can be used to provide transient-voltage signals to the chip's stimulation electrodes. The STG can generate up to three independent outputs simultaneously. Valid stimulation voltages are in the range of  $0 \text{ V}$  to  $3.4 \text{ V}$  and are provided at a resolution of  $1 \text{ mV}$  and a temporal resolution of

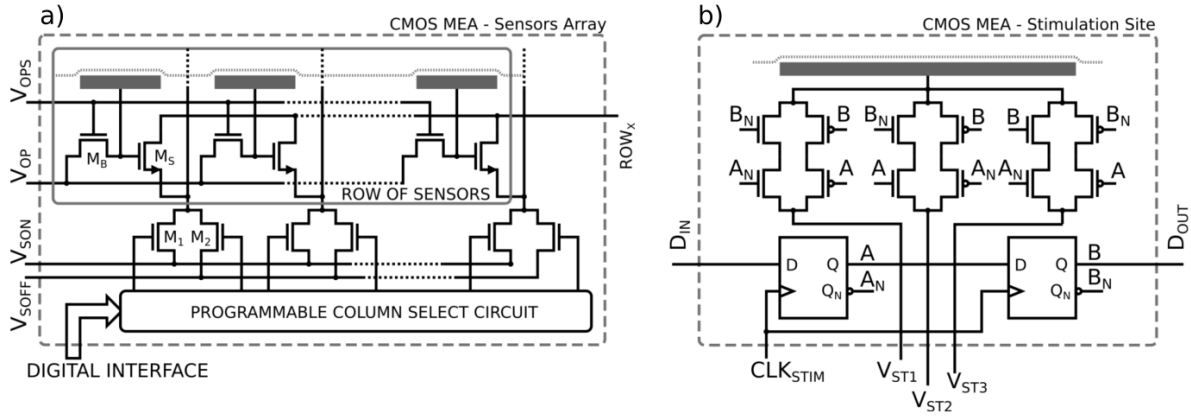


**Figure 2.4:** *a)* Diagram of the CMOS-readout circuitry. Rows are read-out in a multiplexed way. To achieve this transistors of the same row have their drain terminals shorted and share the same output. The row-output is called  $ROW_x$ , where  $x$  is the index of the row  $x \in \{1, \dots, 65\}$ . Only one column may be active at a time during regular operation. Transistors of the same column have their source terminals shorted for column-wise activating or deactivating of sensors. A column is activated by applying  $V_{SON} < V_{SOFF}$  to the source terminals through switch  $M_1$ . Every row of sensors is read out in a time-multiplexed manner, as mentioned above. Signals from all 65 rows are send off-chip as analog signals and are then continuously sampled and digitized by the off-chip hardware. In order to provide a suitable operating-point for the sensor transistors, switches  $M_B$  are closed before starting a measurement series. This sets the operating-point to  $V_{OP}$  Sensor gates are on floating potential once  $M_B$  are opened. Only then sensors can detect neuronal activity induced local potential fluctuations by capacitive crosstalk between electrolyte and gate-electrode. This leads to a modulation of the drain current of active transistors. *b)* Diagram of the CMOS-stimulation electrode circuitry. Different configurations can be set using the binary  $D_{IN}$  signal. A 2 bit signal for configuration of the flip-flop output is created by using  $D_{IN}$  of two consecutive clock-cycles. The flip-flop output is then used to set the PCMOS- and NMOS-gates accordingly, connecting the stimulation electrode to one of three different STG input signals or disconnecting it entirely, leaving it on floating-potential. *Source:* Bertotti, Velychko, Dodel, Keil, Wolansky, Tillak, Schreiter, Grall, Jesinger, Röhler, et al. 2014

10  $\mu$ s. Note that stimulation voltage is defined relative to the chip ground which is equal to  $V_{\text{source}}$  and not to the (average) bath-potential which is set to  $V_{\text{gate}}$ . Negative stimulation voltages result in significant leakage-currents and are therefore prohibited (Bertotti, Velychko, Dodel, Keil, Wolansky, Tillak, Schreiter, Grall, Jesinger, Röhler, et al. 2014). As a result the accessible stimulation voltage range is limited to a maximum of  $V_{\text{stim,max}} = 3.4 \text{ V} + V_{\text{source-gate}}$ . With the parameters  $V_{\text{source-gate}} = -650 \text{ mV}$  and  $V_{\text{source-drain}} = -600 \text{ mV}$  used in this work this is equal to  $V_{\text{stim,max}} = 2.75 \text{ V}$ .

The IB also comprises 4 additional connectors for each digital input and output as well as connectors for an 8-channel analog input. Digital channels can be used to stream or receive signals from external sources. Transition-edges are detected by the software and can be used as triggers in any logical combination of high-low transitions of the 4 digital input channels. All input streams are transmitted to the PC and can be stored in a recording file.

Processing and transmission of all data-streams is handled by an on-board FPGA. This includes but is not limited to tasks such as

- **Downsampling:** Data is always sampled at 25 kHz at the HS. If lower sampling-rates are selected, data needs to be downsampled. This is performed by the IB by extrapolation of the sensor-data to obtain voltage values for the time between data-points.
- **Filtering:** Digital filters are realized as Bessel-filters and can already be applied to the recorded data online. Cutoff-frequencies for high- and lowpass filters are selected in the control software and applied in the FPGA. Filtering-parameters are stored in the FPGA. While default options are limited to specific cutoff-frequencies, any cutoff-frequency can be realized by adjusting the stored parameters accordingly.
- **Calibration:** Digitized sensor-data received from the HS is in ADU. To allow a physical interpretation of the data a conversion factor from ADU to V is required. These conversion factors are acquired by applying a 2 mV peak-peak voltage with a frequency of 70 Hz to the reference electrode and therefore to the bath. These modulations are captured by the chip's sensors. The ADC output can then be directly related to the applied bath voltage and a conversion-factor [V/ADU] can be derived. These conversion-factors are different for each electrode as a result of small, production-based variances of the system components. Conversion-factors are usually in the order of  $10^{-6} \text{ V ADU}^{-1}$  to  $10^{-5} \text{ V ADU}^{-1}$ , where defect sensors, i.e. sensors that do not capture the bath modulation, have a factor of  $1 \text{ V ADU}^{-1}$ . Calibration values are then stored in an on-board Flash Memory.
- **Communication with Flash-Memory:** Datasets such as calibration factors or STG stimuli are stored in an on-board Flash memory. I/O operations are performed by the FPGA.

## **The CMOS-MEA Control software**

The CMOS-MEA Control software runs on a computer which is connected to the IB via USB 3.0. True to its name it allows to control signal flow and configuration of the CMOS-system from the computer using a convenient GUI, providing the interface between hardware-system and the scientist. Using the software physical parameters such as the MOSFET operating points or ADC offsets can be accessed, spatio-temporal stimulation protocols can be defined, and predefined routines such as the calibration process can be started. Sampling-rate, frequency-filters and spatial subsets of sensors can be selected according to the experimental requirements. The GUI also provides live monitoring of neuronal activity detected by the chip, allowing early estimation of signal quality or localization of neurons, and adapting of the experiment accordingly. For additional information consult the CMOS-MEA 5000 documentation on the Multichannel Systems homepage.

### **2.2.2 Optical stimulation**

Optical stimulation was used in this work for two different purposes:

1. To measure the insulation properties of the TiZr/TiO<sub>2</sub> layer under illumination at different wavelength. The results are shown and discussed in Section 3.2
2. To classify the ON-/OFF-behaviour of RGCs by calculating BIAS- and transient-indices.

The first task was addressed in cooperation with the Technical University of Berlin (Bertotti, Jetter, Keil, et al. 2017). Measurements for electrical characterization were performed in Berlin with a custom-built LED-setup. Using this setup the chip surface was illuminated with LEDs of 412 nm, 475 nm, 525 nm, 625 nm and 875 nm wavelengths. Full-width half-maximum values were 5 nm, 25 nm, 30 nm, 25 nm and 37 nm respectively and intensities of 100  $\mu\text{W mm}^{-2}$  were used.

The measurements of ex-vivo RGC activity during optical stimulation also included in Bertotti, Jetter, Keil, et al. 2017 were performed in our lab. For all these recordings as well as for the ON-/OFF-characteristics of RGCs the CoolLED pE-4000 system was used. This system is introduced in the following subsection.

#### **A multiwavelength LED light-source: The CoolLED pE-4000 system**

We used the CoolLED pE-4000 system (CoolLED Ltd., Andover, UK) as a light-source in our experiments. This system provides light at 16 different wavelength in the range of 365 nm to 770 nm. For the spectral distribution of the LEDs see Figure 2.5. Intensities

are in the range between  $\mu\text{W mm}^{-2}$  to  $\text{mW mm}^{-2}$ . The LEDs are divided into four different LED modules (LEM) also called channels. Each LEM comprises four LEDs of which only one can be active at the same time. Light emitted by the LEDs is focused by a lens and reflected into a common beam path by a Bragg-mirror. The light then exits the pE-4000 system and is transmitted to the microscope via glass-fiber. From there light is projected onto the chip or retina by the  $\mu$ -Matrix DMD device (Rapp OptoElectronic GmbH, Germany).

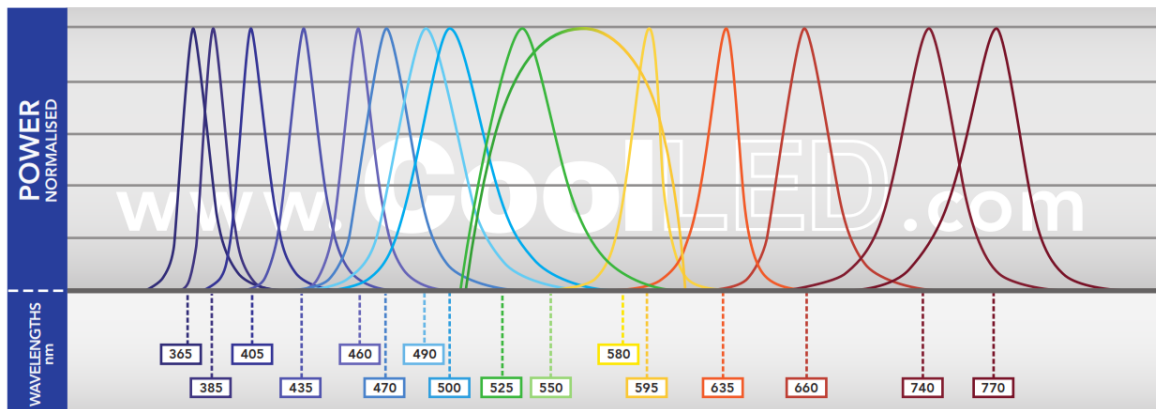


**Figure 2.5:** Illustration of the spectra of all 16 different LEDs of the pE-4000 system. Applicable wavelength range from  $\lambda = 365$  nm in the UV-regime up to  $\lambda = 770$  nm at the transition from visible light to the infrared regime. LEDs are arranged in four different columns of four LEDs each. Between those columns LEDs can be combined in any arbitrary way, allowing combinations of 256 different wavelengths-superpositions in total. *Source: CoolLED Ltd.*

## A DMD for optical stimulation: The $\mu$ -Matrix system

The  $\mu$ -Matrix DMD was used in composition with the pE-4000 system to provide spatially confined stimuli to the retina. Stimuli can be configured in the corresponding software tool with intensity-steps of single bit (on-off) up to 8 bit resolution. Single intensity-steps are always counted as fraction of the applied light-intensity provided by the pE-4000 system. E.g. an 8 bit stimulus can be defined at multiples of  $\frac{1}{256} I_{\text{source}}$ . The mirror flicker frequency or temporal resolution is up to 20 kHz for simple on/off stimuli and up to 250 Hz for 8 bit intensity-resolution. The full nominal spatial resolution of the DMD is  $1024 \text{ px} \times 768 \text{ px}$  and is in our case reduced to approximately  $380 \text{ px} \times 300 \text{ px}$  due to spatial restrictions of the arrangement of the system components. This results in a spatial resolution of approximately 500 nm using a 40x objective. The system components and their arrangement are illustrated in Figure 2.7.



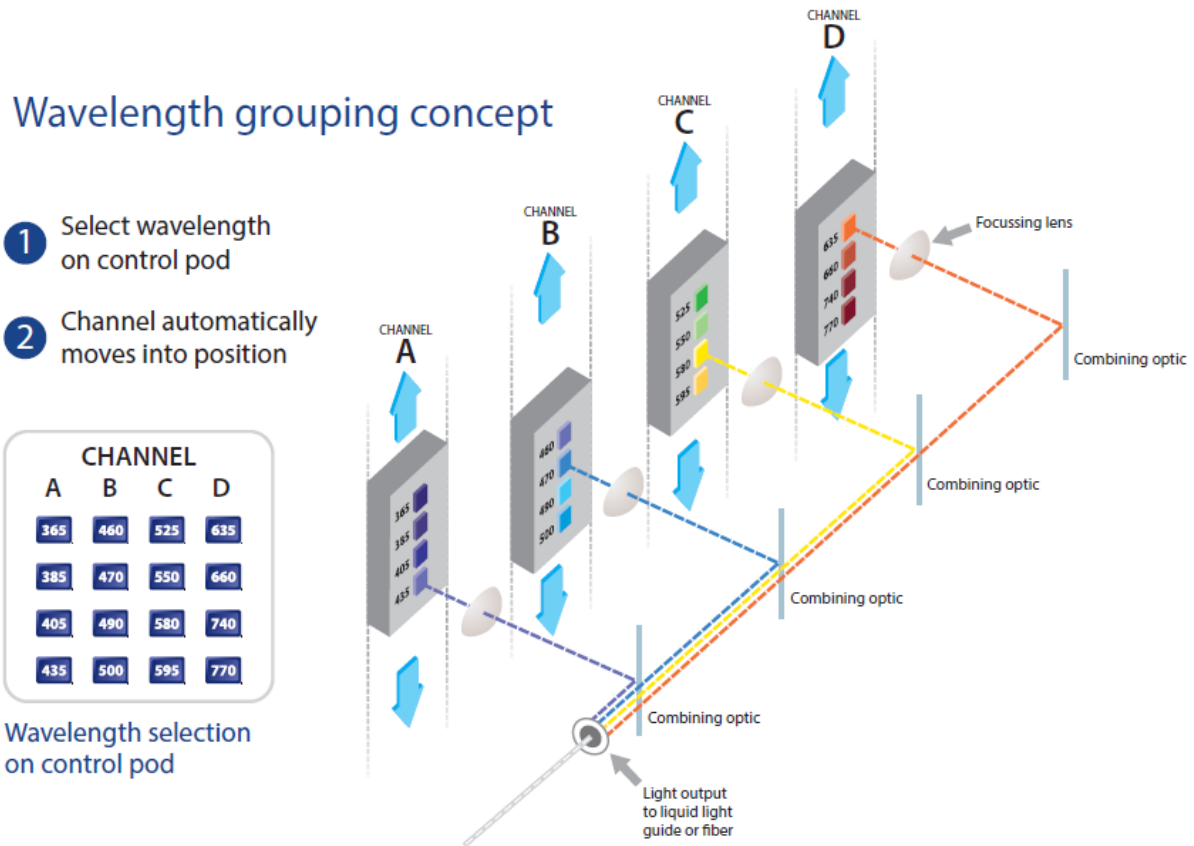


**Figure 2.6:** Schematic illustration of the optical path inside the pE-4000 system. The system houses four different LEMs. For every LEM there's a focusing lens and a Bragg-mirror. Each LEM consists of four different LEDs arranged along the vertical axis. Every time a different wavelength of a channel is selected, the LEM is mechanically moved such that the corresponding LED is on the same level as the focusing lens. Emitted light is then paralleled by the lens and reflected into the common beam path of the system. Light is then transmitted to the microscope via glass-fiber. *Source: CoolLED Ltd.*

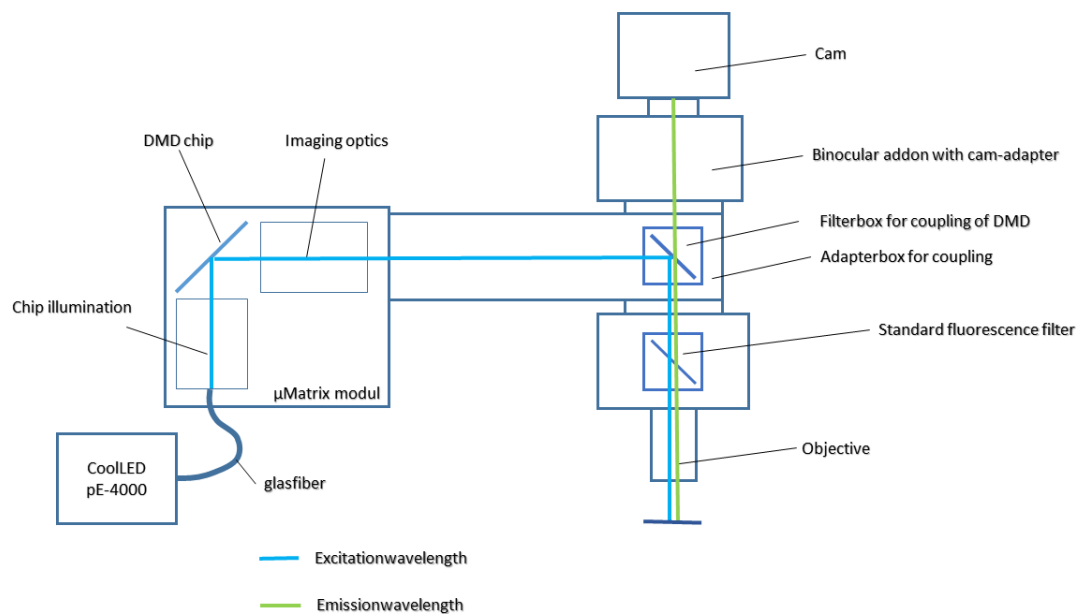


**Figure 2.7:** Illustration of the beam-path for the  $\mu$ -Matrix DMD. The CoolLED pE-4000 systems acts as a light-source for the  $\mu$ -Matrix system. The light is transmitted to the  $\mu$ -Matrix module via glas-fiber. It enters the module and illuminates the DMD-chip. Reflected light then passes the imaging optics and exits to  $\mu$ -Matrix module. It is then brought into the microscope's beam-path by mirrors placed in the adapter box. The light is then focused by an objective onto the CMOS-chip surface. A standard fluorescence filter can be used to block the excitation wavelength when the setup is used for fluorescence microscopy. Reflected/filtered light is then collected by a CCD-cam mounted on top of the microscope. Recorded signals can be monitored online using the corresponding manufacturer software. *Source: Adapted from Rapp OptoElectronic GmbH*

### 2.2.3 Stimulation current

The relation between applied voltage and resulting current-flow for a purely capacitive system is given by

$$i = \frac{I}{A} = -c \frac{dV}{dt} \quad (2.1)$$

where  $A$  is the total area of all used stimulation sites and  $c$  is the specific capacitance. To test if the CMOS-system indeed acts purely capacitive and to obtain values for the specific capacitance of the systems, we calculated the current during electric stimulation. Since the only sink in our bath is the reference electrode, we assumed that the complete current flows across this electrode to the system-ground. We connected a  $10 \Omega$  resistance  $R_{\text{drop}}$  in series to the reference electrode and measured the voltage-drop across this resistance. The wires of a coaxial cable were soldered to both sides of the added resistance  $R_{\text{drop}}$ . Voltage between both cables was amplified by a factor of  $10^3$  and transferred into the analog-channel of the interface board. Electric stimulation and recording of the analog voltage signal were started synchronously using the CMOS-MEA Control software. With  $R_{\text{drop}} \gg R_{\text{reference}}$  and  $U = R \cdot I$  we calculated the stimulation current. The stimulation protocol was adapted from pseudorandom-stimulation sinusoidal stimulation at 10 Hz, 25 Hz, 40 Hz and 100 Hz.

## 2.3 Data processing

While the CMOS-MEA 5000 system is a highly sophisticated tool for data-acquisition new tasks also arise with its imaging capabilities. Data-rates in the order of 200 MByte/s not only put constraints on computer hardware but also on the development of suitable software tools for data-analysis. A collection of analysis techniques implemented in these tools is described in this section.

### 2.3.1 Artefact-reduction

An unwanted side-effect of electrical stimulation with the CMOS-MEA 5000 setup are large modulations of the recorded signal. This is a result of the close proximity of stimulation- and recording-electrodes which allows electrical coupling effects between both nodes (Bertotti, Jetter, Dodel, et al. 2016). The artefact is a superposition of both a capacitive and a non-capacitive contribution. While capacitive-coupling effects result from parasitic capacitances within MEA, the paths for observed non-capacitive coupling effects most-likely arise between the CMOS-chip's surface and the oxide-layer. Those stimulus induced modulations are in the following referred to as artefacts. For the stimuli used in this work artefacts were usually in the order of tens of mV while AP

amplitudes were in the order of hundreds of  $\mu\text{V}$ . Artefacts had to be removed or at least reduced to a large degree before spike-detection was feasible. Different techniques were used to achieve this:

- Offset correction: All recording-electrodes have different outputs when at resting potential due to small production-based variations in their physical parameters. However recording-electrodes of one row share the same output-line and therefore the same ADC. A shifting-voltage is therefore applied to each output-line to move the mean output-signal close to the center of the working range of the ADC. Differences in the initial output between electrodes of the same row translate to variations in the voltage-offsets of corresponding recording traces. Those offsets are corrected by subtracting the mean of the first 50 frames from the each recording-trace as a first step in the processing line.
- Extraction and subtraction of baseline: In the next step the baseline, e.g. the stimulation-caused modulation, had to be separated from the recording containing the spiking-information. Either of two different strategies was used: For slow stimuli, e.g. stimuli below 100 Hz with frequency components well separated from the frequency spectra of APs, the baseline was extracted by lowpass-filtering. The lowpass-filter was a Bessel-filter of fourth order with a cutoff frequency of 300 Hz. Since this procedure still did not completely remove all of the APs' frequency components, a Savitzky-Golay-filter (Width: 51 frames, polynomial order: 2) was also applied smoothing the artefact. For stimuli where the frequency spectra of artefact and APs were not well separated a different approach was taken. Stimuli were repeatedly shown to the retina. Recorded traces were then averaged suppressing noise and the amplitude of recorded action potentials by a factor of  $\frac{1}{N}$  where  $N$  is the number of averaged traces. This worked well if the temporal correlation between stimulus induced APs was not too large and if the temporal scale of voltage changes of the stimulus was larger than the sampling frequency. In our case the shortest applied stimuli contained voltage ramps of 1 ms while the time between two samples was  $50 \mu\text{s}$ . This allowed us to extract the baseline. The baseline was then subtracted from the raw-trace regardless of the filtering method.
- Frequency-filtering: The purpose of the final filtering-step was to improve the signal-to-noise ratio (SNR) by suppressing noise components that do not overlap with the APs' frequency spectra. Applied filters were
  - A Bessel 2nd order highpass filter at 100 Hz
  - A Bessel 4th order lowpass filter at 3 kHz
  - A uniform filter with a width of 200 frames.

### **2.3.2 Spike-Sorting**

Extracting activity of single neurons from high-density CMOS-MEA recordings is a tricky task. With densities of thousands of recording-electrodes per  $\text{mm}^2$  neuronal signals of single sources are usually visible on multiple channels. At the same time due to cell-densities hundreds of cells per  $\text{mm}^2$  signals from multiple neurons might also be recorded by a single electrode. These overlays of source-signals have to be unmixed to provide a way to analyze single-cell activity. This process is called spike-sorting. The spike-sorter used in this work is part of the CMOS-MEA-Tools software distributed by Multi Channel Systems MCS GmbH, Reutlingen, Germany, which is based on the work of Leibig, Wachtler, and Zeck 2016.

The spike-sorting of pre-processed data (see Section 2.3.1) consists of several steps which are also illustrated in Figure 2.8:

- Extracting regions of interest (ROI). Sensor array is split into distinct groups of spatially connected electrodes called ROIs. ROIs can then be processed in parallel by different cores of the CPU or even on multiple computers.
- Detection of neuronal sources in ROIs by embedded Independent Component Analysis.
- Removing neuronal sources of low quality or redundant neuronal sources.

These steps will be explained in more detail now:

#### **Extract Region of Interest**

ROIs are sets of spatially connected electrodes that show a minimum of neuronal activity. A search algorithm developed for high-density CMOS-MEAs was used to determine the activity level of each sensor in the recording (Lambacher et al. 2011). The algorithm identifies events as connected subsets of electrodes that simultaneously exceed a certain SNR threshold level. The subset's spatial center of mass was considered to be the center of the event. Electrodes with activities  $\geq 3$  Hz were used as centers for initial ROIs which comprised corresponding electrode subsets.

In a next step the set of overlapping initial ROIs was consecutively merged into larger ROIs with a maximum size of 169 sensors. One by one overlapping initial ROIs were either merged if their overlap was  $\geq 0.1$  or discarded if the overlap was  $\geq 0.7$ . When all initial ROIs had been either merged or discarded the program continued with extracting of units.

## **Extracting Units from Regions of Interest**

Raw data had to be preprocessed before unmixing. Preprocessing steps included sensor-wise normalization, data embedding and Principal Component Analysis (PCA). Data embedding is used to compensate for small temporal shifts in the peak-detection for different sensors. These shifts can arise for example through differences in the signal-propagation duration from source to different sensors or from multiplexed readout. Normalization is a requirement for PCA which was applied to provide an initial estimate for the number of neurons. Dimensionality is then reduced by projecting the data to the PCA subspace spanned by the strongest Principal Components.

FastICA is applied to extract statistically independent signals (Hyvarinen 1999). The relation between preprocessed data and source signals is then given by  $Y \cdot U = S$  where  $Y$  is the preprocessed data,  $U$  the unmixing matrix and  $S$  are the source signals. So each source signal is a linear combination of all of the ROI's sensor signals. If we also include the projection of the raw data on the PCA components the relation between raw data and source signals is given by  $R \cdot P \cdot U = S$ .  $R$  is the raw-data and  $P$  the projection matrix on the contributing Principal Components. Unmixing is improved in an iterative procedure by Fast ICA until a stable, e.g. converging, solution is found. The algorithm is stopped after 1000 iterations in case of not-converging solutions resulting in non-optimal unmixing. The initial parameters of FastICA are chosen randomly so that rerunning the sorting on identical data might yield slightly different results. There is also the option to run the tool with a fixed set of parameters. However this option was not used in this work.

The extracted sources contain noise components as well as neuronal sources. Amplitude histograms of extracellular recordings of real APs should be shifted to the negative regime due to the negative voltage peak induced by  $\text{Na}^+$  inflow. For noise components a more Gaussian shape is expected. The skewness is a parameter describing the asymmetry in the tail or fatness of a distribution. A negative skewness indicates a tail or fatness in the left flank of a distribution while a positive skewness indicates a tail or fatness in the right flank of a distribution. Since ICA however cannot conserve the original sign of the source signal, all extracted signals with positive skewness are multiplied by  $-1$  since negative skewness values make more sense from the biological perspective. Therefore sources with an absolute skewness below a minimum absolute skewness of 0.2 are rejected since we cannot distinguish between positive and negative skewness. Neurons should also have a minimum spontaneous activity. Sources with less than 3 Hz are therefore considered noise and rejected.

The next step is to extract the timestamps of the extracted source signals. While we have already excluded most of the noise components the source signal might still be an overlay of different cell signals. So as a first step and in order to find all peaks in the

signal we run a simple low-threshold detection with a threshold of  $-3\sigma$ . Due to the low threshold the extracted peaks contain peaks from possible multiple neurons as well as noise peaks. The amplitude distribution of noise components is expected to have a more exponential shape while AP distributions should have more Gaussian shape. A clustering of the distribution with models consisting of an exponential noise component and zero or multiple Gaussians is performed. The best-fitting model is used for final clustering. The threshold is then set to separate the Gaussian cluster of highest amplitudes from the rest since this cluster represents the strongest neuron recorded in the source signal. Timestamps are then extracted for these Peaks.

### **Removing redundant units**

There are usually very similar units relating to the same source in the set of extracted units due to overlaps of ROIs. These units are detected and redundant units are removed in this last processing step. For this purpose units that lie within a radius of  $16\ \mu\text{m}$  from each other are checked for redundancy. This check involves two steps. First similarity of the spike trains of each pair of close units is tested by computing the corresponding alignment. The complete spike trains may be shifted by up to  $1\ \text{ms}$  and single timestamps may be shifted by up to  $500\ \mu\text{s}$ . Both units are then marked as similar if the total fraction of corresponding spikes exceeds a default threshold value of  $0.5$ .

Second similarity in STAs are tested. STAs are computed for each channel in the combined ROIs and for each channel. STAs are then compared on all channels and if the correlation coefficient exceeds a value of  $0.5$  units are marked as similar.

A unit is marked as redundant if both the spike train and the STA are considered similar. For each of those clusters of redundant units only the unit with the best separability is kept and other units are rejected. The final set of sorted units is formed by the remaining units.

### **2.3.3 Circular statistics**

The effects of sinusoidal stimulation on RGC activity cannot be analyzed with commonly used statistical techniques since these techniques do not consider the circular nature of the stimulus. Methods of circular statistic are needed to evaluate the distribution of the response-phase of RGC activity relative to applied stimulation. The CircStat-Toolbox developed by Berens 2009 is a collection of such methods. The tools used in this work were a reimplementations of this library in Python 2.7 since the original library is only available for MATLAB (The MathWorks, Inc., Natick, Massachusetts, United States) and Python versions 3 or newer. Nomenclature used in the following section is based on the official documentation to avoid confusion (Berens 2009). The focus of this analysis

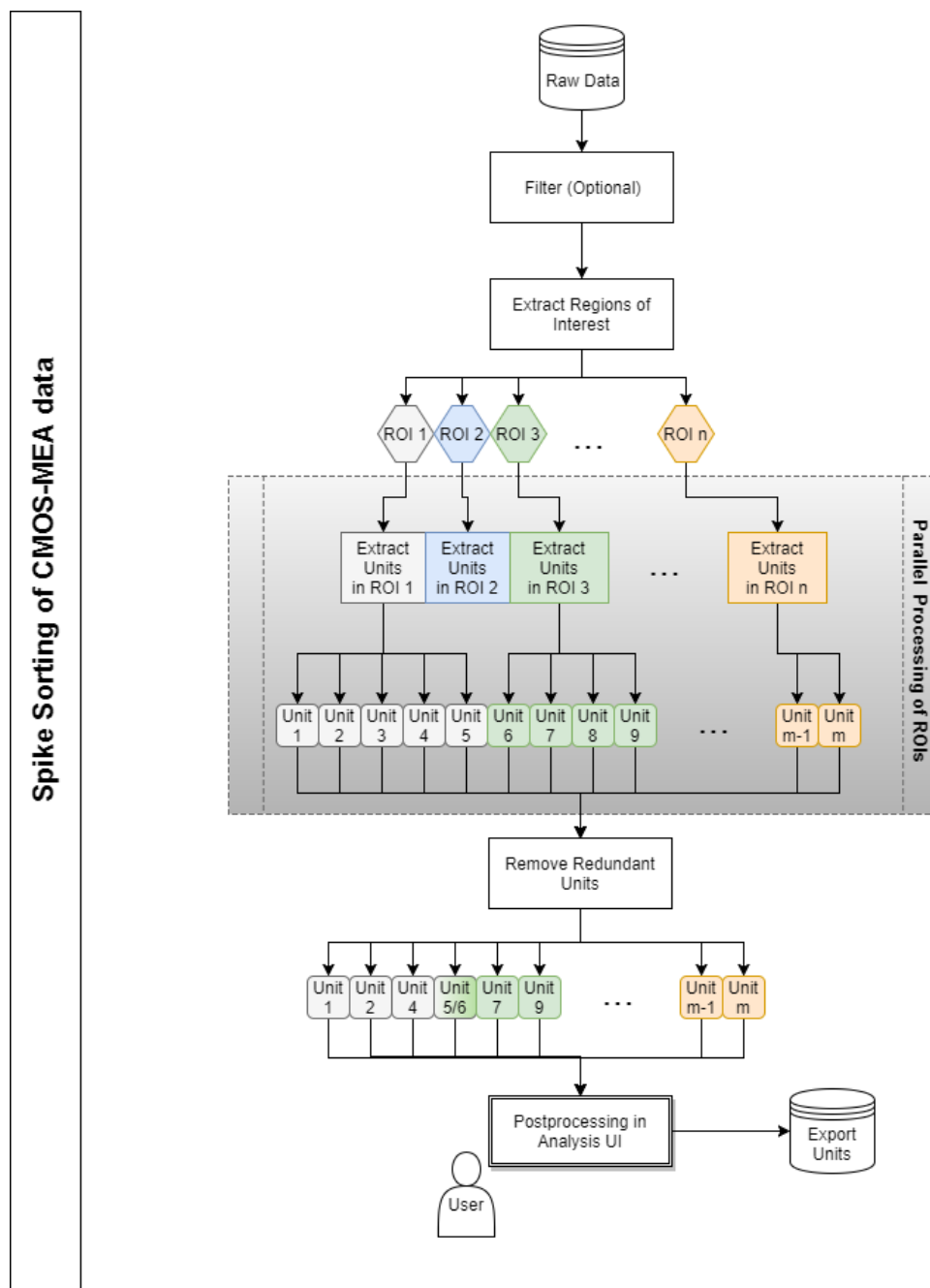


**Figure 2.8:** Illustration of the spike-sorting workflow. Filtered data was searched for neuronal activity. Initial ROIs were created from the activity distribution and merged into final ROIs. For each final ROI source signals were unmixed by convolutive independent component analysis. Units that did not fulfill certain quality-criteria were discarded and remaining units were checked for redundancy. *Source: CMOS-MEA5000-System Manual 2018*



was on the distribution of RGC-activity relative to the applied sinus. Two parameters were used to describe the distribution:

- The mean-phase  $\bar{\alpha}$  is the center of the distribution.
- The vector-strength  $\rho$  is a measurement for the width of the distribution and directly related to the variance  $S$  by  $S = 1 - \rho$ . It lives in the interval  $[0,1]$  and the closer it is to 1 the stronger a distribution is peaked around  $\bar{\alpha}$ .

To obtain those parameters we start by calculating the phase for each recorded AP relative to the stimulus. The phase is given by

$$\alpha_i = (t_i - t_{ON}) 2\pi f \pmod{2\pi} \quad (2.2)$$

where  $t_i$  is the AP's timestamp,  $t_{ON}$  is the onset of the stimulus,  $f$  is the frequency of the applied sinus and  $i = 1..N$  the index assigned to each of the  $N$  recorded APs. In a polar diagram the  $\alpha_i$  describe data-points on a circle with radius unity. However they can also be treated as 2-dimensional vectors  $r_i$  with length unity and direction  $\alpha_i$

$$r_i = \begin{pmatrix} x \\ y \end{pmatrix} = \begin{pmatrix} \cos(\alpha_i) \\ \sin(\alpha_i) \end{pmatrix}. \quad (2.3)$$

The advantage of this view of the data is that we can now use simple vector-algebra to calculate the mean-vector with respect to the circular nature of the data. The mean-vector  $\bar{r}$  is calculated as

$$\begin{aligned} \bar{r} &= \frac{1}{N} \sum_{i=0}^N r_i \\ &= \frac{1}{N} \sum_{i=0}^N \begin{pmatrix} x_i \\ y_i \end{pmatrix}. \end{aligned} \quad (2.4)$$

$\bar{r}$  yields both the center of the distribution at  $\bar{\alpha} = \arctan \frac{\bar{y}}{\bar{x}}$  and the vector-strength  $\rho = \sqrt{\bar{x}^2 + \bar{y}^2}$ .

### 2.3.4 Reliability estimation

To quantify how reliable a cell responds to an applied repetitive sinusoidal stimulus, we defined a parameter called reliability. The reliability is defined as the fraction of applied stimuli which resulted in at least one AP within a time interval  $dt$  centered around the mean-phase  $\bar{\alpha}$ . For each stimulus period a bin with a width of 20 ms centered on  $\bar{\alpha}$  was created. Reliability was now calculated as the fraction of stimulus repetitions for which

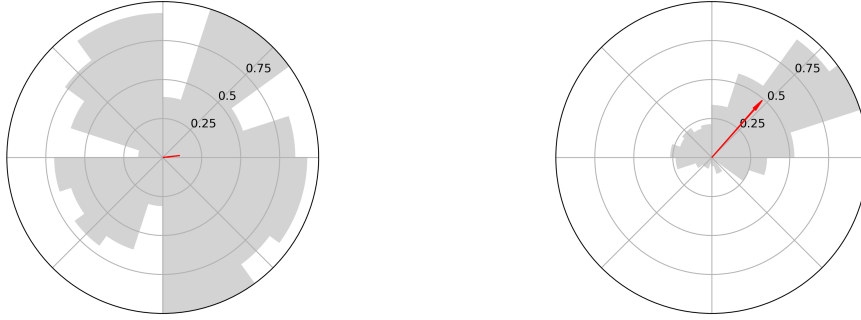


**Figure 2.9:** Illustration of Vectorstrength. Images were created from datasets of single RGC data obtained during sinusoidal electrical stimulation. Histogram of phase-values of recorded APs relative to the applied sinus is shown in grey. The red arrow is the resulting mean-vector  $\bar{r}$  calculated from data without binning. The mean-vector points in the direction of the mean-phase  $\bar{\alpha}$  and its length is the VS. *Left:* Data for low-intensity stimulation at 500 mV. Data shows no preferred phase and the VS is low. *Right:* Data from the same RGC during 2500 mV stimulation. Data shows clear preferred direction and VS is large.

the bin contained at least one AP.

$$\text{rel} = \frac{\sum_{i=1}^N f_i}{N},$$

where  $N$  is the total number of stimulus repetitions and

$$f_i = \begin{cases} 1 & \text{if } |n_i| \geq 1, n_i = \{ \text{APs} \in [\bar{t}_i - dt/2, \bar{t}_i + dt/2] \} \\ 0 & \text{else} \end{cases}.$$

Here APs is the set of timestamps of all detected APs,  $\bar{t}_i$  is the timestamp corresponding to mean-phase  $\bar{\alpha}$  of stimulus repetition  $i$ , i.e.  $\bar{t}_i = (i - 1 + \frac{\bar{\alpha}}{2\pi}) T$ , where  $T$  is the period of the applied sinus.

# Chapter 3

## Results

In recent years several high-density CMOS-MEA systems entered the market. These systems allow simultaneous recording from thousands of electrodes at spatial resolutions of tens of  $\mu\text{m}$  and temporal resolutions of tens of  $\mu\text{s}$ . Resolutions of this quality allow for the first time detailed monitoring of neural dynamics at cell compartment level. These benefits come however also at a price. Hardware of CMOS systems is more complex than those of regular MEAs, both from manufacturing and from operating perspective. Data is collected at rates of hundreds of MB/s requiring high-end computers both for data storage and for data processing. Software tools have to be optimized to work on large data-sets and new algorithms matching the properties of high-resolved data have to be developed. And as with every technological innovation not all of those aspects are well-understood from the start. It is the goal of this work to improve our understanding for several of these aspects using the CMOS-MEA 5000 system. All experiments performed in the frame of this PhD-thesis are explained in this chapter. While some experiments were focusing on testing the technical properties of the system, others were aiming at investigating effects of electrical stimulation on neuronal tissue. It is the goal of this chapter to put the single experiments in a larger context as single episodes of one big story. Each section is dedicated to one experimental series. The experimental setup, the goal and the results will all be discussed in these sections. The work presented in Section 3.1 and Section 3.2 were published as parts of articles. Own contributions will be carefully highlighted and separated from contributions of co-authors. All findings will be wrapped up in a concluding discussion in the final chapter of this work.

## **3.1 Electrical Imaging: Investigating Cellular Function at High Resolution**

### **3.1.1 Abstract**

The results presented in this section were published as parts of “Electrical Imaging: Investigating Cellular Function at High Resolution” (Zeck, Jetter, et al. 2017). Existing CMOS-MEA systems, their properties and typical or future applications were reviewed in this work. The content of this publication can be subdivided into three major parts:

1. In this first part existing CMOS-MEA systems were reviewed. CMOS-MEAs were distinguished into two groups based on the fabrication process and readout-techniques used. Properties of existing systems were summarized in a table. The section concludes by highlighting the lack of a common basis that allows to compare previously mentioned properties across systems. Quantities like noise levels are presented in the corresponding publications without mentioning used frequency-bands or pre-processing steps. A common standard would be mandatory to overcome this restriction.
2. Technical aspects affecting recording quality of CMOS-MEAs were reviewed and compared to those of MEAs. A list of contributing noise-sources was presented. Differences in the shapes and amplitudes of signals arising between conventional MEA and CMOS-MEA recordings were addressed. A novel explanation approach using intrinsic low-pass filtering properties of metal electrode MEAs motivated by the point-contact model was presented (Fromherz 2005). Recordings of both MEA types as well as obtained signal-to-noise ratios (SNR) were compared.
3. Examples of electrical imaging using CMOS-MEAs were shown motivating the application of CMOS-MEAs and their advantages over regular MEA-systems. Promising new fields of application were highlighted.

The experiments performed in the frame of this PhD thesis contributed to the second part of the publication. Performed experiments, achieved results and interpretation thereof are presented in detail.

### **3.1.2 Materials and methods**

Data from neuronal culture was recorded in the frame of “A Comprehensive Small Interfering RNA Screen Identifies Signaling Pathways Required for Gephyrin Clustering” (Wuchter et al. 2012). Cortical rat neurons were prepared following the protocol as described in “The cell adhesion molecule neurofascin stabilizes axo-axonic GABAergic

terminals at the axon initial segment.” (Kriebel et al. 2011) and plated on CMOS-MEAs as well as on a 60-channel TiN, glass-substrate electrode MEA (200  $\mu\text{m}$  electrode spacing; NMI TT). Data was recorded at day 10 *in vitro* for the CMOS-MEA and at day 21 *in vitro* for the metal electrode MEA.

Recordings of RD10 RGCs performed with CMOS-MEAs followed the protocol presented in Section 2.1.2 while those performed with metal-based TiN electrode MEAs followed the protocol described in “Inflammatory stimulation preserves physiological properties of retinal ganglion cells after optic nerve injury”(Stutzki et al. 2014). The set of filters applied to obtained data consisted of an offset-correction, a 2nd order 10 Hz high-pass and a 2nd order 3 kHz low-pass Bessel filter independent of the MEA-type used for data-acquisition. APs were identified data obtained with CMOS-MEAs using the algorithm presented by Lambacher et al. 2011. Spike-sorting was then performed using a former version of the CMOS-MEA-Tool software introduced in Section 2.3.2. The electrode with maximum signal-amplitude was identified for each unit and its SNR was calculated.

In datasets collected with TiN electrode MEAs APs were identified using a  $5\sigma$  threshold with  $\sigma = \text{median}(\text{abs}(x))/0.6745$ , where  $x$  is the data-trace of the central electrode. Spike-sorting was performed using MC\_RACK (*Multi Channel Systems MCS GmbH*). As for the CMOS-MEA data the SNR was calculated for each identified unit.

### 3.1.3 Results

Neuronal activity was clearly identified in both cell-cultures and ex-vivo retina recordings with CMOS-MEA and metal-based electrode MEA (Figure 3.2 a) - d)). Differences in the amplitude levels of AP between CMOS-MEA and metal-electrode MEA recordings were present regardless of the interfaced neuronal tissue. Amplitudes detected in conventional MEAs were in the range of 50  $\mu\text{V}$  to 100  $\mu\text{V}$  while amplitudes detected with CMOS-MEAs were in the range of 700  $\mu\text{V}$  to 1500  $\mu\text{V}$ . At the same time noise levels of MEA traces were significantly smaller compared to those of CMOS-MEAs. As a next step we analyzed SNRs of obtained datasets. The medians of the resulting SNR distributions were roughly the same for both MEA types (Figure 3.2 f)). While the histogram obtained from CMOS-MEA recordings showed a tail extending to smaller SNRs, the data obtained from TiN electrode MEAs was limited to SNRs  $\geq 5$  as a result of the  $5\sigma$  threshold used during AP detection. Next we took a closer look at the shape of recorded APs. APs recorded with TiN electrode MEAs had a broader shape, lacking the dominant peak of CMOS-MEA recorded APs. We speculated that this might be a indication for the absence of high-frequency components in the spectrum of the recorded APs. We then applied a 1 kHz low-pass filter to the CMOS recording, suppressing AP components at higher frequencies. As to be expected the result was a broader shaped signal trace. The filtered signal trace was much more similar to that of the conventional MEA recording compared to the original trace.

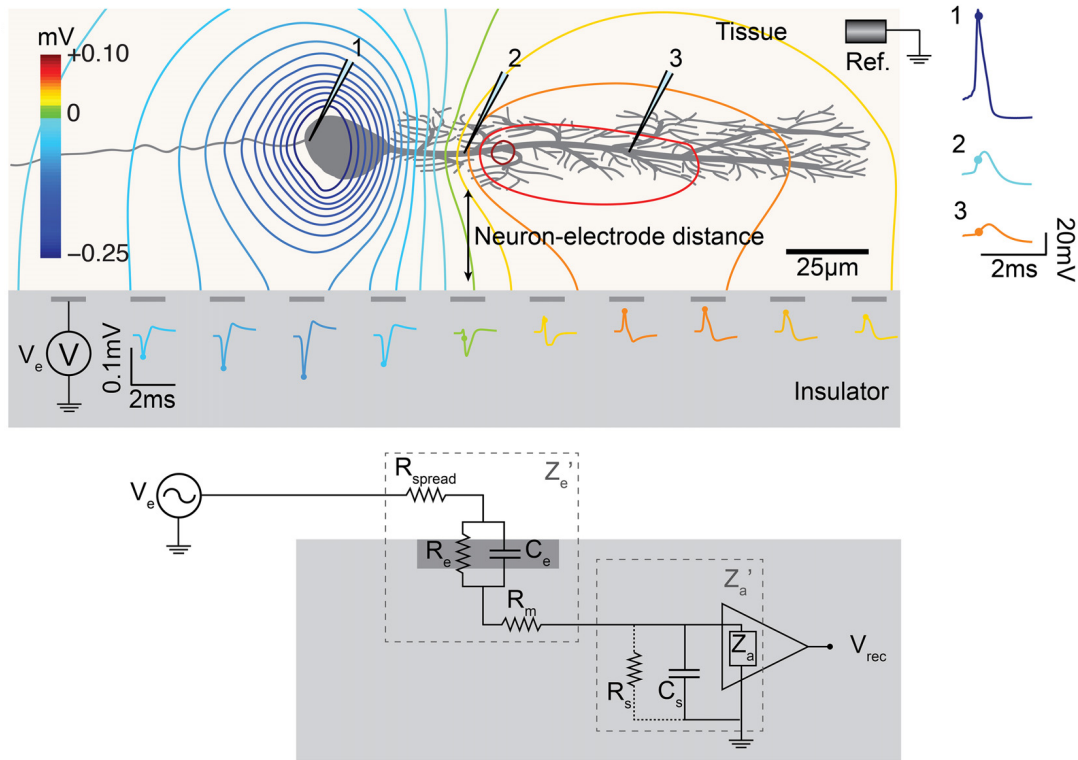


**Figure 3.1:** Illustration of generalized electrode-neuron interface (Obien et al. 2015). Interface is split into "fluid"- and "metal"-side. The potential  $V_e$  at the electrode on the "fluid"-side (upper image) can be described using volume conductor theory. Assuming the MEA surface to be an insulator allows applying of Coulomb's Law to solve the potential at any point on the MEA surface. The signal amplitude measured at the electrode is directly related to the distance between neuron and recording electrode. Novel systems with high spatial resolution, such as the CMOS-MEA 5000 system, allow recording of APs at different sites of the neuron simultaneously. The polarity of the recorded signal depends on the compartment of the cell where  $V_e$  originates. The lower diagram describes the voltage measured at the electrode using an equivalent-circuitry of the recording system. The voltage measured at the electrode on the "metal"-side is shaped by the properties of the electrode-electrolyte interface. These parameters are represented by the effective electrode impedance  $Z'_e$ .  $R_{spread}$  is the spreading-resistance, which a current spreading from electrode to electrolyte "sees".  $R_e$  and  $C_e$  are resistance and capacitance of the electric double layer forming at the recording electrode.  $R_m$  is the resistance of the metallic part of the recording electrode.  $Z'_a$  is the effective amplifier input impedance. It consists of the actual amplifier impedance  $Z_a$ , the shunt resistance  $R_s$  (which is usually negligible) and the shunt capacitance  $C_s$ . While  $C_s$  is usually small, it might in composition with  $Z'_e$  introduce a low-pass filtering effect to the circuitry.

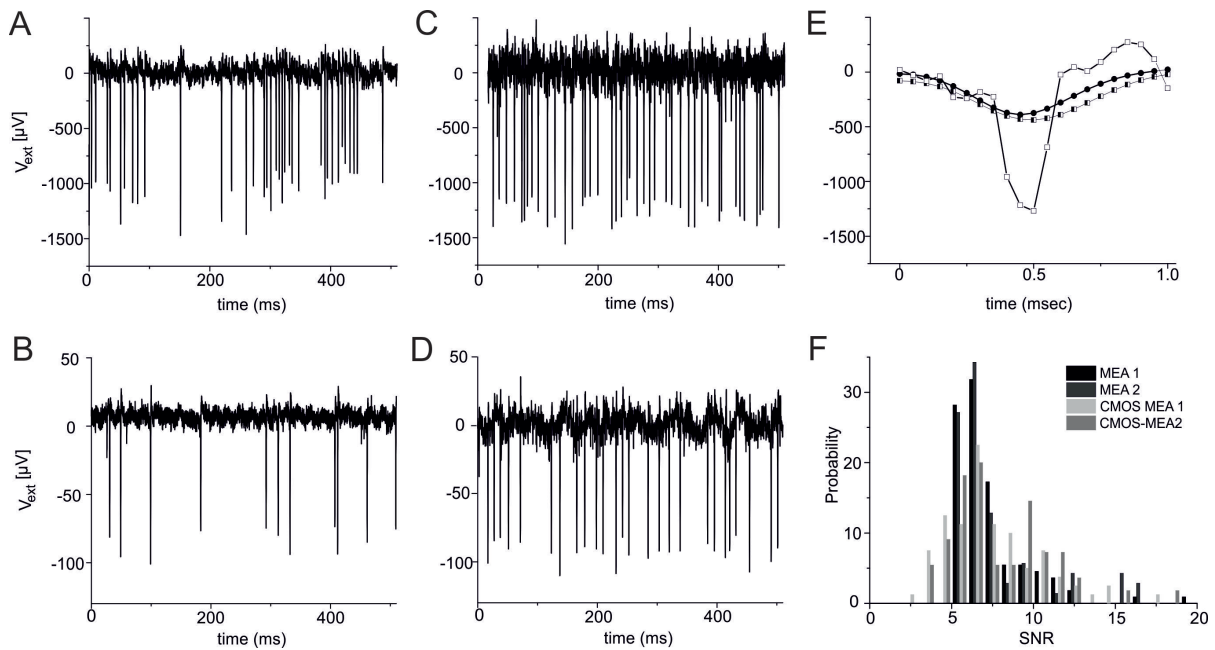


**Figure 3.2:** Comparison of CMOS-MEA and metal-electrode MEA recordings. **a, b):** Cell-culture recordings from CMOS-MEA (**a**) and from metal-electrode MEA (**b**). Note different scales of recorded voltage. **c, d):** Recordings of RGC activity obtained using a CMOS-MEA (**c**) and using a metal-electrode MEA (**d**). **e):** Trace obtained with conventional MEA (transparent circles) compared to traces obtained with CMOS-MEA without filtering (transparent squares) and after applying of a 1 kHz lowpass-filter (semi-filled squares). **f):** Histogram of SNR calculated for two different MEA and two different CMOS-MEA recordings of RGC activity. Cell populations per recording were in the order of 100 cells.

### **3.1.4 Discussion**

We presented that measurements of neuronal activity in ex-vivo tissue slices and neuronal cultures show different signal-amplitudes when recorded with metal-electrode MEAs and CMOS-MEAs. Our work furthermore showed that the SNR is approximately the same for both the conventional MEA and the CMOS-MEA 5000 system used in our experiments. SNR for future versions of the CMOS-MEA 5000 system might possibly improve in future versions of the system due to on-chip placement of analog lowpass-filters. This was not yet feasible for the current version of the setup due to the additional power-consumption and heat-generation. Noise components above the Nyquist-frequency are therefore aliased to lower frequencies during digitizing. Expected progresses in miniaturization might overcome this restriction and further improve the SNR of the system. We also argue that simple SNR values might not always represent the recording-quality of a system, since for MEAs with smaller electrode sizes different spike-detection algorithms can be used. This allows lower detection thresholds compared to systems where cells are only visible on single electrodes. An example for such an algorithm was presented by Lambacher et al. 2011 which is implemented in the CMOS-MEA tools software. While in our experiment the metal-electrode MEA was restricted to AP amplitudes exceeding a simple  $5\sigma$  threshold, the detection algorithm used for the CMOS-MEA allowed detection of smaller signal amplitudes at similar false-positive ratios. Drawbacks of those high-resolution systems are the additional requirements for hardware components. Programming of custom data-analysis tools is becoming more challenging and time-consuming due to the added complexity of correlated activity on neighboring channels. Due to larger data sets, additional effort has to be put on garbage-collection, restricting data to required resolution and parallel processing. Trends go from conventional data-analysis to machine-learning based algorithms. At the same time MEA-system manufacturers like Multichannel Systems GmbH provide users with software tools with a growing set of predefined methods for data filtering, spike-sorting and evaluation. Computer systems with the necessary computational power are becoming cheaper and cost only a fraction of the CMOS-system.

In summary current CMOS-MEA systems offer similar recording quality for single-electrode events as passive MEAs. However high spatial electrode density allows detection of signals at lower thresholds. Corresponding additional computation effort necessary for analyzing of high-density CMOS-MEA recordings is justified if additional spatial information is required. Examples are STAs, axonal signal-conductance or LFPs. If only time-stamps of recorded activity are required, passive MEAs offer the same information at less effort.

We noticed that recordings with CMOS-MEAs and passive MEAs show different shapes of RGC APs. 1 kHz lowpass-filtering made the CMOS-MEA trace much more similar to the trace recorded with the MEA. A possible explanation for observed absence of higher



frequencies in the metal-electrode MEA recording might lie in the manufacture-based stray capacitance. Metal-electrode MEAs have separate output lines for each electrode. These output lines are insulated from one another by thin oxide layers. While these oxide layers inhibit current-flow between the lines, they do not block capacitive crosstalk and therefore form a stray-capacitance. This capacitance couples to the bath which is kept at ground-potential (see Figure 3.1). Typical values are in the range of tens to hundreds of pF (D James et al. 2004). Capacitance values of oxide-covered electrodes in contrast are two to three orders of magnitudes lower since CMOS-MEAs usually use multiplexed readout approaches reducing stray capacitance effects.

Figure 3.1 shows the resulting circuitry.  $Z'_e$  consists of the spreading-resistance  $R_{\text{spread}}$ , the resistive and capacitive properties of the electrode  $R_e$  and  $C_e$ , and the resistance  $R_m$  of the metal interconnect between electrode and amplification stage.  $Z'_e$  together with the stray capacitance  $C_{\text{stray}}$  might form a lowpass-filter. If we now assume  $Z'_e$  to be nearly constant in the frequency range 10 Hz to 5000 Hz and also assume that it is in this regime dominated by the spreading-resistance with a typical value of  $R_{\text{spread}} = 3 \text{ M}\Omega$  (Voelker and Fromherz 2006), the cutoff-frequency of the filter is given by

$$f_c = \frac{1}{2\pi RC} = \frac{1}{2\pi Z'_{e,\text{effective}} C_s}.$$

Finally assuming a typical value of the stray-capacitance  $C_{\text{stray}} = 50 \text{ pF}$ , we get  $f_c \approx 1 \text{ kHz}$ . Here we showed that metal-electrode MEAs have intrinsic lowpass-filter properties when interfaces with neural tissue. This was valid as proof of principle since filtering properties rely not only on MEA but also on the interfaced tissue and adhesion thereof and parameters such as the junction-width may vary by a magnitude thereby changing the cutoff-frequency accordingly. These intrinsic filtering properties might explain at least parts of the observed differences in recorded AP amplitude for CMOS-MEA and conventional MEA.

## **3.2 Effects of optical stimulation on CMOS-recordings**

Light is an important tool in neuroscience. Optogenetic approaches for example allow direct activation of specific ion-channels in the membrane of labeled neurons with high spatial and temporal resolution and optical stimulation reveals computational tasks performed by intrinsically light-sensitive neural networks like the retina (Fenno, Yizhar, and Deisseroth 2010; Baden et al. 2016). Interfacing the tissue of interest with MEAs provides a useful method to simultaneously monitor induced activity changes and network modulations allowing correlation of cause and effect. Illumination however often also affects the MEA's underlying electronics resulting in artifacts in the recording. If these artifacts are too strong information contained in the recorded signal might not

be accessible for data analysis. Analyzing and quantifying of effects of illumination is therefore crucial for experimenters to be able to choose their setups accordingly. Here we analyzed effects of optical stimulation on previously investigated imaging capabilities of the CMOS-MEA 5000 system.

### **3.2.1 Abstract**

In this publication effects of optical stimulation at different wavelengths on CMOS-MEA recordings were investigated. Leakage-currents through the  $\text{TiO}_2/\text{Zr}$ -layer were measured for different bath-voltages during and without illumination. Observed conductance-changes were quantified and physical explanations for the corresponding wavelength-dependency provided. Feasibility of biological measurements during optical stimulation at short wavelength was demonstrated using wild-type mouse retina (C57BL/6J). Artifacts caused by optical stimulation could be completely removed. While the results of this publication are reviewed in this chapter, the focus will be on the contributions performed in the frame of this thesis. This also includes additional results which were not part of “Optical Stimulation Effects on  $\text{TiO}_2$  Sensor Dielectric Used in Capacitively-Coupled High-Density CMOS Microelectrode Array” (Bertotti, Jetter, Keil, et al. 2017).

### **3.2.2 Material and Methods**

The CMOS-MEA 5000 system was used in these experiments using a chip with a 25 nm oxide layer. In the first experiment, the I/V characteristics of the dielectric was measured as a function of the voltage applied between the electrolyte solution on the chip’s surface and CMOS-MEA electrodes. A custom potentiostat was used for this purpose with Pt counter electrode and Ag/AgCl reference electrode, and a voltage was applied to the potentiostat’s input. For simplicity this voltage is called "bath voltage" in the following. All TiN stimulation and sensing sites of the CMOS chip were held at ground potential using a semiconductor analyzer (Agilent B1500A) to measure the current through the dielectric. The measured current was normalized to the total area of the TiN sites. If not otherwise specified, all measurements were performed with a 1 M solution of NaCl. To prevent effects of light-contamination, experiments were performed in a light-shielded setup. To illuminate its surface, LEDs setups introduced in Section 2.2.2 were used. Center wavelengths of 875 nm (infrared), 625 nm (red), 525 nm (green), 475 nm (blue), and 412 nm (violet) were applied with corresponding and full-width half-maximum values of 37 nm, 25 nm, 30 nm, 25 nm, and 5 nm. In all cases, an irradiance of  $100 \mu\text{W mm}^{-2}$  was applied. Finally a chip without oxide was left in contact with air for several days to form a native  $\text{TiO}_2$ -layer. This chip was then used for recording. During recording light at 400 nm was switched on for 2.5 s. The same procedure was also performed with a regular 25 nm CMOS-chip. Induced drifting effects were compared.

### 3.2.3 Results

In the first experiment, I/V characteristics of the oxide layer of post-processed chips were tested using different solutions (Fig 3.3, *right*). Oxide resistivity was stable in the range between  $-0.5\text{ V}$  to  $-4\text{ V}$  as previously published by Bertotti, Velychko, Dodel, Keil, Wolansky, Tillak, Schreiter, Grall, Jesinger, Rohler, et al. 2014. Differences between solutions were marginal. For not post-processed electrodes, i.e. electrodes without oxide layer, observed leakage-currents were drastically larger compared to oxide-covered electrodes and no stable plateau was observed for any voltage range.

Wavelength-sensitivity was tested for a set of fixed bath voltage values ( $-0.5\text{ V}$ ,  $-1.0\text{ V}$ ,  $-1.5\text{ V}$  and  $-2.0\text{ V}$ ). Results are shown on the left-hand side of Figure 3.3. While insulating properties were stable for longer wavelengths, an increase in leakage currents was observed during illumination at  $412\text{ nm}$ . Measured currents scaled linearly with applied bath voltage. A second experiment to investigate effects of  $412\text{ nm}$  and  $475\text{ nm}$  illumi-

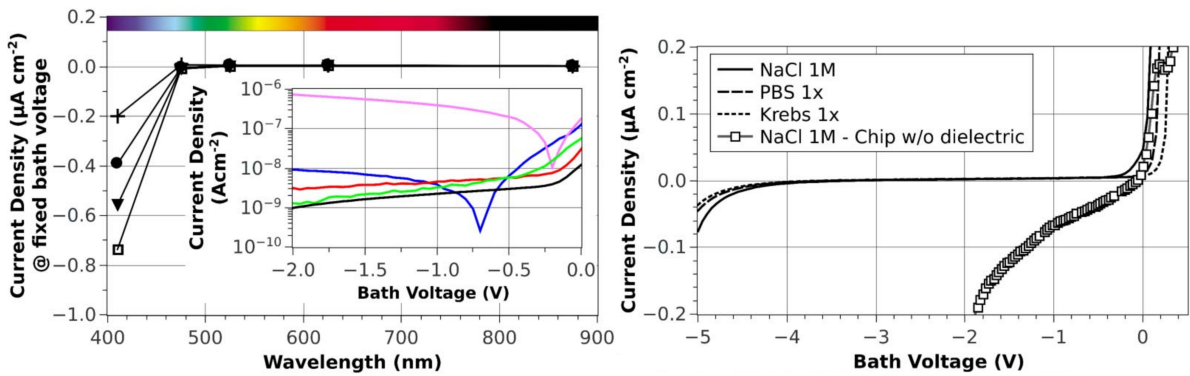


**Figure 3.3:** *Right:* Leakage current as function of applied bath voltage for different electrolyte solutions. Also a measurement for uncovered TiN electrodes is shown. Insulating properties of the chip surface increase drastically with oxide compared to bare electrodes. Differences between measurements using different electrolytes were marginal. Insulation is stable between bath voltages of  $-0.5\text{ V}$  to  $-4\text{ V}$ . *Left:* Current density as measured during illumination of various wavelength at different bath voltages. Current densities increase drastically for illumination at  $412\text{ nm}$ . Inlet: Voltage dependence of current-density for different wavelengths.

nation on the current density was performed. Bath voltage was increased and decreased periodically from  $-1.0\text{ V}$  to  $0.5\text{ V}$  at a rate of  $33.3\text{ mV s}^{-1}$  while simultaneously measuring resulting currents. Measurements were performed during and without illumination. Results are shown in Figure 3.4. For illumination at  $475\text{ nm}$  and without illumination measured current densities showed only small differences. Both were largely dominated by a constant plateau relating to capacitively induced displacement current which is proportional to  $\frac{dV}{dt}$ . The curve measured during illumination with  $412\text{ nm}$  however showed

components scaling linear with the applied voltage (Figure 3.4 a). As a result computed conductance-curves deviated from zero for this measurement (Figure 3.4 b,c). During illumination at 475 nm and in absence of illumination the curve showed zero conductance in the range of 0.0 V to  $-1.0$  V for falling voltage  $\frac{dV}{dt} < 0$ , as well as in the range of  $-0.5$  V to  $-1.0$  V for rising voltage  $\frac{dV}{dt} > 0$ . For  $\frac{dV}{dt} > 0$  and 0.0 V to  $-0.5$  V conductance deviated from zero. For 412 nm illumination a substantial increased conductance was observed over the whole  $\frac{dV}{dt}$ -regime.

In the last experiment effects of optical stimulation on recording from neural tissue were

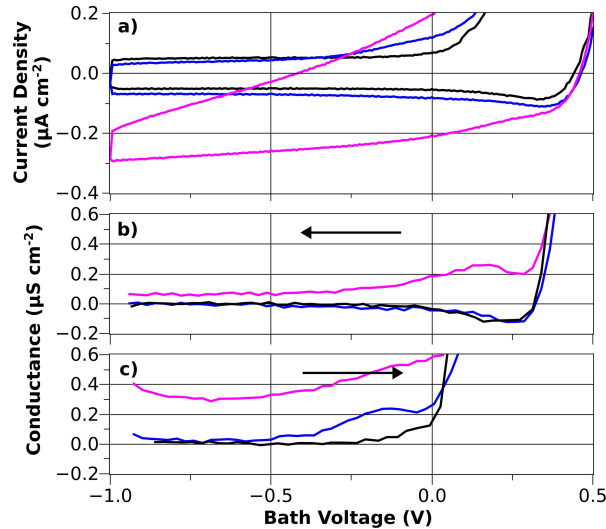


**Figure 3.4:** Cyclovoltammogram measurements of leakage current. Voltage was cyclically increased and decreased from  $-1.0$  Volt to  $0.5$  Volt. Measurements were performed without illumination (black) and with illumination at  $475$  nm (blue) and  $412$  nm (violet). **a)** Recorded traces for the whole cycle. Current plateaus for black and blue traces indicate purely capacitive behavior over most of the voltage range. Violet trace shows clear deviations from this behavior. **b)** Recordings for  $\frac{dV}{dt} < 0$ . **c)** Recordings for  $\frac{dV}{dt} > 0$ .

investigated. C57BL/6J mouse retina was interfaced with the CMOS-MEA in epiretinal configuration and light-pulses of different wavelength were applied at a frequency of  $1$  Hz with a duty-cycle of  $50\%$ . A single RGC was chosen exemplary from  $\geq 100$  cells in the recording. Criteria for selection were isolation of the cell signal, e.g. no signals from multiple cells on the same recording electrodes, and light-response over a wide spectrum. Due to the small recording electrode pitch of  $16\mu\text{m}$  signals of single cells are visible on multiple electrodes. For the selected cell traces from the electrode with the largest recorded signals is shown. Figure 3.5 shows the recorded raw signals along with the filtered recordings for all four wavelengths. Cell responses to the applied  $1$  Hz flicker stimuli are clearly visible for all but  $635$  nm. This was expected since mice PRs contain only S- and M-cones. Optical stimulation results in a strong drift which is larger for shorter wavelengths. Drifts of approximately  $-20\text{ mV s}^{-1}$  were observed. These induced

artifacts could be completely removed using filters described in the methods section. Next a chip without sputtered oxide was left in contact with air to grow a native  $\text{TiO}_2$  layer for several days. We then used this chip and conventional 25 nm  $\text{TiO}_2/\text{Zr}$  chip for recording during illumination at 400 nm for 2.5 s. Recorded traces are shown in Figure 3.6.

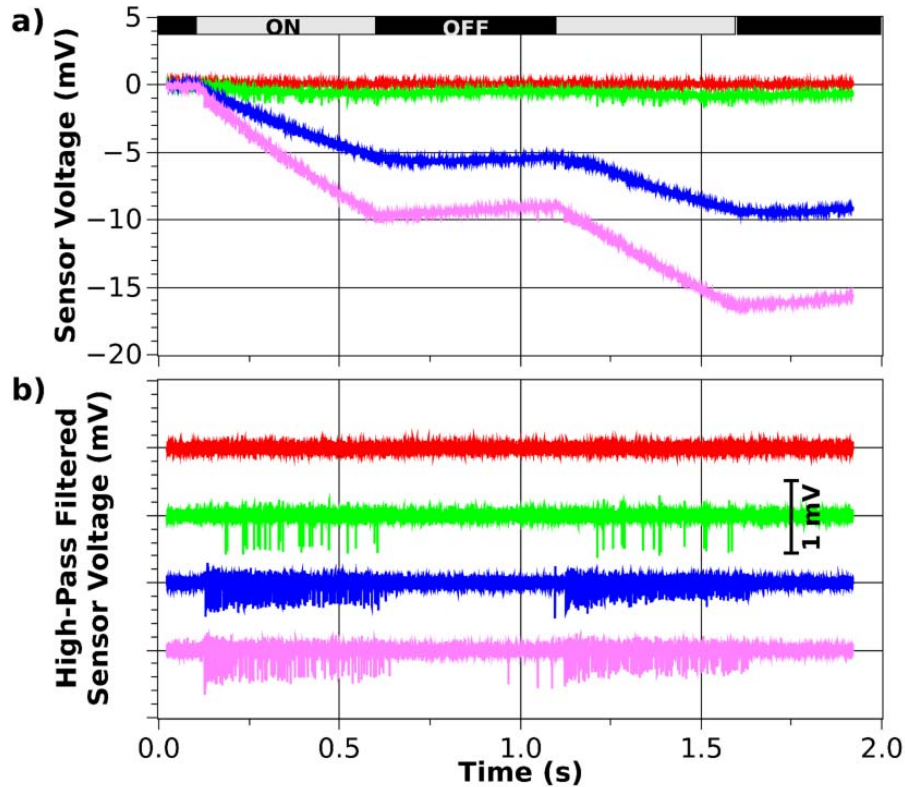


**Figure 3.5:** Recordings of a C57BL/6J mouse RGC activity during optical stimulation with 1 Hz and 50% duty-cycle at different wavelengths. **a)** Raw recording traces. Illumination induced increases in the drift of the recorded signal are clearly visible. Drifts are stronger for shorter wavelengths. **b)** Traces after offset correction and high-pass filtering using a 4th order 100 Hz Bessel filter. Drift artifacts were completely removed. Recorded APs are now clearly visible. As expected for mouse retina no activity was induced by red light. The RGC’s spectral sensitivity was tuned to higher sensitivity for short wavelength in the blue-violet regime compared to longer wavelength in the green regime.

### 3.2.4 Discussion

The  $\text{TiO}_2/\text{Zr}$  layer provides stable insulating properties of the CMOS-MEA in a dark environment when applied stimuli are limited to negative voltages. Note that the supply

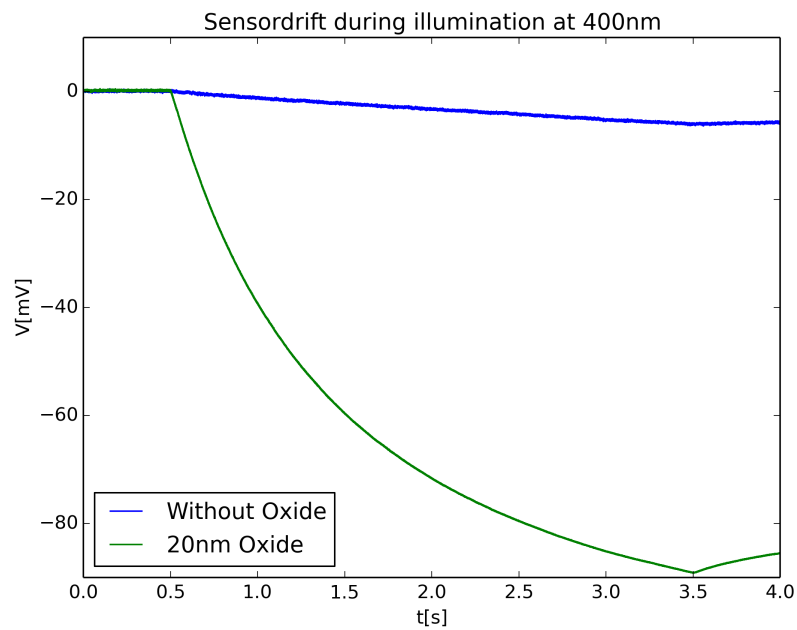


**Figure 3.6:** Effects of optical stimulation at 400 nm on CMOS-MEA 5000 chips with TiN/ZrO<sub>2</sub> and chips without a sputtered oxide layer. For the later a native, thinner oxide layer is created by oxidation effects over time. Drifting effects induced by light illumination are clearly smaller for thinner oxide layers.

voltage of the CMOS-MEA is 3.3 V so that the voltage range below  $-4$  V where leakage currents start to increase is not accessible. For illumination at wavelengths  $> 475$  nm coupling between electrodes and bath is still purely capacitive. For wavelengths towards the ultra-violet regime non-capacitive effects are observed. We exclude direct effects of illumination on the CMOS circuitry since the layout of the six metal layers was chosen such that it provides an efficient light shield for the active CMOS devices and the silicon substrate.

TiO<sub>2</sub> is a semiconductor with a bandgap of approximately 3.0 eV which is energetically equivalent to a photon with a wavelength of  $\nu = 413$  nm (Grant 1959). Photons with  $\nu \leq 413$  nm wavelength can therefore directly create electron-hole pairs by photoelectric interaction in the oxide layer. These free charged particles result in an increase in the conductance and therefore in a non-capacitive current flow across the oxide layer. A CMOS chip without oxide layer was illuminated with blue and violet light to verify this interpretation and no drift was observed. Looking at the data shown in the inset of Figure 3.3 we can see that for violet illumination a working point of  $-250$  mV yields a minimum leakage current which is seven-fold lower than at 0 mV.

Recording of RGC activity during optical stimulation proofed feasibility of recording of light induced responses. Stimulation artifacts were completely removed after applying previously mentioned filters. For violet light sensor drift was approximately  $-20$  mV s<sup>-1</sup>. Given the dynamic range of the measurement system recordings of at least 5 s to 10 s are possible using a flicker frequency of 1 Hz and 50% duty cycle. Lower illumination intensities would significantly increase the duration. The implementation of the MOSFET in the CMOS system would also allow resetting of the node voltage in cases of large drift e.g. for optogenetic experiments. Possible issues might however include non-linear scaling of ADCs over its working-range. While these scaling effects should not influence the SNR ratio, they affect the absolute signal amplitude. This might result in problems during the spike-sorting process. For short light stimuli  $t \leq 0.5$  s this did not turn out to be a problem. For longer illumination periods, dynamic rescaling of noise might overcome this restriction.

Chips with native grown oxide-layer show significantly smaller drifting-effects during illumination than conventional chips. This is most likely a result of fewer electron-hole pairs being created due to the shorter travel-distance of light in thin oxide layers. Another effect might be the absence of Zr in the native oxide, possibly changing its optical cross section. An estimate of the thickness of native grown oxide and its effects on the specific capacitance is given in the next section. In conclusion simultaneous optical stimulation and recording using the CMOS-MEA 5000 system is feasible. While short wavelengths induce drift artifacts on the recording these effects can be reduced by choosing an appropriate bath voltage. Remaining artifacts can be removed by a set of digital filters allowing analysis of contained neural signals.

### 3.3 CMOS MEAs with native oxide

We now investigated properties of CMOS-MEAs with native TiO<sub>2</sub>-oxide, i.e. CMOS MEAs without the last post-processed layer. Based on previous results we estimated to observe smaller effects of optical stimulation on recording drift and thus a potential increase in specific capacitance of stimulation electrodes, increasing accessible stimulation current range.

#### 3.3.1 Material and methods

Chips used for this experiment underwent the same fabrication process as regular CMOS-MEAs except for the post-processing sputtering of a TiO<sub>2</sub>/Zr oxide layer. Instead chips were stored in contact with air for several days. A native TiO<sub>2</sub> layer of initially unknown thickness formed by oxidation processes. In this experiment transient sinusoidal voltage-traces of different frequencies and amplitudes were applied to the stimulation electrodes and resulting bath-currents were measured as described in Section 2.2.3. PBS with a conductivity of 66 Ω cm was used as electrolyte. Separate experiments were performed for stimulus frequencies of 10 Hz, 25 Hz, 40 Hz and 100 Hz. For all frequencies applied peak-peak voltage-amplitudes ranged from 0 mV to 2500 mV in steps of 500 mV.

#### 3.3.2 Results

Sinusoidal stimuli at different amplitudes and frequencies were applied in order to determine the specific-capacitance of the CMOS-MEA, test the degree of capacitive-coupling between stimulation voltage and resulting bath-current, and to put an estimate on the thickness of the native oxide layer.

The relation between applied voltage and resulting bath-current for purely capacitive systems is given by

$$I = C_s \frac{dV}{dt}. \quad (3.1)$$

In other words the stimulation electrode and the bath are coupled purely capacitive if the induced bath-current scales linearly with  $\frac{dV}{dt}$  and there's no bath-current for constant stimulation voltages,

i.e.  $I \left( \frac{dV}{dt} = 0 \text{ V s}^{-1} \right) = 0 \text{ A}$  for all voltages  $V$  within the applied stimulation range. We shifted the applied sinus-shaped stimuli by  $-90^\circ$  to compensate for the derivation-based shift and simplify evaluation, resulting in the following equation:

$$I = C_s \frac{dV}{dt} = C_s \frac{d}{dt} V_0 \sin(2\pi ft - 90^\circ) = 2\pi f C_s V_0 \sin(2\pi ft) = I_{max} \sin(2\pi ft) \quad (3.2)$$



with

$$I_{max}(V_0, f) = 2\pi f V_0 C_s. \quad (3.3)$$

First we determined the specific capacitance of the CMOS-MEA. We therefore plotted

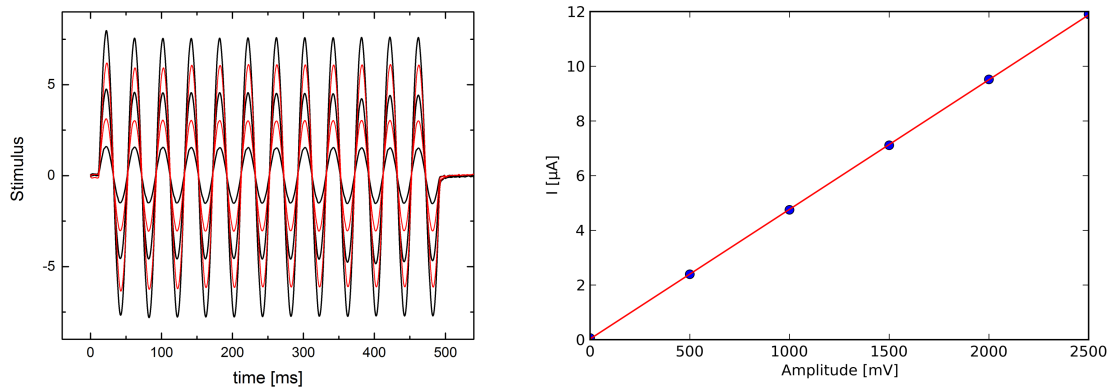


**Figure 3.7:** Illustration of capacitive behavior for 40 Hz stimulation. *Left:* Overlay of recording traces in arbitrary units during stimulation with different amplitudes ranging from 500 mV to 2500 mV in steps of 500 mV. *Right:* Peak-peak values of recorded current-amplitudes for applied stimuli of different voltage-amplitudes but same frequency of 40 Hz. Current amplitudes scale linearly with applied voltage.

current-amplitudes  $I_{max}(V_0, f) = I_{max}(V_0, f) = 2\pi f C_s V_0$  against applied voltage amplitudes  $V_0$  while keeping the frequency constant. From these plots we obtained the line of best fit by linear regression for each applied frequency. The total stimulation capacitance  $C_s$  for each frequency is then given by the inclination of the line of best fit divided by  $2\pi f$ . The specific capacitance  $c_s$  relates to the total capacitance  $C_s$  by  $c_s = \frac{C_s}{A_{stim}} = \frac{C_s}{648 \mu\text{m}^2}$ . Values for specific capacitance were calculated for 10 Hz, 25 Hz, 40 Hz and 100 Hz and are shown in Table 3.9. An exemplary plot for 40 Hz stimulation illustrating the procedure is shown on the left-hand side of Figure 3.8. We found that capacitance values decreased with increasing stimulation-frequency.

We then evaluated how  $I(V_0, f)$  changes for constant voltages and variable frequencies. Results are shown in Figure 3.8 and Table 3.9. Again we observed a frequency dependence in the MEA's capacitance. Lines of best fit were obtained using current values  $I(f = 10 \text{ Hz})$  and  $(f = 25 \text{ Hz})$  only to reduce effects of frequency dependence. Fits for all voltages showed small or no offsets indicating largely capacitive stimulation.

Finally we estimated the thickness of the native oxide layer. The specific capacitance of a electrolyte-TiO<sub>2</sub>-Si interface with a TiO<sub>2</sub> thickness is  $c_{s,15.6 \text{ nm}} = 1.44 \mu\text{F cm}^{-2}$  (Wallrapp and Fromherz 2006). The capacitance of a parallel-plate capacitor is given

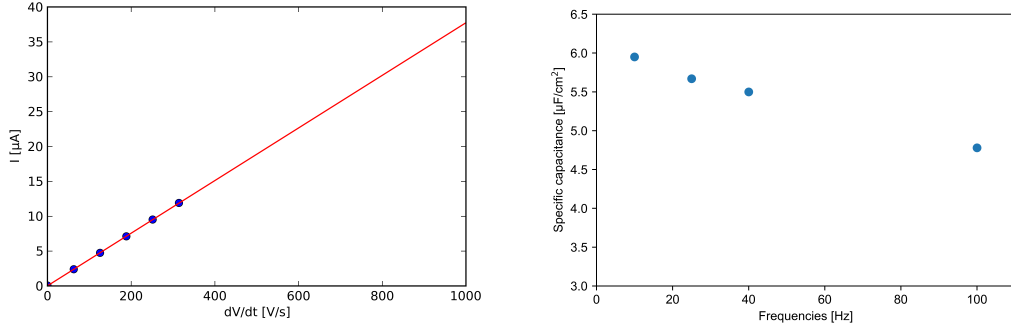


**Figure 3.8:** *Left:* Peak-current measured during 40 Hz stimulation using a combined electrode area of  $648 \mu\text{m}$  plotted against  $\frac{dV}{dt}$ . Red line shows line of best fit obtained by linear extrapolation. Chip capacitance is given by the inclination of the fitted line. *Right:* Specific-capacitance values obtained for different frequencies. Capacitance decreases with increasing frequency since  $c_s = c_s(\epsilon_r(f))$  and  $\lim_{f \rightarrow \infty} \epsilon_r = 0$ .

Frequency [Hz]	10	25	40	100
$c_s$ [ $\mu\text{F cm}^{-2}$ ]	6.31	6.0	5.84	5.07

**Figure 3.9:** Specific capacitance values obtained for various frequencies. Values were obtained as inclination from  $I(V)$  divided by the total stimulation area used. Smaller values for  $c_s$  were observed for larger stimulation frequencies. This was expected as the relative permittivity  $\epsilon_r = \epsilon_r(f)$  is frequency dependent with  $\lim_{f \rightarrow \infty} \epsilon_r = 0$ . The capacitance therefore decreases as well (see Equation 3.4).

by

$$C = \epsilon_0 \epsilon_r \frac{A}{d} \quad (3.4)$$

Thickness of the native oxide-layer was then obtained as

$$\frac{c_{\text{processed}}}{c_{\text{native}}} = \frac{d_{\text{native}}}{15.6 \text{ nm}} \quad (3.5)$$

which is equivalent to

$$d_{\text{native}} = 15.6 \text{ nm} \frac{c_{\text{processed}}}{c_{\text{native}}}. \quad (3.6)$$

With  $c_{\text{TiO}_2, \text{native}} = 4.8 \mu\text{F cm}^{-2}$  obtained from recordings, this yields  $d_{\text{TiO}_2, \text{native}} \approx 4.7 \text{ nm}$ , where  $c_{\text{processed}}$  is the specific capacitance of a processed CMOS-MEA with a  $\text{TiO}_2$  layer of  $15.6 \text{ nm}$  and  $c_{\text{native}}$  is the specific capacitance of an unprocessed CMOS-MEA with native oxide layer.

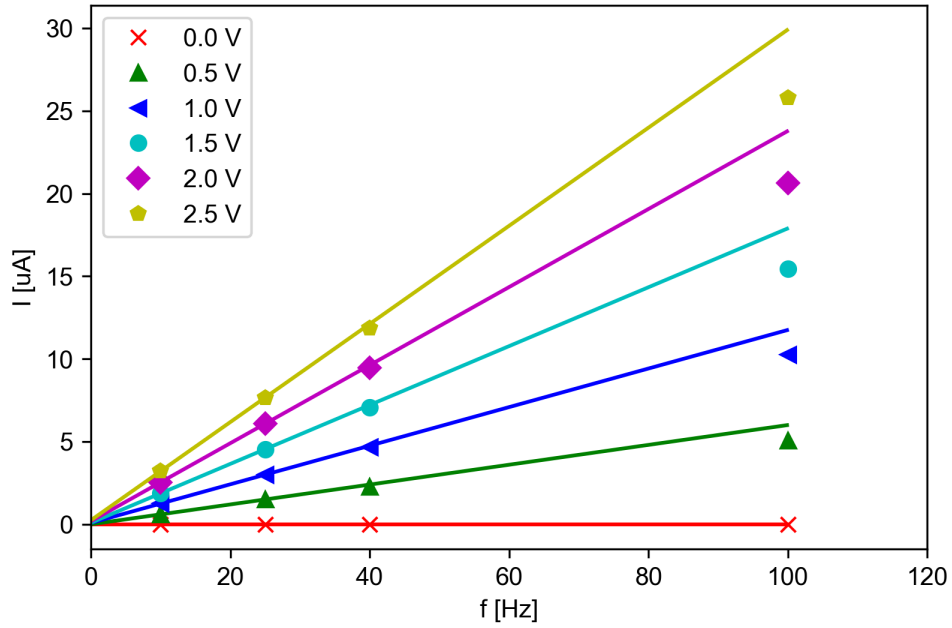


**Figure 3.10:** Induced bath currents plotted against sinusoidal frequencies for all applied voltages. Linear extrapolation has been calculated based on results for 10 Hz and 25 Hz. Currents for larger frequencies are below extrapolated values due to frequency dependence of permeability. Linear fits cut the y-axis at 0 Hz close to the origin, as the stimulation is highly (if not purely) capacitive.

### 3.3.3 Discussion

We showed that induced displacement current scales linearly with  $\frac{dV}{dt}$  and did not show any current-offset. Offsets derived for  $I(f)$  and constant voltages were very small. Additionally the line of best fit is intrinsically tilted due to non linear scaling of  $\epsilon_r$ . Obtained current-offsets might therefore be purely artificial. Both results for  $I(f, V_0)$  show that stimulation using CMOS-MEAs with native oxide is highly if not purely capacitive.

Obtained specific capacitance were larger compared to those for conventional CMOS-chips with sputtered  $\text{TiO}_2/\text{Zr}$  layer (see Table 3.9. This is in good agreement with our expectations, since the native oxide layer is thinner. Specific capacitance values of  $\text{TiO}_2$  from literature which were derived for electrolyte/ $\text{TiO}_2/\text{Si}$  stacks with an oxide thickness of 15.6 nm allowed us to estimate the thickness of the native oxide layer to  $d_{\text{TiO}_2, \text{native}} \approx 4.8 \text{ nm}$  (Wallrapp and Fromherz 2006). We want to discuss two aspects regarding the way capacitance values were obtained by Wallrapp and Fromherz 2006:

Voltage	10 Hz	25 Hz	40 Hz	100 Hz	$p_c$ (Inclination)	$p_l$ (Offset)
0.5 V	0.60 $\mu\text{A}$	1.50 $\mu\text{A}$	2.29 $\mu\text{A}$	5.08 $\mu\text{A}$	0.06 $\mu\text{A s}$	0.0 $\mu\text{A}$
1.0 V	1.25 $\mu\text{A}$	3.00 $\mu\text{A}$	4.69 $\mu\text{A}$	10.27 $\mu\text{A}$	0.12 $\mu\text{A s}$	0.08 $\mu\text{A}$
1.5 V	1.87 $\mu\text{A}$	4.54 $\mu\text{A}$	7.06 $\mu\text{A}$	15.44 $\mu\text{A}$	0.18 $\mu\text{A s}$	0.09 $\mu\text{A}$
2.0 V	2.54 $\mu\text{A}$	6.08 $\mu\text{A}$	9.47 $\mu\text{A}$	20.65 $\mu\text{A}$	0.24 $\mu\text{A s}$	0.18 $\mu\text{A}$
2.5 V	3.21 $\mu\text{A}$	7.66 $\mu\text{A}$	11.86 $\mu\text{A}$	25.79 $\mu\text{A}$	0.30 $\mu\text{A s}$	0.24 $\mu\text{A}$

**Figure 3.11:** Frequency dependance of stimulation currents for constant voltages. Each line refers to one constant voltage level and the corresponding current values obtained for frequencies 10 Hz, 25 Hz, 40 Hz, and 100 Hz. A linear fit has been applied for each set using only values obtained for 10 Hz and 25 Hz in order to minimize effects of frequency dependence of the capacitance. The fit was of the form  $V(f) = p_c f + p_l$ .  $p_c$  therefore represents the capacitive component and  $p_l$  the leakage component of the stimulation. Leaking-voltage is therefore dominated by capacitive stimulation-currents by a factor of at least 12.5 for 10 Hz and up to two magnitudes for 100 Hz.

First, electrolytes with different resistivity were used in our experiment and cited work. In the work of Wallrapp and Fromherz values were obtained using electrolyte 160 mM NaCl, pH 5.9, and resistivity of 56  $\Omega$  cm. This is a difference of 9  $\Omega$  cm or  $\frac{\rho_{\text{Wallrapp}}}{\rho_{\text{currentwork}}} \approx 0.86$  to the resistivity used in our experiment. The resistivity of the medium should however not have an influence on the induced displacement current. This is confirmed by the results obtained from an experiment in which we used the same stimulus protocols and CMOS-MEA used in this work although with RD10 mouse retina interfaced on the CMOS-MEA and AMES medium (A 1420, Sigma Aldrich, Germany). Data is shown in the Appendix in Table 1. Obtained capacitance values are in good agreement with the results presented here. Second, Wallrapp and Fromherz 2006 used Si as electrode-material while for CMOS-MEAs electrode are made from Ti. Again, this should not have any effect on the capacitance (see Equation 3.4). We argue that a thickness of approximately 5 nm provides an upper limit to the thickness of native oxide, since measurements were performed for several chips, but no large deviations from presented results were obtained. When we compare the obtained specific capacitance to that of conventional CMOS-MEAs, we notice that the thickness of the oxide layer does not account for the complete difference in capacitance. If only for the thickness, the specific capacitance of 25 nm oxide chips should be roughly  $c_{25\text{ nm}} \approx \frac{1}{5}c_{4.8\text{ nm}}$ . The difference is however only  $c_{25\text{ nm}} = 1.5\ \mu\text{F cm}^{-2} \approx \frac{1}{3}c_{4.8\text{ nm}}$ . The oxide layer of conventional CMOS-MEAs also contains 20% Zr with  $\epsilon_{\text{TiO}_2/\text{Zr}} > \epsilon_{\text{TiO}_2}$ . Using sputtered layers of  $\text{TiO}_2/\text{Zr}$  instead of native grown  $\text{TiO}_2$  with similar thickness could therefore increase the specific capacitance even further. Finally specific capacitance values were found to be frequency dependent. This however is also in good agreement with results published in (Eickenscheidt et al. 2012) and can be explained by frequency dependence of permittivity  $\epsilon_r$ .

## **3.4 Stimulus Response Relations to sinusoidal stimuli**

### **3.4.1 Abstract**

Here we investigated stimulation thresholds for sinusoidal stimulation for blind (RD10) and healthy (C57BL/6J) retina. Effects of sinusoidal stimulation on neural coding were not only analyzed for activity modulation, but also for timing modulation and reliability. Sinusoidal voltage traces with frequencies of 10 Hz, 25 Hz and 40 Hz were applied to the stimulation electrodes and presented to RD10 and C57BL6/J retina. Individual thresholds were obtained for each stimulation frequency and animal model.

Next the total area of spatially connected stimulation electrodes was varied and effects on stimulation thresholds were analyzed. Findings were compared to stimulation thresholds obtained for pulsatile stimulation published in “Electrode-size dependent thresholds in subretinal neuroprosthetic stimulation” (Corna, Herrmann, and Zeck 2018). Average thresholds for sinusoidal stimulation were found to be smaller than thresholds for pulsatile stimulation. Differences ranged from a factor of 2 for large stimulation areas up to more than a magnitude for small stimulation areas.

Finally control experiments were performed using pharmaceutical blockers to prevent RGC input from BPCs. Sinusoidal stimulation was found to affect RGC activity indirectly, i.e. by modulation of presynaptic RGC input. These findings were supported by the results of previously described experiments as axons remained unaffected by sinusoidal stimulation.

### **3.4.2 Material and Methods**

We interfaced RD10 and C57BL6/J mouse retina with the CMOS-chip as described in Section 2.1.2. We then applied sinusoidal stimuli of different amplitudes arranged in pseudorandom order to selected sets of stimulation electrodes. Amplitudes shown ranged from 0.0 V to 2.5 V in steps of 0.5 V. Each amplitude was shown for 280 ms to 300 ms with a pause of 500 ms between different amplitudes. The protocol was repeated five times for each experiment. Experiments were performed for 10 Hz, 25 Hz and 40 Hz. In the first set of experiments investigating current-density thresholds for previously mentioned frequencies all stimulation electrodes were used.

In the second set of experiments performed to obtain stimulation-area dependency of stimulation-thresholds, the smallest areas used measured  $2 \times 2$  electrodes while the largest areas used were full-field stimuli using all available  $32 \times 32$  electrodes. Stimulation electrodes were selected thus, that regions of good retina adhesion and high-quality neuronal signals were roughly centered above. Recordings were filtered using the procedure described in Section 2.3.1. All five recordings were appended and spike-sorted. Activity,

vector strength (VS) and reliability were calculated for each cell and each applied amplitude. So-called Stimulus Response Relations (SRR) were created as illustrated in Figure 3.13.

To verify if RGC activity modulations resulted from direct effects on RGCs or indirect effects by modulation of presynaptic input of RGCs, we performed an experiment using pharmaceutical blockers. First, we performed an experiment to obtain SRR as previously described. Then we replaced pure AMES-medium with AMES-medium mixed with DNQX and AP-7 at concentrations of 20  $\mu$ M and let it perfuse for 30 min. We then repeated the stimulation protocol. Finally, we washed the retina with pure AMES-medium and let it perfuse for another 30 min and presented the stimulation protocol.

### 3.4.3 Results

Result for the variation of stimulation intensity showed three important observations: First we observed an increase in activity, VS and reliability for most cells during stimulation at higher intensities. More interestingly effects on VS and reliability were already observed at stimulus intensities of 500 mV while activity transitions occurred between 1000 mV to 2000 mV. Second, as expected activity changes were positive for most cells ( $\Delta A > 0$ ). However for some cells down-modulation of activity was observed. Cells with negative  $\Delta A$  showed high initial spontaneous activity rates in the order of 50 Hz. As cells with high spontaneous activity rates have intrinsically high reliability values, down-regulation of activity correlated with down-regulation of reliability. Moreover a decrease in activity sometimes correlated with an increase in VS. No down-regulation of VS was observed for any cell. While most of the cells were affected by stimulation, some cells were unaffected by stimulation. Third, some cells initially responded with positive  $\Delta A$ , but then showed a decrease of activity for stronger stimuli. While for those cells the overall activity decreased after reaching a local maximum, vector-strength and reliability remained high. This indicates that while the number of spikes per stimulus period decreased after a certain stimulus intensity, the number of spikes per stimulus period reached a non-vanishing lower boundary and timing precision remained high. To evaluate thresholds for VS and activity we used the following two different approaches:

- In the first approach we fitted a sigmoidal Boltzmann function to the data. The sigmoidal Boltzmann function is given by

$$f(x) = y_{\min} + \frac{y_{\max} - y_{\min}}{1 + \exp((x_0 - x)/dx)}. \quad (3.7)$$

Here  $x_0$  is the applied intensity where  $f(x_0) = y_{\min} + (y_{\max} - y_{\min})/2$ . Values  $x_0$  were therefore used as threshold. However activity values of some cells did not saturate within the applied range of intensities, e.g. they did not converge

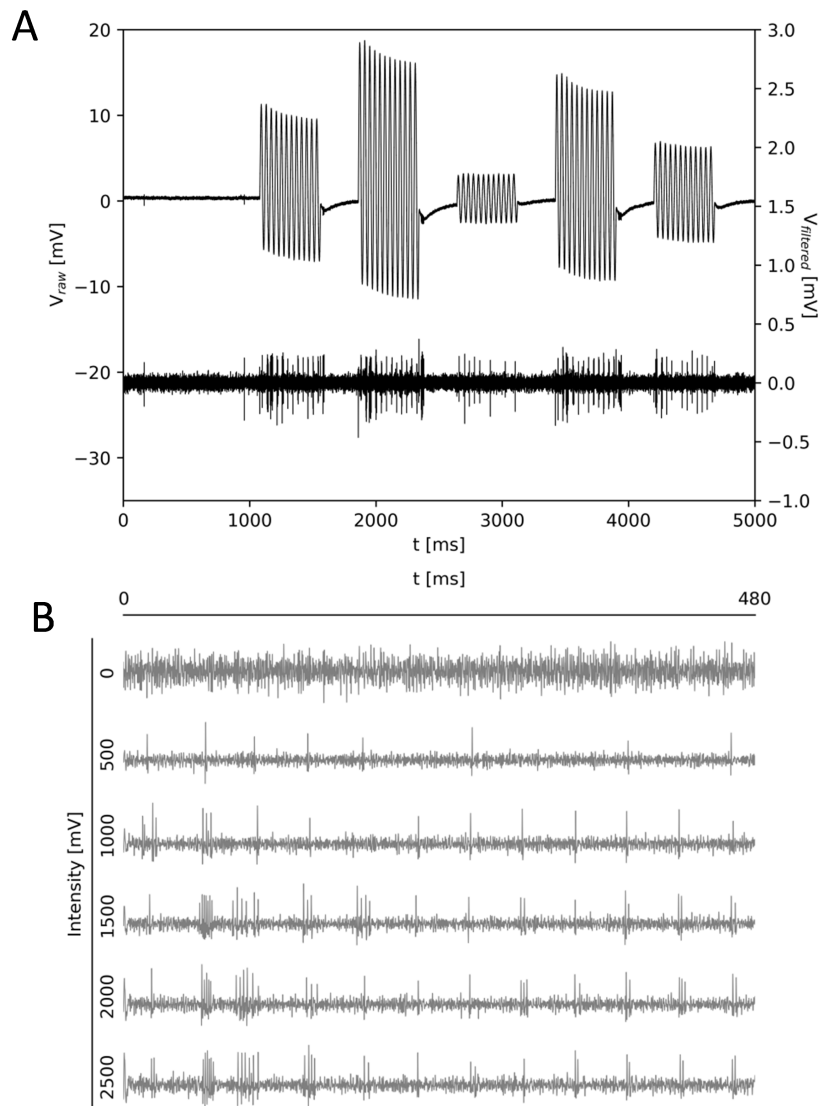


**Figure 3.12:** Illustration of artifact removal. A): Top: Raw-trace of single electrode recording of neuronal activity during sinusoidal stimulation. Voltage-scale on the left hand side of the diagram. Bottom: Filtered trace of the same recording after artifact-subtraction. Voltage scale on the right hand side of the diagram. B): Filtered traces of a different single electrode recording after artefact subtraction. Traces are arranged on the vertical axis in increasing stimulation-voltage order (top to bottom.)

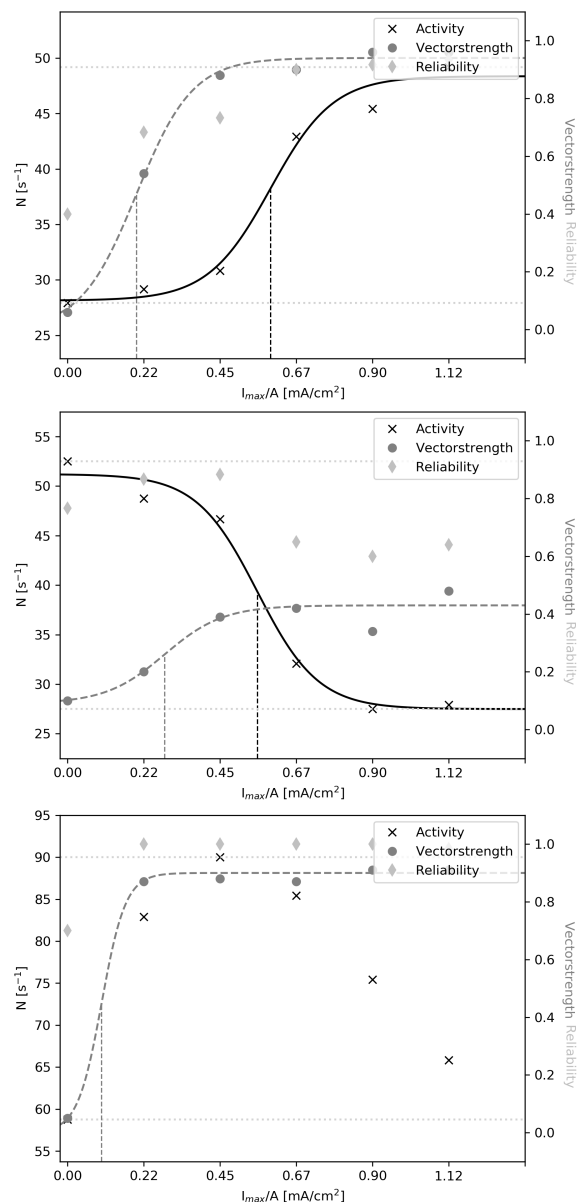


**Figure 3.13:** Illustration of exemplary data obtained from RD10 mouse retina to 25 Hz sinusoidal stimulation. Top: Typical stimulus response relation (SRR). Increase of stimulation intensity results in an increase of activity, vector-strength (VS), and reliability. Effects on activity are delayed relative to effects on VS. Middle: Example of a cell inhibited by sinusoidal stimulation. The cell starts with a high spontaneous activity rate of about 50 Hz. Increasing stimulation intensity correlates with a decrease of firing rate and an increase in VS. Bottom: Cell responds with an initial increase of activity to sinusoidal stimulation which is followed by an inhibition of the firing rate at higher intensities.



	electrodes	area [mm <sup>2</sup> ]	$x_0 \pm \sigma$ [ $\mu\text{C cm}^{-2}$ ]	$x_{30} \pm \sigma$ [ $\mu\text{C cm}^{-2}$ ]	$x_{50} \pm \sigma$ [ $\mu\text{C cm}^{-2}$ ]	vs $x_0 \pm \sigma$ [ $\mu\text{C cm}^{-2}$ ]
10 Hz	2x2	0.003	4.73±0.24	5.02±0.56	5.09±0.89	4.47±1.45
	4x4	0.010	8.62±0.79	6.27±1.26	6.98±1.49	10.15±0.62
	5x5	0.016	9.41±1.98	6.14±1.14	6.67±1.65	9.04±0.84
	6x6	0.023	9.40±0.66	8.78±0.56	8.94±0.79	7.84±0.42
	8x8	0.040	9.54±0.60	4.25±0.71	4.00±0.65	7.25±0.59
	10x10	0.063	10.00±0.26	5.60±0.59	6.16±0.63	6.37±0.44
	32x32	0.648	8.84±0.23	7.36±0.39	7.84±0.41	4.30±0.30
25 Hz	2x2	0.003	9.87±0.65	7.42±0.95	7.48±1.60	8.29±0.83
	4x4	0.010	8.60±0.69	6.26±0.65	6.08±0.86	5.90±0.43
	5x5	0.016	9.31±0.66	6.47±0.89	8.55±1.01	6.40±0.74
	6x6	0.023	8.81±0.47	5.61±0.57	8.33±0.74	5.40±0.31
	8x8	0.040	7.82±0.68	6.58±0.60	6.74±0.69	4.48±0.35
	10x10	0.063	7.94±0.43	5.57±0.49	6.51±0.57	4.08±0.37
	32x32	0.648	7.59±0.21	4.38±0.33	4.57±0.35	2.87±0.17
40 Hz	2x2	0.003	12.25±nan	3.68±0.65	2.84±0.57	5.98±0.95
	4x4	0.010	7.97±0.47	5.55±0.50	5.57±0.57	6.76±0.35
	5x5	0.016	10.04±0.48	6.53±0.96	6.16±1.02	6.21±0.80
	6x6	0.023	8.06±0.28	5.93±0.43	6.76±0.57	4.77±0.32
	8x8	0.040	6.29±0.39	3.76±0.46	4.29±0.56	3.98±0.41
	10x10	0.063	7.51±0.41	5.09±0.48	4.60±0.42	2.70±0.23
	32x32	0.648	7.99±0.21	2.56±0.24	3.32±0.29	2.22±0.15

**Table 3.1:** Stimulation charge-density thresholds obtained for RD10 mouse RGCs during stimulation at 10 Hz, 25 Hz and 40 Hz for various stimulation-area sizes (see Equation 3.8). Thresholds have been calculated as mean with their corresponding standard error. Only cells where sigmoidal threshold curves could be fit with good quality ( $r^2 \geq 0.9$ ) and that showed a minimum of spiking-rate modulation ( $dA \geq 2$  Hz) where included in the calculation. Thresholds  $x_{30}$  and  $x_{50}$  could only be calculated for cells that showed the required amount of spiking-rate modulation. The number of cells that could be used for the calculation was therefore sometimes smaller and in some cases these thresholds could not be calculated. The same is true for the standard error which requires a minimum two cells. Table 2 lists the corresponding numbers of cells used for the calculation.

	electrodes	area [mm <sup>2</sup> ]	$x_0 \pm \sigma$ [ $\mu\text{C cm}^{-2}$ ]	$x_{30} \pm \sigma$ [ $\mu\text{C cm}^{-2}$ ]	$x_{50} \pm \sigma$ [ $\mu\text{C cm}^{-2}$ ]	vs $x_0 \pm \sigma$ [ $\mu\text{C cm}^{-2}$ ]
10 Hz	2x2	0.003	2.16±nan	8.02±1.58	5.37±1.59	7.85±0.90
	3x3	0.006	8.27±1.34	7.91±1.70	11.18±2.68	8.40±0.79
	4x4	0.010	9.28±0.47	8.46±0.72	10.06±0.74	6.53±0.50
	5x5	0.016	8.72±0.38	5.16±0.86	6.53±0.79	5.71±0.52
	6x6	0.023	9.43±0.31	5.86±0.69	5.57±0.72	6.21±0.45
	8x8	0.040	7.78±0.28	4.20±0.83	4.61±0.90	3.24±0.44
	10x10	0.063	6.87±0.33	4.33±0.48	4.54±0.50	3.44±0.24
	32x32	0.648	5.64±0.25	2.58±0.35	2.98±0.42	1.91±0.18
25 Hz	2x2	0.003	8.79±1.42	4.88±2.49	6.17±6.17	7.21±0.64
	3x3	0.006	9.85±0.54	10.28±1.09	7.94±2.67	6.34±0.54
	4x4	0.010	7.95±0.37	5.36±0.64	7.52±0.83	5.07±0.42
	5x5	0.016	6.46±0.41	6.75±0.64	7.93±0.52	3.71±0.39
	6x6	0.023	7.54±0.35	4.99±0.54	5.64±0.61	3.16±0.27
	8x8	0.040	6.84±0.39	4.67±0.77	3.90±0.73	3.11±0.39
	10x10	0.063	6.22±0.32	4.06±0.40	4.57±0.45	2.41±0.21
	32x32	0.648	5.20±0.53	1.83±0.37	1.89±0.36	1.93±0.23
40 Hz	2x2	0.003	9.09±0.47	6.38±1.21	6.46±1.39	6.42±0.69
	3x3	0.006	7.56±0.79	5.23±1.07	7.14±1.02	4.83±0.56
	4x4	0.010	8.17±0.28	6.26±0.61	5.97±0.73	3.77±0.26
	5x5	0.016	6.47±0.47	5.75±0.63	7.64±0.64	3.39±0.34
	6x6	0.023	6.63±0.32	4.80±0.50	5.02±0.47	3.38±0.33
	8x8	0.040	6.66±0.48	3.07±0.57	3.52±0.58	2.05±0.40
	10x10	0.063	6.25±0.49	2.23±0.46	2.45±0.49	1.95±0.31
	32x32	0.648	4.49±0.38	1.03±0.24	1.61±0.31	1.43±0.30

**Table 3.2:** Stimulation charge-density thresholds obtained for C57BL6/J mouse RGCs during stimulation at 10 Hz, 25 Hz and 40 Hz for various stimulation-area sizes (see Equation 3.8). Thresholds have been calculated as mean with their corresponding standard error. Only cells where sigmoidal threshold curves could be fit with good quality ( $r^2 \geq 0.9$ ) and that showed a minimum of spiking-rate modulation ( $dA \geq 2$  Hz) where included in the calculation. Thresholds  $x_{30}$  and  $x_{50}$  could only be calculated for cells that showed the required amount of spiking-rate modulation. The number of cells that could be used for the calculation was therefore sometimes smaller and in some cases these thresholds could not be calculated. The same is true for the standard error which requires a minimum two cells. Table 3 lists the corresponding numbers of cells used for the calculation.

against a certain upper bound  $y_{\max}$ . This led to more or less arbitrary fits, since  $y_{\max}$  was not well defined. To still receive proper sigmoidal fits we performed two additional adaptations. First, we restricted fit values  $y_{\min}$  and  $y_{\max}$  to the interval of  $[A_{\min, \text{measured}}, A_{\max, \text{measured}}]$  for fitting to activity values. Second we created a virtual data-point  $A(2500 \text{ mV}) \equiv A(3000 \text{ mV})$  for the fitting procedure only to simulate saturation. Finally, we restricted our results to fits with  $r^2 \geq 0.9$  to guarantee high fitting quality. Fits with lower  $r^2$  were discarded.

- In the second approach we slightly varied the definition introduced in “Electrical multisite stimulation of the isolated chicken retina”(Stett et al. 2000). Two stimulation threshold were defined as the applied stimulus-intensity for which the observed corresponding activity reached an activity-threshold of 130 % or 150 % of the baseline activity  $A(0 \text{ mV})$ . Threshold values were called  $x_{30}$  and  $x_{50}$  respectively. This definition however heavily depends on the spontaneous activity rate of the cell. For cells with very low spontaneous activities the threshold can easily be crossed by noise alone while activity modulation for cells with high spontaneous activity rates did not reach  $x_{30}$  and  $x_{50}$  even though these cells were clearly affected by stimulation.

To compensate for the drawbacks of either definition, all three threshold values were calculated from data. Relative thresholds in units of  $x_0$  can be found in Table 3.3. For both mouse models spike-rate modulation thresholds  $x_0$  were larger than results for  $x_{30}$  and  $x_{50}$ . We did however observe differences in the number of cells for which thresholds could be calculated between RD10 and C57BL/6J. While variations for C57BL/6J were small (0.93 - 1.15), large differences were observed for RD10 (1.77 for  $x_{30}$  and 1.29 for  $x_{50}$ ). Finally we observed that results obtained for timing-modulation showed lower stimulation thresholds and higher cell-count compared to spike-rate modulation.

To compare thresholds for different electrode-sizes, we converted values from current-density to charge-density transmitted per half sine period.

$$q = \int_0^{\frac{T}{2}} i(t) dt = -c(f) \int_0^{\frac{T}{2}} \frac{dV_0 \cos(2\pi ft)}{dt} dt = 2c(f)V_0 = c(f)V_{0, pp} \quad (3.8)$$

Here  $V_0 = 2V_{0, pp}$  where  $V_{0, pp}$  is the peak-peak voltage. As an additional criteria we only took cells into account which could be identified over all measurements/for all electrode sizes. Additionally thresholds were compared with thresholds obtained by pulsatile stimulation (Corna, Herrmann, and Zeck 2018). Results are shown in Figures 3.14 and 3.15 and Tables 5 and 4. Thresholds obtained for sinusoidal stimulation were lower than thresholds  $x_{\text{pulsed}}$  presented by Corna, Herrmann, and Zeck 2018 for pulsed stimuli. We calculated thresholds for pulsed stimulation for electrode-sizes not included in the published data by linear interpolation between adjacent data points in order to compensate the mismatch between electrode sizes used in the publication and in our work. Sinusoidal thresholds for RD10 were between 1% and 49% of  $x_{\text{pulsed}}$ .

In the control experiment spontaneous activity of most cells vanished after adding DNQX and AP-7. Additionally sinusoidal stimulation no longer showed any effect on previously affected cells. After replacing the AMES/pharmaceutical blocker mixture with pure AMES-medium cell-activity returned as expected. Modulation of cell activity during sinusoidal stimulation could again be observed.

C57BL/6J			
$x_i$	median( $x_i/x_0$ )	median( $\sigma_i/\sigma_0$ )	median( $N_i/N_0$ )
$x_0$	1.00	1.00	1.00
$x_{30}$	0.67	1.53	1.15
$x_{50}$	0.73	1.68	0.93
$vs_{x0}$	0.52	0.83	1.60

RD10			
$x_i$	median( $x_i/x_0$ )	median( $\sigma_i/\sigma_0$ )	median( $N_i/N_0$ )
$x_0$	1.00	1.00	1.00
$x_{30}$	0.69	1.20	1.77
$x_{50}$	0.71	1.49	1.29
$vs_{x0}$	0.63	0.83	2.00

**Table 3.3:** Median of stimulation thresholds, standard error of the mean and cell count relative to results found for sigmoidal fitting, i.e. thresholds  $x_0$ . Calculation is based on results shown in Table 3.1 and 3.2 as well as Tables 2 and 3. Activity-modulation thresholds  $x_0$  obtained by sigmoidal fitting were larger than for  $x_{30}$  and  $x_{50}$ . Standard error of the mean however was lower.

Thresholds for vector-strength modulation and corresponding errors are lower, numbers of affected cells higher than their activity-modulation counterparts.

### 3.4.4 Chapter-discussion

We found that all spike-rate modulation threshold definitions yield results in the same order (see Tables 3.3). Thresholds obtained for  $x_0$  were larger than results for  $x_{30}$  and  $x_{50}$  in both mouse models RD10 and C57BL/6J. This indicates that induced differences in spiking-rate at maximum stimulus intensity relative to spontaneous spiking-rate were on average above 50%. Additionally spread in obtained threshold distributions for  $x_{30}$  and  $x_{50}$  was larger compared to  $x_0$ . We address variances in the spontaneous activity levels within the recorded cell-population, due to the high dependence of  $x_{30}$  and  $x_{50}$  on the spiking baseline. Inhibitory and excitatory photoreceptor coupling contributions increase this spread even further for C57BL/6J mice compared to RD10. The number of cells for which thresholds could be calculated showed only small variations with respect to the threshold definition used for wild-type retina (15% more cells for  $x_{30}$  and 7% less cells for  $x_{50}$  relative to the number of obtained thresholds for  $x_0$ ). There were

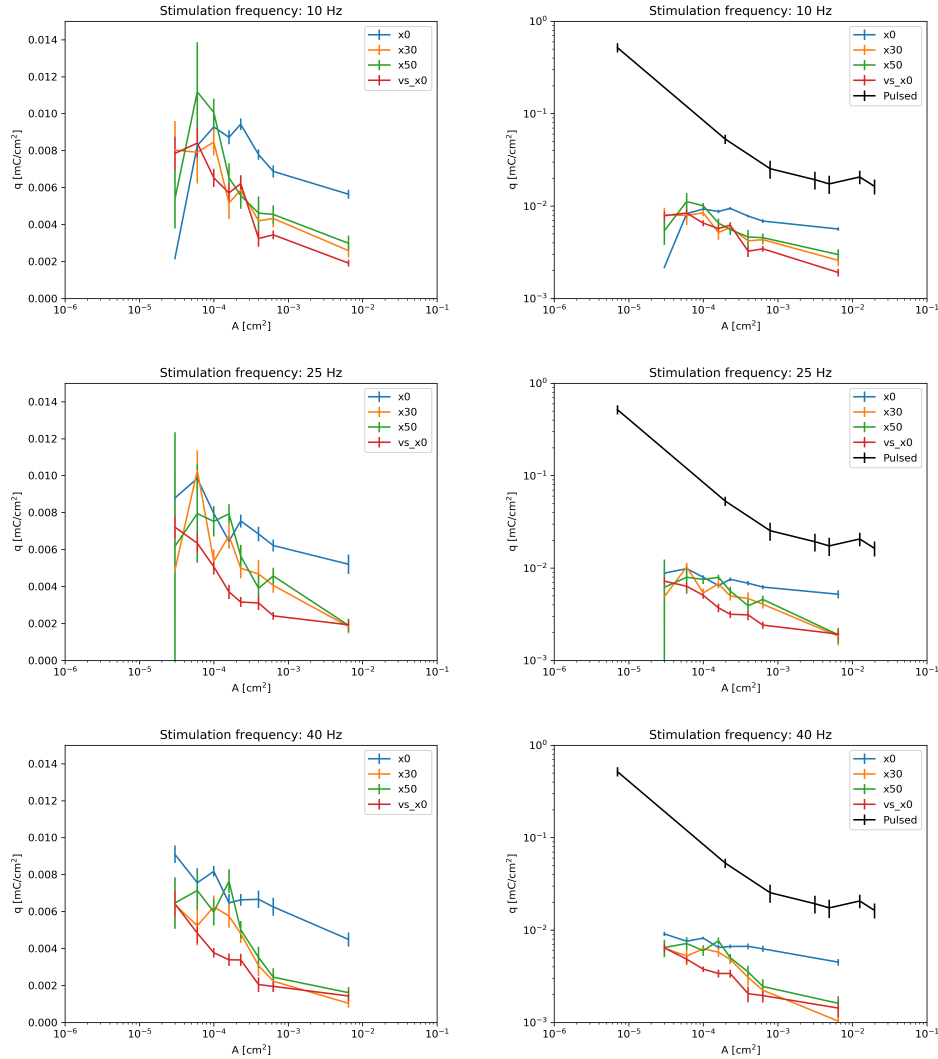


**Figure 3.14:** Illustration of thresholds obtained with sinusoidal stimulation of C57BL6/J retina. *Left:* Thresholds for different stimulation frequencies and electrode-sizes. Different thresholds for activity were plotted as well as thresholds obtained for VS. Activity thresholds show very good overall agreement independent of how they were obtained. Differences show only for very small electrode sizes where number of cells was low. VS thresholds were well below activity thresholds in all experiments. *Right:* Activity-thresholds for the same data-sets as on the left-hand side but in a double-log scale. The black line shows activity-thresholds obtained with pulsatile stimulation published by Corna, Herrmann, and Zeck 2018. Sinusoidal thresholds are below pulsatile thresholds by approximately an order of magnitude (for exact values refer to Table 5).

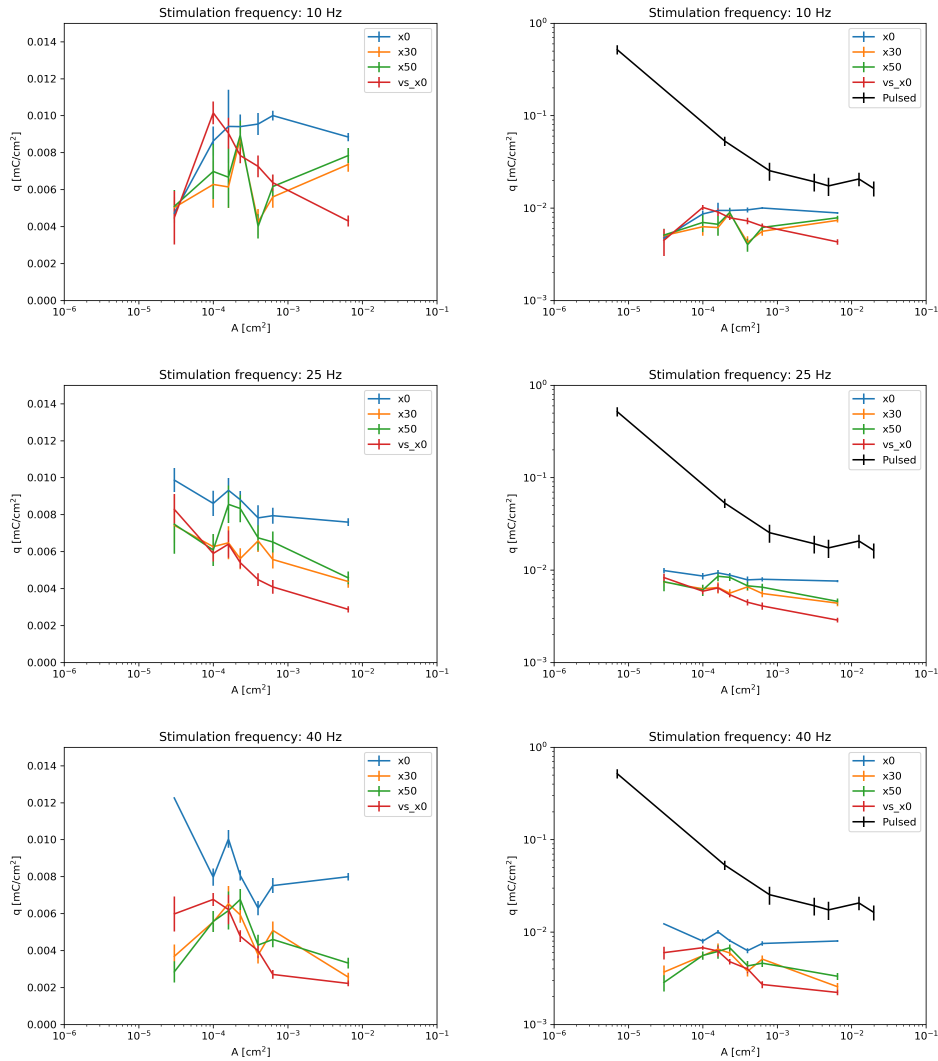


**Figure 3.15:** Illustration of thresholds obtained with sinusoidal stimulation of RD10 retina. *Left:* Thresholds for different stimulation frequencies and electrode-sizes. Different thresholds for activity were plotted as well as thresholds obtained for VS. Activity thresholds show very good overall agreement independent of how they were obtained. Differences show only for very small electrode sizes where number of cells was low. VS thresholds were well below activity thresholds in all experiments. *Right:* Activity-thresholds for the same data-sets as on the left-hand side but in a double-log scale. The black line shows activity-thresholds obtained with pulsatile stimulation published by Corna, Herrmann, and Zeck 2018. Sinusoidal thresholds are below pulsatile thresholds by approximately an order of magnitude (for exact values refer to Table 4).

however 77% more cells for which thresholds could be obtained using  $x_{30}$  and 29% more cells using  $x_{50}$  compared to the number of thresholds obtained using  $x_0$ . By definition  $x_0$  can be obtained for any cell and the only criteria for discarding these thresholds are restrictions to the fitting parameters  $r^2$  to values  $r^2 \leq 0.9$ . We considered the following three explanations: First, restrictions to  $r^2$  were too conservative excluding too many cells which were actually stimulated. This could be a result of spiking-noise (e.g. spontaneous activity). Second, cells were affected but showed a diminishing spiking-rate at higher intensities (see Figure 3.13). We exclude this scenario as we only found a very low number of these cells when screening our results. Third, cells were not affected by stimulation but spiking-noise led to false positives of  $x_{30}$  and  $x_{50}$ . We cannot exclude the latter especially for low spontaneous activity cells, where the 30% or 50% thresholds are exceeded rather quickly. At the same time lower spontaneous activity results to a lower chance to observe superpositions of induced spikes and spontaneously occurring spikes, even more so as we obtain values by averaging over 5 recordings. Inspecting of plots for single cells confirmed our suspicion that an r-value of  $r^2 > 0.9$  results in discarding of apparently stimulated cells in a number of cases. However we also found that this restriction removes a number of false positives. We therefore argue that this restriction is a justified tradeoff which improves threshold quality at the cost of cell-count.

All spiking-modulation thresholds were well below results published for pulsed stimulation regardless of the threshold definition (Corna, Herrmann, and Zeck 2018). We use  $x_0$  when comparing thresholds to results published by Corna, Herrmann, and Zeck as thresholds for pulsed stimulation were also derived by sigmoidal fitting. Sinusoidal thresholds for RD10 were between 1% and 49% of  $x_{\text{pulsed}}$ . A complete overview of relative thresholds is given in Table 4. We assume, that lower thresholds originate from modulation and synchronizing of presynaptic input to RGCs. Lower stimulation thresholds would result in a reduction of energy needed per induced RGC activation and thus reduce energy consumption of implants. This could reduce the frequency of battery-charging and at the same time increase battery life-time. Modulation of RGC spiking by activation of the presynaptic circuitry should also result in higher spatial resolution as it avoids stimulation of axons of passage. This was confirmed by our experiments as no off-site RGCs were activated during stimulation while using small electrode subsets, e.g. 6x6 electrodes. This finding is in good agreement with results published for spatial-resolution enhancing effects of increased stimulus pulse duration (Weitz et al. 2015a)

A most notable outcome of our experiment was the timing modulation of RGC spiking, which occurred at even lower stimulus intensities. As previously introduced, vector-strength is in this work used as a parameter to measure timing-precision of RGC activity during sinusoidal stimulation usually recorded over multiple periods. It is not a sufficient criterion for high vector-strength that RGC activity occurs with a temporal-precision during a specific phase, but activity recorded out of phase also needs to be low. In our case this out of phase activity is spontaneous activity which can also be understood as

background noise. We observed not only high reliability of sinusoidal stimulation, but also high vector-strength in our experiments. Therefore activity out of phase was also reduced. Surprisingly vector-strength was already modulated as much lower stimulus intensities than RGC spiking-rate.

Obtained thresholds vs  $x_0$  and standard errors of the mean were smaller, number of affected cells larger than results for any of the spiking-rate modulation thresholds. VS thresholds were only 1%-24% of corresponding spiking-modulation thresholds  $x_0$  obtained for RD10 and 1.7%-12% of thresholds  $x_0$  obtained for C57BL/6J (Note that we used a sigmoidal fit approach to obtain thresholds as upper and lower limits for vector strength are well defined. We therefore intrinsically overcome restrictions faced for activity modulation thresholds. Alternative threshold definitions are therefore obsolete.)! We therefore assume that at this point no additional activity was induced, but existing fluctuations in BPC potentials (the origin of spontaneous RGC activity) were synchronized. This could open the field for new applications of electrical stimulation, i.e. by synchronizing spontaneous activity rather than inducing new spikes. This is especially interesting since spontaneous activity is much more abundant in blind retina. Sinusoidal stimulation below spiking-modulation threshold but above VS thresholds could various benefits:

1. Transmission of information to the brain by synchronizing output (timing-modulated spontaneous activity) of affected cells.
2. Improving of signal-to-noise ratio by suppression / timing-modulation of spontaneous activity.
3. Lowering of power needed for electrical stimulation.

We conclude this section by discussing limitations of our experimental setup and methods used as well as potential chances for future work. The first limitation is the overall relative rough alignment of stimulation area and affected cell-network. We only considered RGCs located directly above stimulation area for analysis during variation of stimulation area sizes. We did however not map the spatial receptive field of the RGC. As sinusoidal stimulation acts not directly on the RGC, stimulation areas should have been aligned with the receptive field rather than the RGC soma. We should obtain different stimulation thresholds for cells where only half of the receptive field integrates charge compared to receptive fields that are centered above the stimulation electrodes and therefore integrate nearly all transmitted charge. These effects should however not necessarily result in a bias to larger stimulation thresholds, as the same consideration is true for inhibitory input of the surround. Future experiments should nevertheless consider these effects and include appropriate adaptations.

Second, we did not distinguish between the various cell-types found in the retina (Baden et al. 2016; Carciari, Jacobs, and Nirenberg 2003; Zeck and Masland 2007). While those cell-types might differ in the morphology of the RGC itself, they also differ in their presynaptically connected cell-network. We assume that strong variability among



stimulation thresholds were to be expected given the variety of AC- and BPC-types, connections thereof and resulting effective physical properties of the circuitry. If this interpretation of our observations is correct then these variations might also offer an opportunity to cell-type specific stimulation. Future experiments towards this goal would need to include two major modifications:

1. Applied protocols for sinusoidal stimulation should consist of finer granulated intensity steps and cover a larger total intensity range. While artefact-free simultaneous stimulation and recording was limited to the voltage range between 0 V to 2.65 V (using  $V_{\text{source-gate}} = -650 \text{ mV}$ ) resulting intensities seemed to be large enough for stimulation of all cells. We found however that some cells showed a decrease in spiking-rate at higher stimulus intensities after an initial increase at lower intensities. This behavior might also be specific for certain cell-types. Since we cannot rule out that other cell-types show similar behavior at higher, yet (with our system) inaccessible intensity ranges we consider it important for future experiments to extend this window to higher intensities. Additionally choosing finer granulated steps allows obtaining thresholds at higher accuracy.
2. RGCs may need to be classified, e.g. using the protocol presented by Baden et al. 2016. However this gives rise to new challenges. Previously mentioned classification relies on optical stimulation consisting of amplitude- and frequency-modulated sinusoidal intensities and an additional moving-bar to detect direction selectivity. Calcium imaging was used to obtain RGC activity levels and classify cells. The CMOS-MEA 5000 chips are sensitive to light in the blue regime as described in the previous sections. Wavelength in the blueish regime are typically used for stimulation of mouse retina. We think removing of resulting stimulus artifacts as previously described could be challenging due to the high temporal variability and high frequency components of the stimulus. Artifact suppression using high-pass filters worked well while frequency components of the stimulus and spikes were well separated, but if both spectra overlap different approaches might have to be taken. The circuitry of CMOS-chips is however also affected by light at longer wavelengths if intensities are large enough. This could be the case using calcium imaging. We therefore consider this technique to be limited in combination with the CMOS-system. The obvious solution would be to use CMOS-recordings for classification of RGCs. It has however to be tested if this approach yields the same results. Finally, classification based on cell-response to optical input is not feasible using blind-retina.

## **3.5 Circuit-specific stimulation**

We found differences in the preferred response phase to sinusoidal stimulation amongst RGCs during our work on the previous section. We hypothesized that these variations are a result of variations in the presynaptic circuitry. One aspect which could introduce such a variation is the stratification of BPC dendrites to different layers of the IPL as described in Section 1.2. ON- and OFF-type BPCs have dendrites of different vertical extent. These dendrites experience different voltages along the vertical axis if exposed to the same electric field. This introduces variations in BPC output and as a result variations in the input of ON- and OFF-type RGCs induced by electric stimulation. We therefore decided to investigate if variations in mean-response phases found in the previous section correlated with ON- and OFF-type BPC functionality and if so, whether these distinctions could be used towards circuit-specific electrical stimulation in blind retina.

It became clear in early analytical stages that our working hypothesis was not correct and we didn't dive any deeper. We still show our results here however incomplete as of this section's importance to understanding the complete scope of this thesis: Investigating effects of optical stimulation on CMOS-recordings and effects of sinusoidal stimulation on the neuronal network of the retina. This experiment links both aspects and shows one of many possible applications of high-density CMOS-MEAs.

### **3.5.1 Abstract**

Here we investigated correlations of circular mean-phase obtained for sinusoidal stimuli with bias- and transient-indices obtained from optical stimulation. Healthy C57BL6/J mouse retina was interfaced with CMOS MEAs. Optical flicker stimuli of blueish light were shown to the retina at rates of 1 Hz with a duty-cycle of 50%. Cells were classified in ON and OFF cells based on obtained bias indices. Mean-response phase of RGC to sinusoidal stimulation at 10 Hz and 25 Hz using 2.5 V were extracted. ON and OFF cells had different mean-response phase. We hypothesized that these phase- or timing-differences could be used for separate stimulation of both circuits. Same procedure was repeated for blind RD1 mice, but no splitting of mean-response phase was found.

### **3.5.2 Materials and Methods**

C57BL6/J mouse retina was extracted and interfaced with CMOS MEAs as described in Section 2.1.2. Optical on/off flicker stimuli of 470 nm wavelength were presented to the retina at a rate of 1 Hz with a duty-cycle of 50%. Stimuli were generated using the CoolLED pE-4000 system and the Rapp Optoelectronics  $\mu$ -matrix system introduced in

Section 2.2.2. Stimuli were projected on the sensitive area of the CMOS-chip using a  $10\times$  objective and 5% of the maximum light intensity. This resulted in intensities of approximately  $32 \mu\text{W mm}^{-1}$ , which is in the photopic regime (Tikidji-Hamburyan et al. 2015). Drift artifacts resulting from optical stimuli were removed as previously described. Data was spike-sorted and BIAS and transient indices were calculated for all cells. The BIAS-index is defined as

$$\text{BIAS} = \frac{N_{\text{ON}} - N_{\text{OFF}}}{N_{\text{ON}} + N_{\text{OFF}}}, \quad (3.9)$$

where  $N_{\text{ON}}$  and  $N_{\text{OFF}}$  are the number of action potentials observed during illumination or after illumination respectively. ON-OFF-cells have a bias index around 0, while ON-cells have positive and OFF-cells negative bias indices. To have a clear separation into ON and OFF cells, we here termed cells with  $\text{bias} \geq 0.6$  ON-cells while cells with  $\text{bias} \leq -0.6$  were termed OFF-cells. Cells with bias-indices  $-0.6 < \text{bias} < 0.6$  were not taken into account for evaluation and were discarded.

Cells were then stimulated electrically using sinusoidal stimuli of 2.5 V at frequencies of 10 Hz and 25 Hz. Stimulation artifacts were removed as described in Section 2.3.1. Data was then spike-sorted and analyzed using circular statistics. For each cell the mean-response phase was calculated.

Retina of RD1 mice was extracted and interfaced with the CMOS-MEA using the same techniques as for BL6 mice. Stimulation thresholds and mean-phase values were obtained using the same stimulus and filtering protocols as previously described.

### 3.5.3 Results

Results for BL6-mouse retina showed preferred mean-response phases correlating with the cells' BIAS index (see Figures 3.16 and 3.17). The resulting mean phase-distribution was broad and continuous. Reducing the cell population to clear ON- and OFF-cells ( $|\text{bias}| \geq 0.6$ ) resulted in two distinct peaks which showed high correlations with ON- and OFF-cells. The mean phase distribution for RD1 cells showed a single, relatively narrow peak (see Figure 3.18).

### 3.5.4 Chapter-discussion

Observed differences in mean-response phase  $\bar{\alpha}$  between ON- and OFF-pathway RGCs of wild-type mouse-retina were in good agreement with previous publications (Twyford and Fried 2016). We tried to use this behavior to selectively activate both pathways. First promising results towards this goal were already published (Twyford, Cai, and Fried 2014). We did however not observe splitting of RGC mean-response phase  $\bar{\alpha}$  in RD1 retina. We address this to the lack of PR coupling in contrast to experiments using wild-type retina. Additional differences may arise due to rewiring effects on PR-degeneration,

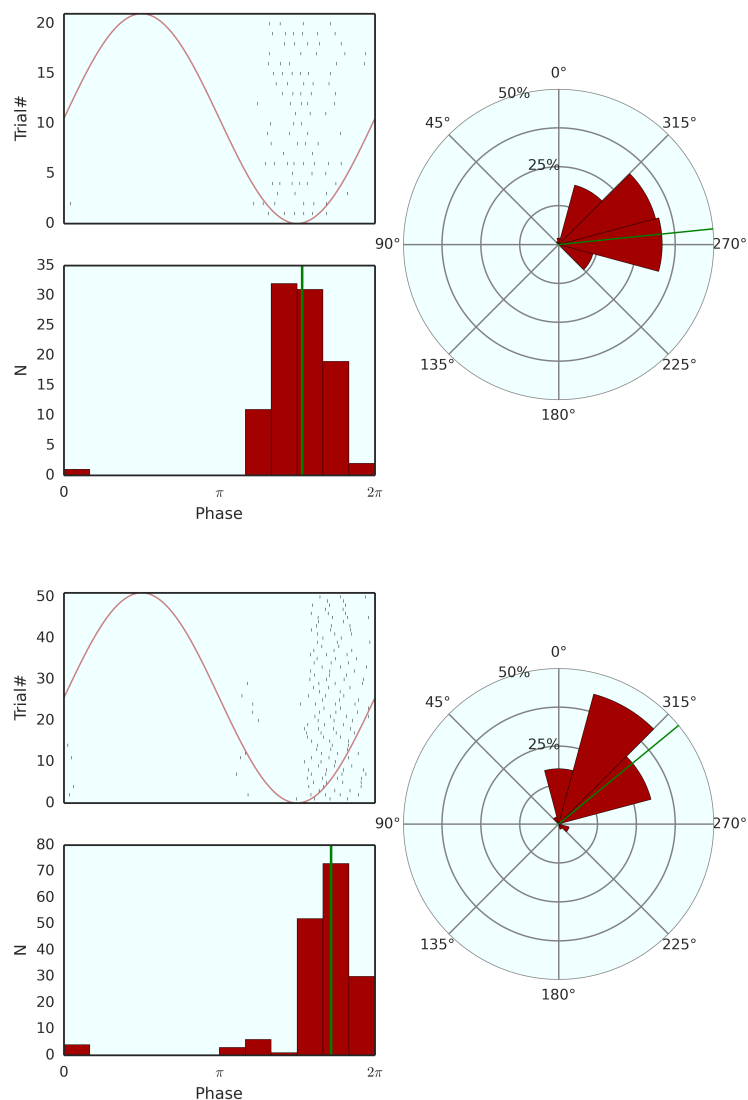


**Figure 3.16:** Conventional peristimulus time histograms-Diagrams (PSTH) (left) and PSTH in polar coordinates showing activity recorded from the same RGC during 10 Hz (*top*) and 25 Hz (*bottom*) sinusoidal stimulation. Retina was obtained from healthy BL6-mouse. *Left column:* Spikes recorded during continuous sinusoidal stimulation for 2s. Phase of single stimulus periods is plotted on the x-axis, while stimulus repetitions are plotted on the y-axis. Each recorded spike is marked as a dot. PSTHs are then created. *Right column:* PSTH in polar coordinates. Mean-response phase is indicated by the green line.

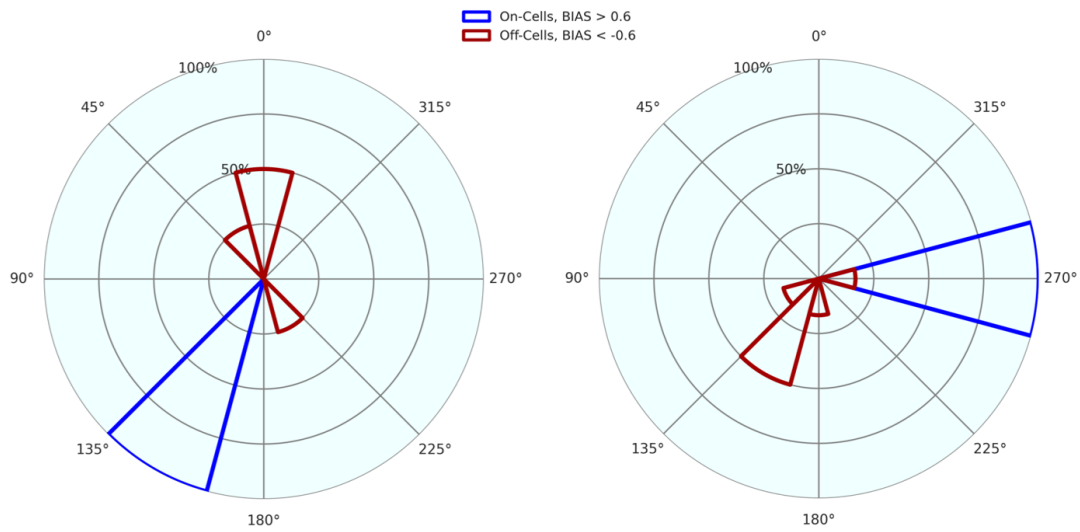


**Figure 3.17:** Mean-phase values for BL6-mouse ON- and OFF-RGCs during 10 Hz (*left*) and 25 Hz (*right*) sinusoidal stimulation at 2.5 V. Previously obtained mean-phase values were plotted as histograms in polar coordinates. Distinct histograms were created for ON- (blue) and OFF-cells. Differences in preferred mean-phases between both populations are clearly visible.

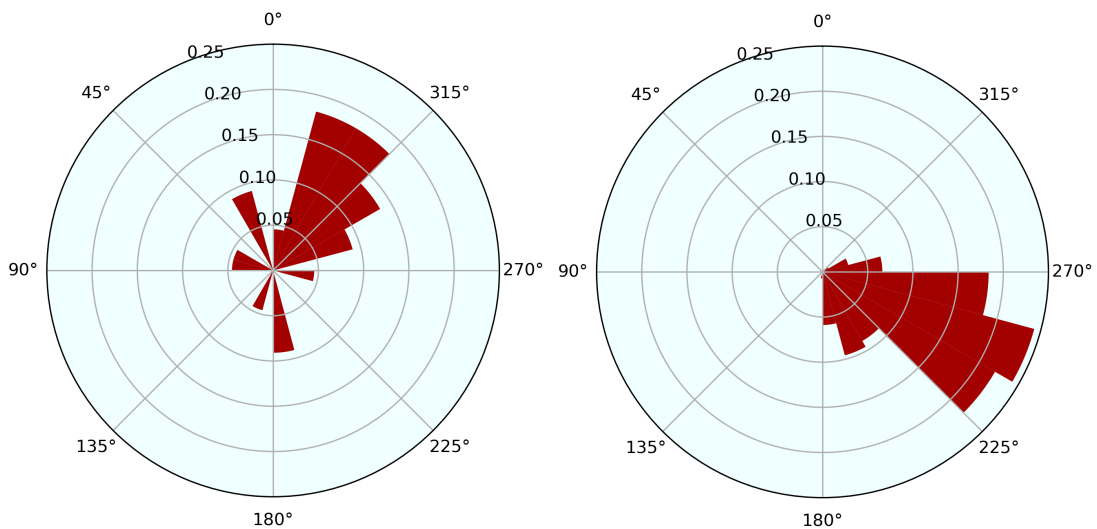


**Figure 3.18:** Mean-phase histograms obtained for RD1 mouse RGC activity during sinusoidal stimulation at 2.5 V using frequencies of 10 Hz (*left*, 22 RGCs) and 25 Hz (*right*, 136 RGCs). Results were calculated using 5 different retina slices extracted from distinct animals. A clear preference for mean-response phase was visible contradicting our working hypothesis.

especially as this degeneration starts in RD1 previous to fully establishing of the retinal-network (Jones and Marc 2005).

We hypothesize that sinusoidal transmembrane potentials of the BCs network become highly synchronized by sinusoidal stimulation. This synchronicity translated to the timing of RGC spiking, as RGCs integrate synchronized BPC input. Differences in BPC and RGC cell-types, receptive-field sizes, and AC-coupling result in a broadening of the distribution but not in resolvable distinction of individual peaks.

For wild-type retina there's the additional contribution of PR stimulation. Release of glutamate by PRs should also be synchronized by sinusoidal stimulation. However the sign of resulting contributions to postsynaptic BPC transmembrane potentials is determined by the type of synaptic connections between PR and BPC, i.e. by ionotropic or metabotropic receptors. BC potentials therefore split into  $V(t) \pm X(t)$  where  $X$  stands for the PR's contribution and the sign depends on the synaptic type. RGC activity splits in preferred phases accordingly.

While circuit-specific stimulation could not be achieved with our approach, we still think that it is a feasible goal. We address the most fundamental error in our approach to the relatively rough cell-classification based on bias-indexing. A much more accurate classification algorithm was introduced in the work of Baden et al. 2016. This RGC classification is based on functional classification based on the features of the optical input encoded in the RGC's activity pattern. It captures a lot more information than a simple bias-/ transient-index based ON/OFF classification. This detailed distinction between RGC type should result in a classification in distinct presynaptic circuitry types. As a consequence physical properties of these circuitry should also separate into clusters. It is therefore highly likely that these circuits show distinct characteristics of the integration of transient-electrical fields. It would be interesting to see if future work in this field could use electric chirp stimuli to distinguish cell-types.

## **3.6 Effects of continuous sinusoidal stimulation**

One of the limiting factors for the use of retinal implants are observed adaptation effects of the retina to repeated pulsatile stimuli at frequencies above 5 Hz. Results are vanishing RGCs responses to repetitive stimuli. This is also referred to as fading (Jensen and Rizzo 2007). An important aspect of future stimulation protocols is therefore to overcome these restrictions.

### **3.6.1 Abstract**

Here we analyzed RGC response to continuous sinusoidal stimulation at 10 Hz, 25 Hz and 40 Hz for up to 10 min. Measurements of spontaneous activity were performed to obtain baselines for all cells previous to stimulation onset. The retina was then exposed to continuous sinusoidal stimulation and recordings were taken at defined time intervals. Again recordings of spontaneous activity were performed after stimulus offset. Effects of sinusoidal stimulation were analyzed regarding two different aspects:

1. Effects of stimulation within the first few seconds of stimulation.
2. Long-term average stability of spiking-rate, reliability and vector-strength for cell populations.

Initial response-strength in terms of induced spikes per stimulus-period remained almost constant for the first 1 s of continuous stimulation. After the first second the overall amount of active cells started to decay and saturated at a level of about 10%. For the remaining cell population reliability of response to electric stimulation remained high which is in contrast to previous publications using pulsatile stimulation at comparable frequencies (Jensen and Rizzo 2007).

### **3.6.2 Materials and Methods**

A RD10 mouse retina was interfaced with the CMOS-chip as described in Section 2.1.2\*. Previous to onset of electrical stimulation a 3 s recording of spontaneous activity was performed to obtain baseline-activity values for all cells. Then continuous sinusoidal voltage traces of 10 Hz, 25 Hz and 40 Hz with 2 V and 2.5 V were applied to all stimulation electrodes. Recordings of 3 s duration were performed every 1 min starting with stimulation onset for experimental duration of 10 min. After stimulation stopped recordings of 3 s were taken.

Data was pre-processed for data-analysis by applying of filtering protocol as described in Section 2.3.1. Filtered recordings were then spike-sorted.

---

\* We performed 12 recordings of 3 s for each of the 6 different parameter sets. This resulted in an overall data volume of 42.2 GB. Recordings had to be filtered, spike sorted, post-processed and evaluated, which was a most time consuming procedure. The extend of this experiment therefore limited the number of retinas which could be performed in the frame of this work. Additional recordings would be required for a more significant evaluation. Additional hardware and performance optimization of software tools could accelerate this process. Results of predecessor experiments on smaller parameter sets however indicated similar behavior.

### **3.6.3 Results**

We started by investigating the first recordings aligned with stimulation onset with respect to adaptation effects to applied stimuli. First, activity recorded was separated into stimulus period sized bins. Then spiking-rate per stimulus period was normalized to spiking-rate recorded during the first stimulus period and plotted against stimulation time (see Figure 3.19). We observed that normalized spiking-rate remained constant for all recordings within approximately the 1 s of stimulation. This initial period was followed by a phase of decay of the spiking-rate. This drop off occurred at the same time across all applied frequencies and amplitudes.

We continued by investigated if observed decay was a result of a decrease of the total number of spiking cells or if it was a result of a decrease of the mean spiking-rate of the whole cell population. Towards this goal we calculated the number of responding cells per period, normalized it to the initial number of responding cells during the first stimulus period and plotted it against stimulation time. The resulting Figures 3.20 showed a high consistency to previously shown Figures 3.19. This indicates that the observed decay in spiking-rate was a result of a silencing of a subset of the overall cell-population. Finally we analyzed stability of cell-response to continuous stimulation over the complete stimulation duration of 10 min. We therefore calculated activity, vector-strength and reliability for each 3 s recording separately and plotted the results against stimulation time. Results are shown in Figure 3.21. We observed little effect of sinusoidal stimulation on RGC spiking rate across all frequencies used in this experiment. At the same time a strong up-regulation of vector-strength indicates a strong timing-modulation. We additionally observed that reliability was increased during stimulation for 25 Hz and 40 Hz but not for 10 Hz.

### **3.6.4 Chapter-discussion**

Results obtained by previously described experiments are now compared to results obtained by Jensen and Rizzo 2007 for pulsed stimuli. While our scope was focused on analyzing of stimulation effects over extended durations, data obtained for cell-behavior on stimulus onset is comparable to results shown in Figure 3.22.

For pulsed stimuli normalized RGC response to stimuli at frequencies above 2.5 Hz was diminished (Jensen and Rizzo 2007). Observed diminishing effects for the response to the second applied pulse ranged from 10% at 4 Hz stimulation rate to 94% at 65 Hz stimulation rate. This is in contrast to our results obtained for sinusoidal stimulation. We did not observe strong diminishing for any of the applied stimulation frequencies & amplitude pairs within the first second of stimulation (10-40 stimulus repetitions, depending on stimulation frequency). We did however observe slight increases in the normalized RGC response of 17% at 2 V and 19% at 2.5 V for stimulation at 10 Hz during the second stimulus period (in contrast to approximately 15% diminishing reported by Jensen



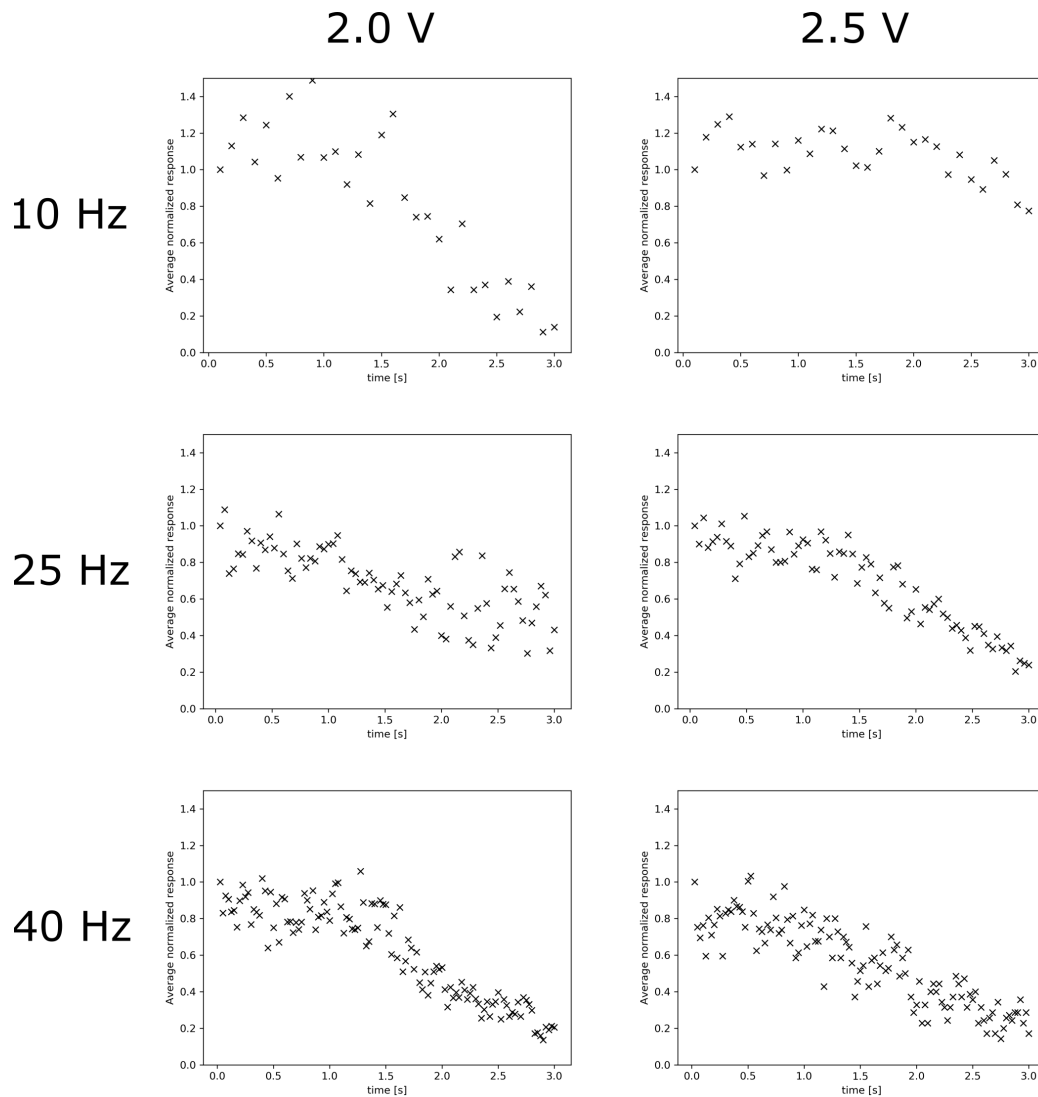


**Figure 3.19:** Illustration of normalized response averaged for all observed cells for each stimulus period during the first 3s of stimulation. Activity was measured as the number of spikes observed for each stimulus period. All obtained values were then normalized to the activity observed during first stimulus period for the corresponding cell. Cells which showed no activity during the first stimulus period were excluded from the evaluation. Figures are organized in two columns: The left hand column shows recordings using 2.0 V peak-peak amplitude and the right hand side shows recordings obtained for 2.5 V stimuli. Figures in each row share the same stimulus frequency. These are from top to bottom: 10 Hz, 25 Hz and 40 Hz.

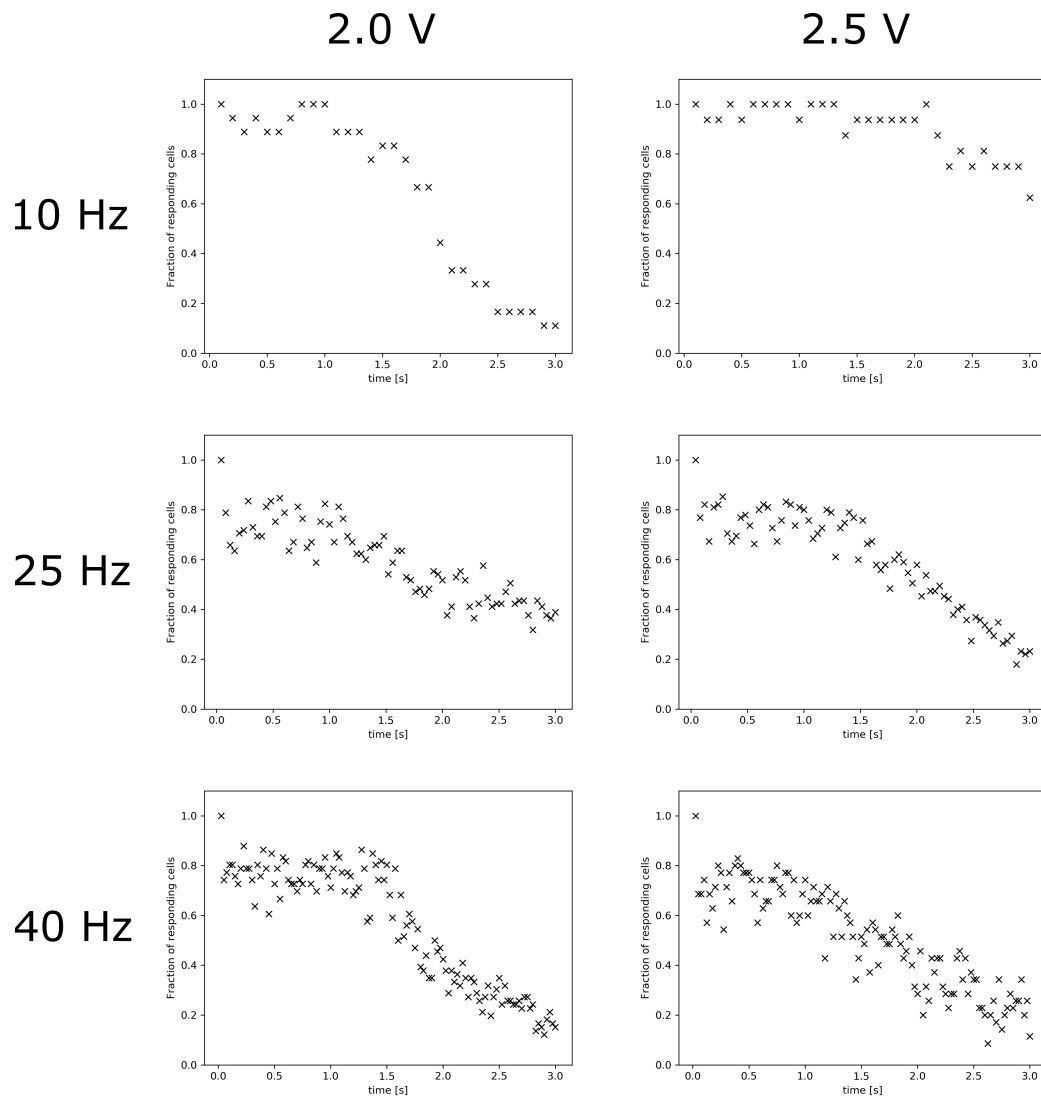


**Figure 3.20:** Illustrations show fraction of responding cells per stimulus period during the first 3 s of stimulation. These are from top to bottom: 10 Hz, 25 Hz and 40 Hz. Figures in the left hand column were created from recordings during stimulation using 2 V amplitude while figures in the right hand column were created from recordings during stimulation using 2.5 V amplitude.

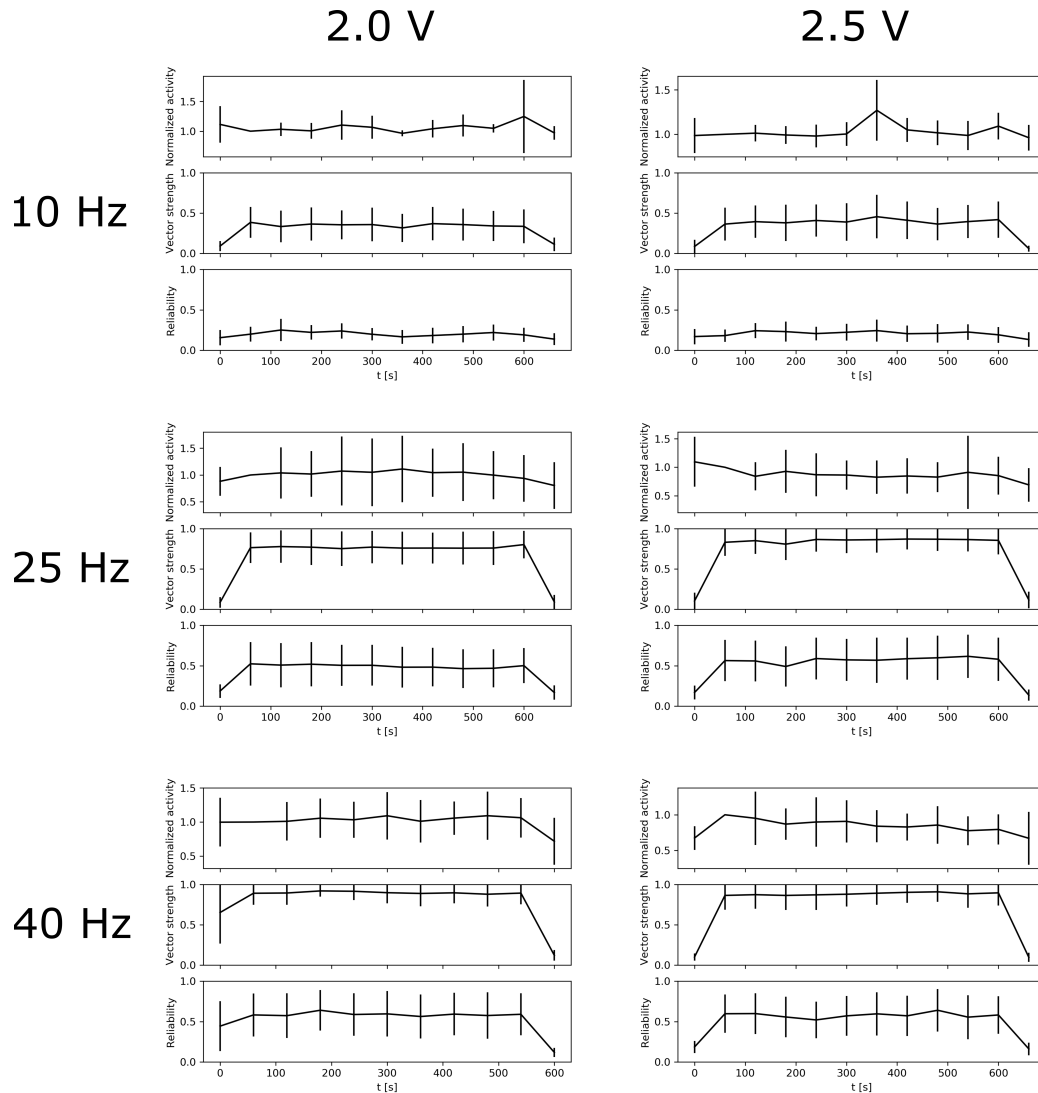


**Figure 3.21:** Illustration of effects of continuous stimulation. Recordings in the left column were performed during stimulation with amplitudes of 2.0 V while the amplitudes of 2.5 V were used for the right hand column. Figures in each row shared the same stimulation frequency. From top to bottom frequencies of 10 Hz, 25 Hz and 40 Hz were used. All stimuli lasted 10 min.

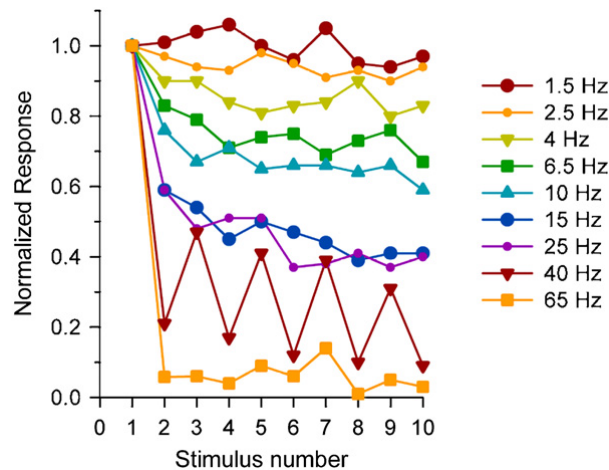


**Figure 3.22:** Cell response to pulsatile stimulation at various frequencies. Pulse duration remained the same for all frequencies, but inter pulse intervals decreased with increasing frequencies. Adaptation effects to high-frequent stimuli are clearly visible. *Source: Jensen and Rizzo 2007*

and Rizzo 2007). For 40 Hz we observed diminishing of the RGC response of 18% (2 V) and 24% (2.5 V) during the second stimulus period (in contrast to 80% diminishing reported by Jensen and Rizzo 2007). However due to differences in calculation of response strength in both cases, spontaneous activity should have a larger impact on sinusoidal stimulation (In our experiments all recorded spikes were included in the spiking rate due to the continuous nature of sinusoidal stimulation. In the work of Jensen and Rizzo 2007 only spikes of the first burst following the stimulation pulse were included in the analysis). We therefore address small fluctuations in the average normalized response in our experiments to spontaneous activity rather than adaptation effects. Clear adaptation effects were only observed for stimulus durations exceeding 1 s to 1.5 s. This highlights the previously mentioned expected difference in the coupling mechanism of both sinusoidal (indirect stimulation via presynaptic stimulation of RGCs) and pulsatile stimulation (direct stimulation of RGCs) on the neuronal network.

Adaptation related activity reduction to static images, i.e. constant activation, is an expected and physiological correct behavior. Declining of induced spiking-rate after 1 s to 1.5 s is therefore not necessarily a limiting factor for retinal implants. In contrast making the temporal regime of tens to hundreds of ms accessible for repetitive, reliable stimuli at frequencies above 5 Hz is a huge advantage compared to currently used pulsatile stimulation protocols.

Next we analyzed the effects underlying the decay of induced activity after this initial stable period. We therefore calculated the fraction of cells with  $A(n) < 0$  for each sinus period  $n$  and plotted it against time (see Figure 3.20). Again a clear decay which correlated with the activity decay was visible. This decay could have two origins:

1. Single cells becoming completely silenced and vanishing. This would reduce the total number of active cells.
2. The overall spiking-rate of certain cells is reduced and/or cells start skipping stimulus periods. This would reduce the average activity while keeping the total number of active cells per recording constant.

Combinations of both were also possible and we actually expected to observe this due to the huge variety of different cell-types, cell-networks and their resulting physical properties. A logical next step would thus have been to track and identify cells across recordings and analyze their behavior. This however proved to be infeasible with our current methods for a number of reasons:

1. The spike-sorter used in this work was developed for relatively short recordings, i.e. recordings of several seconds of neuronal activity. One simplistic assumption that could be made for this scenario was that spikes have a relatively static shape or a shape that does not change with time. As our recordings were a minute apart from one another we had to assume (and also observed) that this was not the case. Identification of cells across recordings based on the wavelet was therefore not possible.
2. Due to the discrete nature of recording electrodes an exact positioning of the cell on the CMOS-MEA is impossible. The cell-center was calculated as the center of charge of the recorded activity per cell by the spike-sorter. This center of charge may vary since the temporal and spatial shape of spikes are affected by fluctuations and dynamics. Additionally the retina may drift slightly on the CMOS-MEA during or between recordings. Finally cell-densities in the order of 1000 cells/mm<sup>2</sup> prevented precise cell identification in most cases even if the cell-position is only shifted by one electrode between recordings.
3. The spike-sorter used in this thesis does not work completely unsupervised. Adapting of thresholds and distinction between spike and artifact are at least partially performed by humans. Distinguishing between cells that do not appear in recordings due to silencing and cells that could either be not identified or were mistakenly classified artifacts.

Finally we analyzed the behavior of the whole cell-population across all recordings using parameters activity, vector-strength and reliability (see Figure 3.21). 10 Hz stimulation showed little / no effects on spiking rate modulation for both applied amplitudes. This was not unexpected since induced bath-currents are proportional to the applied stimulation frequency. Effects would be expected to appear at higher voltage amplitudes. This voltage regime could however not be accessed with the setup used in this work. While spiking-rate remained unaffected, vector strength was increased on stimulation onset. The increase was not as drastic as for higher stimulation frequencies. This effect can also be explained with the frequency dependance of the stimulation current, but is

more likely also a of higher impact of spontaneous activity on vector-strength for lower frequencies.

We did not observe increases in activity for 25 Hz and 40 Hz, which was unexpected given thresholds derived in Section 3.4. Initial increases in spiking-rate were averaged out by adaptation effects. Observed increases in vector-strength and reliability were stronger than in results obtained for 10 Hz stimulation. In contrast to activity modulation there were no adaptation effects for timing modulation. Finally after stimulation offset cells responded with a drastic drop in reliability as well as in vector strength with very little variation. As activity did not show such a drastic drop we can conclude that turning off stimulation did not result in a complete silencing of the cells. However spiking occurred clearly out of the preferred phase as reliability and vector-strength were close to zero.

To conclude we summarize the following main findings:

1. Sinusoidal stimulation does induce stable RGC spiking within 1 s to 1.5 s after stimulus onset independent of the stimulation frequency. After this initial period RGCs show adaptation effects which results in a decay of the spiking-rate. This is in strong contrast to pulsed stimuli, which result in down-regulations of the number of induced spikes starting from the first stimulus repetition at comparable frequencies (Jensen and Rizzo 2007).
2. We did not find any adaptation effects to timing-modulation of RGC spiking. Sinusoidal therefore provides high temporal precision at least for up to 10 min of stimulation.
3. We observed mean-reliability values of approximately 0.5 for continuous sinusoidal stimulation at 25 Hz and 40 Hz, indicating that RGCs only responded to every second stimulus on average. This is similar to the results of Jensen and Rizzo 2007 for 40 Hz pulsed stimulation.

## **3.7 Encoding of letter-shaped objects**

### **3.7.1 Abstract**

The next experiment was designed as a simple proof of principle with the idea of using sinusoidal stimulation in retinal-implants. While temporal robustness was shown in the previous experiment this experiment aimed at testing spatial-selectivity of applied stimuli. One to two different letter-shaped stimulation areas were selected and connected to different stimulus generators. Surrounding areas were connected to a third stimulus generator as a background. At first all stimulators showed the same low-intensity stimulus for 1 s. Then both letter-shaped electrodes present a short increase in intensity for 2 periods one after the other and go back to baseline intensity. Baseline intensity is then

held for another 1 s. Stimuli were shown at 25 Hz and 40 Hz. Results are illustrated in Figure 3.23.

### **3.7.2 Materials and Methods**

RD10 mouse retina was interfaced with the CMOS-chip as described in Section 2.1.2. The stimulation electrodes of the CMOS-MEA were separated into three different areas which were connected a separate STG each. Two of those areas formed the letters E and I while the third area covered all other electrodes. The stimulation protocol consisted of the following four distinct phases:

1. In the first phase all stimulation electrodes were kept on 500 mV sinus with frequencies of 25 Hz and 40 Hz. This phase lasts 25 periods which corresponds to 625 ms or 1 s depending on the applied frequency. This phase is marked as t1 in the diagram.
2. The stimulation voltage applied to electrodes forming letter I was then increased to 2500 mV for 2 periods and decreased to baseline afterward. This phase is called t2 in the diagram.
3. In the third phase the stimulation voltage applied to electrodes forming letter E was increased to 2500 mV for 2 periods and then put back to baseline level. Again all other electrodes were kept on baseline level. This phase is called t3 in the diagram.
4. The sequence was concluded by phase t4 in which all electrodes were kept at 500 mV. It lasted 25 periods.

This procedure was repeated 5 times to increase statistics during relatively short periods t2 and t3.

Recordings were then low-pass filtered using a 4th order Bessel low-pass-filter at 300 Hz to suppress influence of spikes on the stimulus artifact. All 5 recordings were then averaged and smoothed using a Sawitzky-Golay filter. Extracted artifacts were then subtracted from each recording. Finally all five recordings were appended and spike-sorted. Activity was then calculated for each phase separately.

### **3.7.3 Results**

Background stimulation applied during phase t1 was chosen to be below activity threshold and showed little effects on activity modulation. On stimulation onset we found all cells centered above the stimulation site to show an increased activity. Reliable excitation was constrained to stimulation sites only and off-site neurons showed little change in their activity pattern. Very few cells in the surround showed an increase in activity while

most showed a slight decrease in activity. There were no signs of axon-related activation of off-site neurons. After stimulus offset activity levels of on-site neurons went back to baseline activity. We did not observe any kind of delayed response causing temporal overlays of on-site activity modulation between stimulation areas and phases t2 and t3. We did also not observe any significant derivation from baseline activity levels between phases t1 and t4.

### **3.7.4 Chapter-discussion**

While this experiment was designed as a simple proof of concept it showed several interesting results. The first and probably most important one is the spatial precision of sinusoidal stimulation. Spatial precision was one of our biggest concerns when thinking of the applicability of sinusoidal stimulation in retinal implants. We initially expected activation on BPC level to induce larger horizontal interaction than direct activation of RGCs. However at the same time activation of pre-synaptic layers should resemble physiological PR related input more closely. We were therefore pleasantly surprised to see that spatial encoding of letters using sinusoidal stimulation selectively activated cells above stimulation sites. There were even hints that it decreased activity in surrounding areas slightly which could be indications of contrast enhancing perception of the shown image. However this experiment was only designed as proof of concept and does not provide the needed statistics to fully support such claims. Further experiments are required to allow a solid statistical and quantitative analysis of described effects.

Despite these promising results there are still the common limitations to electrical stimulation of the retinal pathways. Electrically induced activity patterns on RGC level should resemble the projection of optically induced PR activation on RGC layer activity to be physiological. For letter shaped optical patterns resulting spatial patterns on the RGC layer not necessarily have to be letter-shaped. Additionally progressing rewiring-effects of diseases such as retinitis pigmentosa might change crosstalk-effects between cells and therefore make spatial resolution depending on the state of disease progression. In the end physiologists have to rely on the brains ability to relearn encoding of visual input.



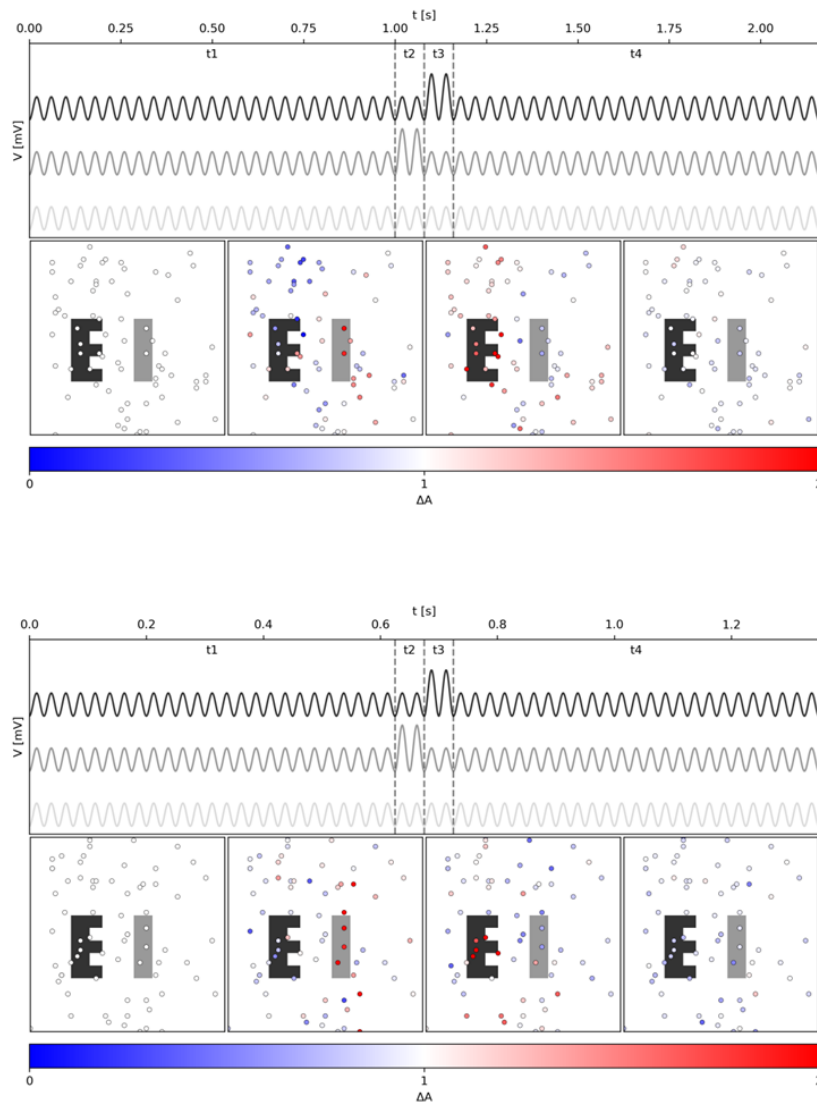


**Figure 3.23:** Effects of spatially-selective letter-shaped stimulation on RGC activity. Voltage-traces shown in top diagram correspond to voltage applied to stimulation-areas with the same color. A third unmodulated sinusoidal stimulus (lowest shown voltage trace) was applied to the background (white area). From left to right these correspond to time periods before, during stimulus one, during stimulus two and after stimulation. Activity of single cells normalized to the activity of the corresponding cell before stimulation (left panel) is shown in different colors. Red refers to an increase of activity and blue to a decrease in activity as illustrated by the color bar. Local increases in activity were clearly visible during stimulation. *Top:* 25 Hz stimulation. *Bottom:* 40 Hz stimulation.



# Chapter 4

## Conclusion

The results of all experiments were discussed in detail in the corresponding sections. Here we want to review all working blocks to form a single, coherent picture. We start by summarizing previously obtained results, and will continue by discussing system-related and stimulation-related outcomes. We will conclude this work by discussing further challenges encountered during the experimental series which do not directly fall into one of the previous blocks and give an outlook on potential developments in this field.

### 4.1 Summary of results

We investigated potentials of CMOS-MEA applications for simultaneous sinusoidal stimulation and recording of retinal ganglion cell activity using the CMOS-MEA 5000 system. We highlighted state of the art scientific applications, analyzed technical properties of the MEA such as light sensitivity and specific capacitance, and used the CMOS system to investigate effects of sinusoidal stimulation on retinal neurons.

An overview of current applications was shown and discussed in Section 3.1. The light sensitivity of the chips was analyzed in Section 3.2. We showed that artifacts introduced by optical stimulation could be removed using highpass and sliding average filters. Effects of optic stimulation could further be reduced using a thinner, native oxide-layer (See Section 3.3). We then performed additional experiments to determine system parameters such as specific capacitance and induced stimulation currents. We found that thinning of the oxide layer also increased the specific capacitance of the MEA by a factor of 3-4, which increases the accessible current-range for electrical stimulation.

We then evaluated stimulation thresholds of RD10 and C57BL/6J RGCs for sinusoidal stimulation at various frequencies. Stimulation effects on the cells were characterized using the three parameters activity (spike rate), reliability and vector-strength. We found stimulation thresholds for activity being smaller than those of pulsatile stimulation. Additionally thresholds for vector-strength were even smaller than those obtained for activity modulation.

In the following experiment application of electrical and optical stimulation as well as recording of neuronal activity during stimulation were combined. The experiment was designed to stimulate ON- and OFF-circuits within the retina separately using sinusoidal stimulation (see Section 3.5). However circuit-specific stimulation could not be realized using this approach. Potential explanations for this were discussed in detail in the section, but the most likely are: First, phase-splitting observed for ON- and OFF-cells is a result of photoreceptor-component of stimulation induced activity. Second, remodeling of the neuronal network in the retina after photoreceptor degeneration removes ON-/OFF-separation. Finally, a more robust cell-classification approach is required. Despite the negative result, optical stimulation, electrical stimulation and recording of neuronal activity were successfully applied without experiencing any saturation effects and collected data could be analyzed during all steps.

We continued by investigating effects of continuous sinusoidal stimulation over 10 min on RD10 cells. This was described in Section 3.6. Applied frequencies were 10 Hz, 25 Hz and 40 Hz at amplitudes of 2.0 V and 2.5 V. We divided recordings to one 3 s recordings every minute of stimulation with one recording before stimulation onset, one recording aligned with stimulation onset and one recording after stimulation offset. All other recordings were started relative to the first recording during stimulation with a pause of 57 s in between. Our first analysis focused on the recorded activity aligned with stimulation onset. One key result here was that cells responded with a constant increase in activity during the first 1 s to 1.5 s of stimulation for all frequencies and intensities. Adaptation effects could be observed after that initial period for activity and reliability. Both parameters did however not drop below baseline level during the complete stimulation cycle. In contrast vector strength did not show any adaptation effects, allowing temporally precise stimulation even after repetitive application.

Finally, we investigated spatial precision in Section 3.7 using a proof of concept approach for letter-shaped stimulation of retinal cells. This experiment was designed towards application in retinal implants. We presented sinusoidal stimuli in E and I shaped patterns which were applied in consecutive order while keeping a low-intensity background stimulation on over the whole chip. Induced retinal activity was mainly constrained on cells centered above stimulation electrodes. Cells off-site of the stimulation area showed little to no deviation from baseline activity level.

## **4.2 CMOS-MEA as a neurotechnological tool**

We found the CMOS-MEA 5000 system to be a tool which is suitable for a variety of applications. Its high spatial and temporal resolution make it ideal for monitoring of cell populations, as it enables observing of somatic activity but also cellular interaction at axonal levels in the form of spike triggered averages (STA). Additionally the system allowed recording of the propagation of local field potentials with high resolution. As

there's no switch matrix used in the CMOS-MEA 5000 system and all electrodes can be used for recording simultaneously. This is in contrast to some of the other systems on the market (Ballini et al. 2014; Heer, Hafizovic, Ugniwenko, et al. 2007). A drawback of small electrode-sizes were resulting large noise-values in the order of  $70 \mu\text{V}^*$ . Obtained signal-to-noise ratios (SNR) were still comparable to that of metal-electrode MEAs (Zeck, Jetter, et al. 2017). The high spatial resolution further enabled using multi-electrode thresholds for spiking detection (Lambacher et al. 2011). This led to detection of additional action potentials which would not have been detected using conventional (e.g.  $5\sigma$ ) thresholds.

Further characteristics of the system are its large number of stimulation electrodes, its three stimulus generators (STG) and the arbitrary spatial configurability of stimulation electrodes. An additional  $\text{TiO}_2$  layer on top of the electrodes results in purely capacitive coupling between bath and electrodes, thus preventing faradadic currents. This results in preserving of the CMOS-circuitry, increasing of the overall chip life-time, and prevents stimulus-induced damaging of neuronal tissue. The proximity of stimulation and recording electrodes led to strong cross-talks effects. A frequency-filter or averaging approach described in 2.3.1 worked sufficiently for our experiments to allow reliable data processing and spike-sorting. We found that artifacts for stimuli containing frequency components in the tens of Hz regime could be suppressed sufficiently while frequencies above 100 Hz left imprints on the recording which decreased spike-sorting quality tremendously.

This stimulation range might still be available for proper data analysis using more sophisticated filter approaches (Bertotti, Jetter, Dodel, et al. 2016).

Finally, we investigated the CMOS-MEA's sensitivity to light. A low light sensitivity of the chip would allow e.g. analyzing of physiological activity pattern to real-world stimuli, but also enables techniques such as two-photon or calcium imaging. The peak-sensitivity of the CMOS-MEA 5000-system is in the blueish regime close to 400 nm, which is a direct result electron-hole pair creation in the  $\text{TiO}_2$  layer 3.2. This peak-sensitivity correlates with the optical sensitivity of S-opsin in mouse retina. The impact on the recording is however not only determined by the stimulus wavelength but also by the intensity used. Artifacts introduced by stimulation in the photopic regime at wavelengths close to the peak-sensitivity of the oxide could be removed using previously described filter sets in our experiments (i.e. uniform filters and highpass-filters). The temporal shape of the stimulus consisted of a 1 Hz flicker stimuli with a 50% duty-cycle. Induces artifacts therefore contained mostly low-frequency components except for the edges at intensity transition. This made suppression of artifact components by frequency filtering simple as frequency components of spikes reside within hundreds to thousands of Hz. Optical stimuli containing high frequency components in contrast will result in an overlap of both frequency spectra of spikes and optically induced artifacts. This will make artifact suppression much more challenging for this kind of stimulus and it will need a different

---

\* C57BL/6J retina interfaced with CMOS-MEA,  $V_{\text{Source-Gate}} = -650 \text{ V}$ , frequency-band 300 Hz to 3000 Hz

approach to make information in the recorded data accessible.

While the peak-sensitivity of the  $\text{TiO}_2$  layer is within the blue regime the chip is still sensitive to light at higher wavelength though to a smaller degree. This influence is usually negligible for the red regime when it comes to optical stimulation or background illumination of the lab, but it becomes a limiting factor at higher intensities such as for 2-photon imaging. Finally optically induced drift on the recorded voltage puts an additional constrain on the recording duration. This constrain depends on the strength of the drift and as such on the intensity and wavelength of the stimulus. The drift results in a time dependance of the conversion factor from ADU to V due to the non-linearity of the conversion towards the edges of the ADC's input range and will eventually drive the sensor into saturation.

We conclude that the CMOS-MEA 5000 system is suitable tool for monitoring of cell-populations within an area of 1 mm. It provides high spatial and temporal resolution as well as a good signal to noise ratio. Its strengths for electrical stimulation are the 3 STGs, the high number of stimulation 1024 electrodes, and the flexibility of spatial configuration. Limitations for electrical stimulation are the accessible voltage windows of a maximum of 3.3 V minus the applied source-gate voltage and the unavoidable cross-talk between stimulation and recording electrodes. This system is therefore suitable for experiments where the flexible spatial arrangement of stimulation electrodes is used, up to three different stimuli are applied simultaneously and where the stimulation frequencies do not overlap too much with the frequency spectrum of spikes. Considering optical stimulation the user has to avoid high light intensities, blueish-light, high-frequency components in the stimulus shape and long recording durations. As such the systems applicability for optical stimulation heavily depends on the specific use-case.

### **4.3 Sinusoidal stimulation as a tool**

While investigating effects of sinusoidal stimulation we confirmed that sinusoidal stimulation modulate retinal ganglion cell (RGC) activity indirectly and does not induce activity in axons of passage (Weitz et al. 2015b). The first by blocking of presynaptic input to RGCs using DNQX and LAP4, the latter by locally confined activation of RGCs during the presentation of letter-shaped stimuli. We found activity-modulation thresholds for sinusoidal stimulation of RD10 RGCs to be smaller by a factor of 2-100 compared to thresholds for pulsed stimulation (Corna, Herrmann, and Zeck 2018). Adaptation effects of RGC populations to continuous sinusoidal stimulation were observed, but only after a stable response period of 1 s to 1.5 s. This energy-efficiency and reliability make sinusoidal stimulation a promising option for application in (retinal) electrical implants. A potential disadvantage could however be the unavoidable transformation of (optical) input into

sinusoidal stimulator output, as this adds a level of complexity to the underlying electrical device. Finally high vector strength timing modulation at sub-activity-modulation thresholds opens additional opportunities for future applications as discussed in Section 3.4. Synchronizing of spontaneous activity in blind retina could potentially be used to transmit information instead of inducing of additional spiking. This would then provide a low-energy, high signal-to-noise way of electrical stimulation (as the timing of action potentials is shifted to within a specific phase-interval of the stimulus, thus reducing out of phase activity and increasing in phase activity simultaneously). We are highly curious to see if this aspect of sinusoidal stimulation will be used in future medical applications.

## 4.4 Outlook

Here we want to discuss future work on our projects. When it comes to sinusoidal stimulation, we think a logical next step would be extending Stimulus Response Relations to a wider spectrum of frequencies and intensities while using a finer granularity for both parameters. For continuous stimulation next steps taken should go towards continuous recordings. This would avoid cell-identification across different recordings and would allow a more detailed long-term monitoring of cell activity modulation. Regarding letter-shaped stimuli we recommend to take a step backwards. Starting again using simpler pattern such as squares of different sizes would allow to obtain quantitative descriptions of effects and spatial distributions. This information would be useful for planning electrode-sizes for future MEAs or implants. However all these projects have in common that they would greatly benefit from a more specific classification of cells.

Novel classification algorithms could potentially be supported by future generations of MEAs. We think that improvements could include larger numbers of electrodes, larger recording areas, additional read-out channels and larger signal-to-noise ratios, e.g. by use of analog on-board low-pass filters in the case of the CMOS-MEA 5000 system. Additional information will come from 3D-MEAs which extend electrical imaging to the third dimension using needle-like electrodes. This would allow recording from BPCs and ACs for the retina and could lead to deeper understandings of cell-classes, networks thereof and corresponding signal-processing features.

Most of these improvements - both technological as well as proposed next steps for investigating sinusoidal stimulation - will come at the cost of increased data-rates. This is a transformation of which we think that it is highly critical and underrated. We therefore want to discuss future developments and possible solutions in the remaining part of this section. In the frame of this work we already collected data at rates of approximately  $200 \text{ MB s}^{-1}$ . It was this data-rate that restricted us to recordings in the order of few seconds as it put tough requirements on hardware and data-storage as well as increased durations of data pre-processing and spike-sorting. It also limited us in recording duration (and thus e.g. in the granularity used for SRRs), in the number of recording repetitions

(e.g. to achieve increased noise-suppression by averaging) and slowed down the overall progress as data-filtering and spike sorting consumed lots of computational resources which were shared by the whole group. Data-size was the largest obstacle encountered in this work. We think that this is a challenge faced not only by our group but which will or already does affect large parts of the neuro-scientific community regardless if data is collected using optical or electrical imaging techniques. We also think that in order to overcome this obstacle it is mandatory to professionalize solutions for data-storage, handling, and processing. While this problem has only become apparent to our group over the last few years as more and more students started using the CMOS-MEA 5000 system, large companies such as Google or Amazon or scientific institutions like the NASA have been dealing with similar problems for several years. Thus there's already a variety of relatively well-established tools and practices available. **Apache Hadoop** for example is an open-source software tool that allows distributed and redundant storing and processing of big data across a cluster of computers (Apache Software Foundation 2019). It was designed to be fault tolerant, i.e. resistant to single-hardware failures, and scalable. As Hadoop works with commodity hardware it could provide an affordable solution for scientific groups. **Apache Spark** is a cluster computing framework that can work on top of a Hadoop cluster. It is optimized to access and process data in the Hadoop File System and is provided with PySpark, a library for the Python scripting language which is very common in the scientific community. These tools are just examples for technologies which could provide affordable, save data storage and speed up data processing compared to conventional computer systems.

Naturally the solution has to be chosen with respect to the problem, i.e. the kind and format of data collected, the processing pipeline etc. The task of setting up an efficient IT infrastructure for data collection, cleaning and storing is called data-engineering. The data engineer is as such the link between the data-collecting system and the data-scientist. We think that data-engineering is a task of which most scientific groups are currently unaware or which is at least underrated. It is however a functional IT infrastructure that enables the data scientist to become fully efficient. We therefore think it is crucial to establish data engineering skills in scientific groups in order to fully take advantage of the ever increasing amount of information of novel recording systems, so that big data can become an enabler rather than a blocker. We are curious how this field will develop in the future and which open questions will be answered by this new kinds of technology.



# List of Figures

1.1	Structure of the retina . . . . .	3
1.2	The inner plexiform layer and bipolar cell stratification . . . . .	6
1.3	Retinal implant . . . . .	8
1.4	Equivalent circuitry and Hodgkin-Huxley predictions . . . . .	11
1.5	Experimental Setup . . . . .	13
2.1	Simplified illustration of the signal flow within the CMOS-MEA 5000 system.	17
2.2	The CMOS-MEA 5000 system . . . . .	18
2.3	CMOS chip layout . . . . .	20
2.4	CMOS-circuitry diagram . . . . .	21
2.5	Spectral distribution of the pE-4000 system . . . . .	24
2.6	Components of the pE-4000 system . . . . .	25
2.7	Schematics of $\mu$ -Matrix DMD . . . . .	26
2.8	Spike-sorting workflow . . . . .	32
2.9	Illustration of Vectorstrength . . . . .	34
3.1	Lowpass-filter . . . . .	38
3.2	Comparison of CMOS-MEA and metal-electrode MEA recordings . . . . .	39
3.3	Wavelengths dependency of leakage current . . . . .	43
3.4	Voltammogram with and without illumination . . . . .	44
3.5	Effects of optical stimulation on neural recording . . . . .	45
3.6	Effects of optical stimulation on CMOS-chips with and without oxide . . . . .	46
3.7	Sinusoidal currents . . . . .	49
3.8	Capacitance . . . . .	50
3.9	Specific capacitance values obtained for various frequencies . . . . .	50
3.10	Bath current as function of frequency . . . . .	51
3.11	Frequency dependance of stimulation currents for constant voltages . . . . .	52
3.12	Illustration of artifact removal . . . . .	55
3.13	SRR . . . . .	56
3.14	Sinusoidal stimulation thresholds: C57BL6/J . . . . .	61
3.15	Sinusoidal stimulation thresholds: RD10 . . . . .	62
3.16	Example of phase-locking . . . . .	68
3.17	Mean-phase values of ON- and OFF-RGCs for BL6 . . . . .	69
3.18	Circuit-specific stimulation: Results for RD1 . . . . .	69

3.19 Average normalized response during stimulation onset . . . . .	73
3.20 Fraction of responding cells for first 3 s . . . . .	74
3.21 Effects of continuous stimulation on vector-strength, activity and reliability	75
3.22 Cell response to pulsatile stimulation at various frequencies . . . . .	76
3.23 Letter-shaped stimuli . . . . .	81

# List of Tables

3.1	Stimulation thresholds: RD10 . . . . .	57
3.2	Stimulation thresholds: C57BL6/J . . . . .	58
3.3	Relative stimulation thresholds . . . . .	60
1	Specific capacitance values obtained for various frequencies with interfaced retina. . . . .	109
2	Number of cells used for obtaining thresholds: RD10 . . . . .	110
3	Number of cells used for obtaining thresholds: C57BL6/J . . . . .	111
4	Relative thresholds RD10 . . . . .	112
5	Relative thresholds C57BL/6J . . . . .	113



# Bibliography

- Apache Software Foundation (2019). *Apache Hadoop*. URL: <https://hadoop.apache.org/> (visited on 06/10/2019) (cit. on p. 88).
- Applebury, M.L et al. (2000). “The Murine Cone Photoreceptor: A Single Cone Type Expresses Both S and M Opsins with Retinal Spatial Patterning”. In: *Neuron* 27.3, pp. 513–523. ISSN: 0896-6273. DOI: [https://doi.org/10.1016/S0896-6273\(00\)00062-3](https://doi.org/10.1016/S0896-6273(00)00062-3) (cit. on p. 4).
- Baden, Tom et al. (2016). “The functional diversity of retinal ganglion cells in the mouse”. In: 529 (cit. on pp. 2, 6, 7, 41, 64, 65, 70).
- Ballini, M. et al. (2014). “A 1024-Channel CMOS Microelectrode Array With 26,400 Electrodes for Recording and Stimulation of Electrogenic Cells In Vitro”. In: *IEEE Journal of Solid-State Circuits* 49.11, pp. 2705–2719. DOI: 10.1109/JSSC.2014.2359219 (cit. on pp. 1, 85).
- Berens, Philipp (2009). “CircStat: A MATLAB Toolbox for Circular Statistics”. In: *Journal of Statistical Software, Articles* 31.10, pp. 1–21. ISSN: 1548-7660. DOI: 10.18637/jss.v031.i10 (cit. on p. 31).
- Bertotti, G., F. Jetter, N. Dodel, et al. (2016). “Artifact-compensated time-continuous recording from neural tissue during stimulation using a capacitively coupled in-vitro CMOS-MEA with 4k recording and 1k stimulation sites”. In: *2016 IEEE Biomedical Circuits and Systems Conference (BioCAS)*, pp. 256–259. DOI: 10.1109/BioCAS.2016.7833780 (cit. on pp. 27, 85).
- Bertotti, G., D. Velychko, N. Dodel, S. Keil, D. Wolansky, B. Tillak, M. Schreiter, A. Grall, P. Jesinger, S. Röhler, et al. (2014). “A CMOS-based sensor array for in-vitro neural tissue interfacing with 4225 recording sites and 1024 stimulation sites”. In: *2014*

*IEEE Biomedical Circuits and Systems Conference (BioCAS) Proceedings*, pp. 304–307. DOI: 10.1109/BioCAS.2014.6981723 (cit. on pp. 16, 21, 22).

Bertotti, Gabriel, Florian Jetter, Stefan Keil, et al. (2017). “Optical Stimulation Effects on TiO<sub>2</sub> Sensor Dielectric Used in Capacitively-Coupled High-Density CMOS Microelectrode Array”. In: PP (cit. on pp. vii, ix, 23, 42).

Bertotti, Gabriel, Dmytro Velychko, Norman Dodel, Stefan Keil, Dirk Wolansky, Bernd Tillak, Matthias Schreiter, Andreas Grall, Peter Jesinger, Sebastian Rohler, et al. (2014). “A CMOS-based sensor array for in-vitro neural tissue interfacing with 4225 recording sites and 1024 stimulation sites”. In: *2014 IEEE Biomedical Circuits and Systems Conference (BioCAS) Proceedings*. IEEE, pp. 304–307. ISBN: 978-1-4799-2346-5. DOI: 10.1109/BioCAS.2014.6981723 (cit. on p. 43).

Carcieri, Stephen M., Adam L. Jacobs, and Sheila Nirenberg (2003). “Classification of Retinal Ganglion Cells: A Statistical Approach”. In: *Journal of Neurophysiology* 90.3. PMID: 12966177, pp. 1704–1713. DOI: 10.1152/jn.00127.2003. eprint: <https://doi.org/10.1152/jn.00127.2003> (cit. on p. 64).

Chang, B. et al. (2002). “Retinal degeneration mutants in the mouse”. In: *Vision Research* 42.4, pp. 517–525. ISSN: 0042-6989. DOI: 10.1016/S0042-6989(01)00146-8 (cit. on p. 15).

*CMOS-MEA5000-System Manual* (2018) (cit. on p. 32).

Cohen, Ethan D. (2018). *Retinal Prostheses*. URL: <http://webvision.med.utah.edu/> (visited on 05/07/2018) (cit. on pp. 7, 9).

Corna, Andrea, Thoralf Herrmann, and Guenther Zeck (2018). “Electrode-size dependent thresholds in subretinal neuroprosthetic stimulation”. In: *Journal of Neural Engineering*. ISSN: 1741-2560. DOI: 10.1088/1741-2552/aac1c8 (cit. on pp. 53, 59, 61–63, 86).

D James, Conrad et al. (2004). “Extracellular Recordings From Patterned Neuronal Networks Using Planar Microelectrode Arrays”. In: *IEEE transactions on bio-medical engineering* 51, pp. 1640–8. DOI: 10.1109/TBME.2004.827252 (cit. on p. 41).

- D Lamb, Trevor, Shaun Collin, and Edward Pugh (2008). “Evolution of the vertebrate eye: Opsins, photoreceptors, retina and eye cup”. In: 8, pp. 960–76 (cit. on p. 3).
- Do, Michael Tri Hoang and King-Wai Yau (2010). “Intrinsically Photosensitive Retinal Ganglion Cells”. In: *Physiological Reviews* 90.4. PMID: 20959623, pp. 1547–1581. DOI: 10.1152/physrev.00013.2010. eprint: <https://doi.org/10.1152/physrev.00013.2010> (cit. on p. 6).
- Doroudchi, M Mehdi et al. (2011). “Virally delivered Channelrhodopsin-2 Safely and Effectively Restores Visual Function in Multiple Mouse Models of Blindness”. In: *Molecular Therapy* 19.7, pp. 1220–1229. ISSN: 15250016. DOI: 10.1038/mt.2011.69 (cit. on p. 7).
- Edwards, Thomas L. et al. (2018). “Assessment of the Electronic Retinal Implant Alpha AMS in Restoring Vision to Blind Patients with End-Stage Retinitis Pigmentosa”. In: *Ophthalmology* 125.3, pp. 432–443. ISSN: 01616420. DOI: 10.1016/j.optha.2017.09.019 (cit. on p. 9).
- Eickenscheidt, Max (2010). “Kapazitive Stimulation der Retina auf CMOS Chip”. PhD thesis. Technische Universität München (cit. on p. 13).
- Eickenscheidt, Max et al. (2012). “Electrical stimulation of retinal neurons in epiretinal and subretinal configuration using a multicapacitor array”. In: *Journal of Neurophysiology* 107.10, pp. 2742–2755. ISSN: 0022-3077. DOI: 10.1152/jn.00909.2011 (cit. on p. 52).
- Euler, Thomas et al. (2014). “Retinal bipolar cells: Elementary building blocks of vision”. In: *Nature Reviews Neuroscience* 15.8, pp. 507–519. ISSN: 14710048. DOI: 10.1038/nrn3783 (cit. on p. 6).
- Eversmann, Bjoern et al. (2004). “A 128 × 128 CMOS Biosensor Array for Extracellular Recording of Neural Activity”. In: *Solid-State Circuits, IEEE Journal of* 38, pp. 2306–2317. DOI: 10.1109/JSSC.2003.819174 (cit. on p. 1).
- Famm, Kristoffer et al. (2013). *Drug discovery: A jump-start for electroceuticals*. DOI: 10.1038/496159a. arXiv: NIHMS150003 (cit. on p. 1).

- Fenno, Lief, Ofer Yizhar, and K Deisseroth (2010). “The Development and Application of Optogenetics”. In: *Annual Review of Neuroscience*. ISSN: 0147-006X. DOI: 10.1146/annurev-neuro-061010-113817. arXiv: 0811.0559 (cit. on p. 41).
- Freeman, Daniel K. et al. (2010). “Selective Activation of Neuronal Targets With Sinusoidal Electric Stimulation”. In: *Journal of Neurophysiology* 104.5. PMID: 20810683, pp. 2778–2791. DOI: 10.1152/jn.00551.2010. eprint: <https://doi.org/10.1152/jn.00551.2010> (cit. on p. 7).
- Frey, U. et al. (2007). “Cell Recordings with a CMOS High-density Microelectrode Array”. In: *2007 29th Annual International Conference of the IEEE Engineering in Medicine and Biology Society*, pp. 167–170. DOI: 10.1109/IEMBS.2007.4352249 (cit. on p. 1).
- Fromherz, P. (2005). *Bioelectronics: From Theory to Applications*. Wiley, pp. 339–394 (cit. on p. 36).
- Fujikado, Takashi et al. (2016). “One-Year Outcome of 49-Channel Suprachoroidal Transretinal Stimulation Prosthesis in Patients With Advanced Retinitis Pigmentosa”. In: *Investigative Ophthalmology & Visual Science* 57.14, p. 6147. ISSN: 1552-5783. DOI: 10.1167/iovs.16-20367 (cit. on p. 9).
- Gargini, Claudia et al. (2007). “Retinal organization in the retinal degeneration 10 (rd10) mutant mouse: A morphological and ERG study”. In: *The Journal of Comparative Neurology* 500.2, pp. 222–238. ISSN: 00219967. DOI: 10.1002/cne.21144 (cit. on p. 15).
- Gollisch, Tim and Markus Meister (2010). “Eye Smarter than Scientists Believed: Neural Computations in Circuits of the Retina”. In: *Neuron* 65.2, pp. 150–164. ISSN: 08966273. DOI: 10.1016/j.neuron.2009.12.009. arXiv: NIHMS150003 (cit. on p. 6).
- Grant, F. A. (1959). “Properties of Rutile (Titanium Dioxide)”. In: *Reviews of Modern Physics* 31.3, pp. 646–674. ISSN: 0034-6861. DOI: 10.1103/RevModPhys.31.646 (cit. on p. 47).
- Heer, F., S. Hafizovic, W. Franks, et al. (2006). “CMOS microelectrode array for bidirectional interaction with neuronal networks”. In: *IEEE Journal of Solid-State Circuits* 41.7, pp. 1620–1629. DOI: 10.1109/JSSC.2006.873677 (cit. on p. 1).



- Heer, F., S. Hafizovic, T. Ugniwenko, et al. (2007). “Single-chip microelectronic system to interface with living cells”. In: *Biosensors and Bioelectronics* 22.11, pp. 2546–2553. ISSN: 0956-5663. DOI: <https://doi.org/10.1016/j.bios.2006.10.003> (cit. on p. 85).
- Herrmann, Rolf et al. (2011). “Rod Vision Is Controlled by Dopamine-Dependent Sensitization of Rod Bipolar Cells by GABA”. In: *Neuron* 72.1, pp. 101–110. ISSN: 0896-6273. DOI: 10.1016/J.NEURON.2011.07.030 (cit. on p. 5).
- Hodgkin, A. L. and A. F. Huxley (1952). “A quantitative description of membrane current and its application to conduction and excitation in nerve”. In: *The Journal of Physiology* 117.4, pp. 500–544. DOI: 10.1113/jphysiol.1952.sp004764. eprint: <https://physoc.onlinelibrary.wiley.com/doi/pdf/10.1113/jphysiol.1952.sp004764> (cit. on pp. 10, 11).
- Hyvarinen, A. (1999). “Fast and robust fixed-point algorithms for independent component analysis”. In: *IEEE Transactions on Neural Networks* 10.3, pp. 626–634. ISSN: 1045-9227. DOI: 10.1109/72.761722 (cit. on p. 30).
- Inayat, Samsoon et al. (2015). “Chemical stimulation of rat retinal neurons: feasibility of an epiretinal neurotransmitter-based prosthesis”. In: *Journal of Neural Engineering* 12.1, p. 016010. ISSN: 1741-2560. DOI: 10.1088/1741-2560/12/1/016010 (cit. on p. 7).
- Jae, Seol A et al. (2013). “Electrophysiological and Histologic Evaluation of the Time Course of Retinal Degeneration in the *rd10* Mouse Model of Retinitis Pigmentosa”. In: *The Korean Journal of Physiology & Pharmacology* 17.3, p. 229. ISSN: 1226-4512. DOI: 10.4196/kjpp.2013.17.3.229 (cit. on p. 15).
- Jensen, Ralph J. and Joseph F. Rizzo (2007). “Responses of ganglion cells to repetitive electrical stimulation of the retina”. In: *Journal of Neural Engineering* 4.1, S1–S6. ISSN: 17412560. DOI: 10.1088/1741-2560/4/1/S01 (cit. on pp. 70–72, 76, 78).
- Jeon, Chang-Jin, Enrica Strettoi, and Richard H. Masland (1998). “The major cell populations of the mouse retina. *J Neurosci.*” In: 18, pp. 8936–46 (cit. on p. 3).

- Jones, Bryan W. and Robert E. Marc (2005). “Retinal remodeling during retinal degeneration”. In: *Experimental Eye Research* 81.2, pp. 123–137. ISSN: 0014-4835. DOI: <https://doi.org/10.1016/j.exer.2005.03.006> (cit. on p. 70).
- Kawamura, Satoru (1995). “Phototransduction, excitation and adaptation”. In: *Neurobiology and Clinical Aspects of the Outer Retina*. Ed. by M. B. A. Djamgoz, S. N. Archer, and S. Vallergera. Dordrecht: Springer Netherlands, pp. 105–131. ISBN: 978-94-011-0533-0. DOI: 10.1007/978-94-011-0533-0\_5 (cit. on p. 4).
- Kolb, Helga et al. (2018). *Webvision: The Organization of the Retina and Visual System*. URL: <http://webvision.med.utah.edu/> (visited on 05/02/2018) (cit. on p. 3).
- Kriebel, Martin et al. (2011). “The cell adhesion molecule neurofascin stabilizes axo-axonic GABAergic terminals at the axon initial segment.” In: *The Journal of biological chemistry* 286 27, pp. 24385–93 (cit. on pp. 36, 37).
- Lambacher, A. et al. (2011). “Identifying firing mammalian neurons in networks with high-resolution multi-transistor array (MTA)”. In: *Applied Physics A* 102.1, pp. 1–11. ISSN: 0947-8396. DOI: 10.1007/s00339-010-6046-9 (cit. on pp. 29, 37, 40, 85).
- Leibig, Christian, Thomas Wachtler, and Guenther Zeck (2016). “Unsupervised neural spike sorting for high-density microelectrode arrays with convolutive independent component analysis”. In: *Journal of Neuroscience Methods* 271, pp. 1–13. ISSN: 0165-0270. DOI: <https://doi.org/10.1016/j.jneumeth.2016.06.006> (cit. on p. 29).
- Linsenmeier, Robert A. and Hao F. Zhang (2017). “Retinal oxygen: from animals to humans”. In: *Progress in Retinal and Eye Research* 58, pp. 115–151. ISSN: 13509462. DOI: 10.1016/j.preteyeres.2017.01.003 (cit. on p. 9).
- Lorach, Henri et al. (2015). “Photovoltaic restoration of sight with high visual acuity”. In: *Nature Medicine* 21.5, pp. 476–482. ISSN: 1078-8956. DOI: 10.1038/nm.3851 (cit. on p. 9).
- Luo, Yvonne H-L. et al. (2016). “Long-term Repeatability and Reproducibility of Phosphene Characteristics in Chronically Implanted Argus II Retinal Prosthesis Subjects”. In: *American Journal of Ophthalmology* 170, pp. 100–109. ISSN: 0002-9394. DOI: <https://doi.org/10.1016/j.ajo.2016.07.021> (cit. on p. 7).

- MacNeil, Margaret A. et al. (2004). “The population of bipolar cells in the rabbit retina”. In: *The Journal of Comparative Neurology* 472.1, pp. 73–86. ISSN: 0021-9967. DOI: 10.1002/cne.20063 (cit. on p. 7).
- Masland, Richard H. (2011). “Cell Populations of the Retina: The Proctor Lecture”. In: *Investigative Ophthalmology & Visual Science* 52.7, p. 4581. DOI: 10.1167/iovs.10-7083. eprint: /data/journals/iovs/933461/z7g00711004581.pdf (cit. on p. 3).
- (2012). “The tasks of amacrine cells”. In: *Visual Neuroscience* 29.01, pp. 3–9. ISSN: 0952-5238. DOI: 10.1017/S0952523811000344 (cit. on pp. 2, 7).
- Nanduri, D. et al. (2008). “Retinal prosthesis phosphene shape analysis”. In: *2008 30th Annual International Conference of the IEEE Engineering in Medicine and Biology Society*, pp. 1785–1788. DOI: 10.1109/IEMBS.2008.4649524 (cit. on p. 7).
- Obien, Marie Engelen J. et al. (2015). “Revealing neuronal function through microelectrode array recordings”. In: *Frontiers in Neuroscience* 9.JAN, p. 423. ISSN: 1662453X. DOI: 10.3389/fnins.2014.00423 (cit. on p. 38).
- Röhlich, P., Th. van Veen, and A. Szel (1994). “Two different visual pigments in one retinal cone cell”. In: *Neuron* 13.5, pp. 1159–1166. ISSN: 0896-6273. DOI: [https://doi.org/10.1016/0896-6273\(94\)90053-1](https://doi.org/10.1016/0896-6273(94)90053-1) (cit. on p. 4).
- Safadi, M. et al. (2003). “Development of a Microfluidic Drug Delivery Neural Stimulating Device for Vision”. In: *iovs Investigative ophthalmology & visual science* 44.13 (cit. on p. 7).
- Shekhar, Karthik et al. (2017). “Neurons by single-cell transcriptomics”. In: 166.5, pp. 1308–1323. DOI: 10.1016/j.cell.2016.07.054.COMPREHENSIVE (cit. on pp. 2, 6).
- Stett, A et al. (2000). “Electrical multisite stimulation of the isolated chicken retina”. In: *Vision Research* 40.13, pp. 1785–1795 (cit. on p. 59).
- Stingl, Katarina et al. (2013). “Artificial vision with wirelessly powered subretinal electronic implant alpha-IMS”. In: *Proceedings of the Royal Society B: Biological Sciences* 280.1757, p. 20130077. ISSN: 0962-8452. DOI: 10.1098/rspb.2013.0077 (cit. on p. 9).

- Strauss, Olaf (2011). *The Retinal Pigment Epithelium*. URL: <http://webvision.med.utah.edu/> (visited on 01/26/2011) (cit. on p. 4).
- Stutzki, Henrike et al. (2014). “Inflammatory stimulation preserves physiological properties of retinal ganglion cells after optic nerve injury”. In: *Frontiers in Cellular Neuroscience* 8. ISSN: 1662-5102. DOI: 10.3389/fncel.2014.00038 (cit. on p. 37).
- Tikidji-Hamburyan, Alexandra et al. (2015). “Retinal output changes qualitatively with every change in ambient illuminance”. In: *Nature Neuroscience* 18.1, pp. 66–74. ISSN: 1097-6256. DOI: 10.1038/nn.3891 (cit. on p. 67).
- Twyford, Perry, Changsi Cai, and Shelley Fried (2014). “Differential responses to high-frequency electrical stimulation in ON and OFF retinal ganglion cells”. In: *Journal of Neural Engineering* 11.2, p. 025001. DOI: 10.1088/1741-2560/11/2/025001 (cit. on p. 67).
- Twyford, Perry and Shelley Fried (2016). “The Retinal Response to Sinusoidal Electrical Stimulation”. In: *IEEE Transactions on Neural Systems and Rehabilitation Engineering* 24.4, pp. 413–423. ISSN: 1534-4320. DOI: 10.1109/TNSRE.2015.2415811 (cit. on p. 67).
- Voelker, Moritz and Peter Fromherz (2006). “Nyquist noise of cell adhesion detected in a neuron-silicon transistor”. In: *Physical Review Letters* 96.22, pp. 1–4. ISSN: 00319007. DOI: 10.1103/PhysRevLett.96.228102 (cit. on p. 41).
- Wallrapp, Frank and Peter Fromherz (2006). “TiO<sub>2</sub> and HfO<sub>2</sub> in electrolyte-oxide-silicon configuration for applications in bioelectronics”. In: *Journal of Applied Physics* 99.11, pp. 1–10. ISSN: 00218979. DOI: 10.1063/1.2199707 (cit. on pp. 49, 51, 52).
- Weitz, Andrew C. et al. (2015a). “Improving the spatial resolution of epiretinal implants by increasing stimulus pulse duration”. In: *Science Translational Medicine* 7.318, 318ra203–318ra203. ISSN: 1946-6234. DOI: 10.1126/scitranslmed.aac4877. eprint: <https://stm.sciencemag.org/content/7/318/318ra203.full.pdf> (cit. on p. 63).
- Weitz, Andrew C et al. (2015b). “Improving the spatial resolution of epiretinal implants by increasing stimulus pulse duration.” In: *Science translational medicine* 7.318, 318ra203. ISSN: 1946-6242. DOI: 10.1126/scitranslmed.aac4877 (cit. on p. 86).

- Wilke, Robert et al. (2011). “Spatial Resolution and Perception of Patterns Mediated by a Subretinal 16-Electrode Array in Patients Blinded by Hereditary Retinal Dystrophies”. In: *Investigative Ophthalmology & Visual Science* 52.8, p. 5995. ISSN: 1552-5783. DOI: 10.1167/iovs.10-6946 (cit. on p. 9).
- Wuchter, Jennifer et al. (2012). “A Comprehensive Small Interfering RNA Screen Identifies Signaling Pathways Required for Gephyrin Clustering”. In: *Journal of Neuroscience* 32.42, pp. 14821–14834. ISSN: 0270-6474. DOI: 10.1523/JNEUROSCI.1261-12.2012. eprint: <http://www.jneurosci.org/content/32/42/14821.full.pdf> (cit. on p. 36).
- Yan, Boyuan and Sheila Nirenberg (2018). “An Embedded Real-Time Processing Platform for Optogenetic Neuroprosthetic Applications”. In: *IEEE Transactions on Neural Systems and Rehabilitation Engineering* 26.1, pp. 233–243. ISSN: 1534-4320. DOI: 10.1109/TNSRE.2017.2763130 (cit. on p. 7).
- Zeck, Günther M. and Richard H. Masland (2007). “Spike train signatures of retinal ganglion cell types”. In: *European Journal of Neuroscience* 26.2, pp. 367–380. DOI: 10.1111/j.1460-9568.2007.05670.x. eprint: <https://onlinelibrary.wiley.com/doi/pdf/10.1111/j.1460-9568.2007.05670.x> (cit. on p. 64).
- Zeck, Günther, Florian Jetter, et al. (2017). “Electrical Imaging: Investigating Cellular Function at High Resolution”. In: 1, p. 1700107 (cit. on pp. vii, ix, 11, 36, 85).
- Zrenner, Eberhart (2013). “Fighting blindness with microelectronics.” In: *Science translational medicine* 5.210, 210ps16. ISSN: 1946-6242. DOI: 10.1126/scitranslmed.3007399 (cit. on p. 8).



# Statement of contributions

## Electrical Imaging: Investigating Cellular Function at High Resolution

Authors: Günter Zeck, Florian Jetter, Lakshmi Channappa, Gabriel Bertotti, and Roland Thewes

Published in: *Advanced Biosystems*, Volume: 1, Issue: 11, October 2017,  
doi: 10.1002/adbi.201700107

This publication reviews neuroscientific applications of CMOS-MEA systems including new experimental results and evaluations. The publication contains own data and was written by G.Z.. Own contributions include evaluations of signal-to-noise ratios obtained for retinal ganglion cells (RGC) spiking as well as recordings of propagation of local field potentials in epileptical hippocampus slices. Preparation of hippocampus slices and recording of activity thereof were performed by L.C..

My contributions to the review included preparation of mouse retina following the protocol introduced in Section 2.1.2 as well as recordings of RGC and neuronal activity using the CMOS-MEA 5000 system. I filtered and spike-sorted recorded data and performed statistical analysis of the extracted activity. The software used for filtering and evaluating of data was implemented by myself in Python. Finally, I created shown figures 2 a)-d).

## **Optical Stimulation Effects on $\text{TiO}_2$ Sensor Dielectric used in Capacitively-Coupled High-Density CMOS Microelectrode Array**

Authors: Gabriel Bertotti, Florian Jetter, Stefan Keil, Norman Dodel, Matthias Schreiter, Dirk Wolansky, Clemens Boucsein, Karl-Heinz Boven, Günther Zeck, and Roland Thewes

Published in: *IEEE Electron Device Letters*, Volume: 38, Issue: 7, July 2017, Pages: 967-970, doi: 10.1109/LED.2017.2701901

The framework of this project was a collaboration between the research group of Dr. Günther Zeck (G.Z., F.J.), Multichannel Systems (C.B., K.-H. B.) and the research group of Prof. Dr. Roland Thewes (R.T., G.B., S.K., N.D., M.S., D.W.). The study was initiated and designed by G.B. and R.T. and written mainly by G.B.. The goal of the study was to investigate effects and wavelength dependency of light on a high-density CMOS microelectrode array coated with a  $\text{TiO}_2$ -layer and find a physical explanation thereof. All parts of the project, dealing with recordings of electrophysiological signal from retinal tissue, were performed by me together with G.Z..

These own contributions included preparation of the retina, setting up of the stimulation and recording systems, as well as recording, filtering, spike-sorting and analyzing of data. For this purpose a pE-4000 light-source along with a  $\mu$ -Matrix DMD were setup. I synchronized the optical system with the CMOS system using TTL triggers and implemented optical stimuli using the  $\mu$ -Matrix control software. I performed separate recordings for stimuli at various wavelengths using this setup. Data was evaluated using Python scripts for filtering, analyzing and plotting which were developed by myself. Additional post-processing steps performed by myself included spike-sorting of filtered data. Finally, I developed algorithms for the identification of cells across multiple measurements.

### **CMOS-MEAs with native oxide**

Soldering work involved in creating of a bath electrode suitable for indirect measurement of the stimulation current as well as setting up of the corresponding recording system were performed by myself. Thoralf Hermann assisted with configuration of the voltage amplifier. I configured the CMOS-MEA system, connected the recording system for stimulation current measurements and ran the experiment. Finally, I also developed the stimulation protocols used in this experiment and all software components used for data filtering and evaluation.



## **Stimulus Response Relations to sinusoidal stimuli**

Trained personnel assisted by euthanizing the mice used in this experiment. Meng-Jung Lee and Larissa Höfling helped with preparation of mouse retina and this task was shared amongst the three of us. Creating of experimental design and interpretation of results occurred in alignment with Günther Zeck. The CMOS-MEA system was setup and recordings were performed by myself. I also developed the software for filtering, transformation, evaluation, and illustration of data and executed the corresponding tasks.

## **Circuit-specific stimulation**

Trained personnel assisted by euthanizing the mice used in this experiment. I received additional help in the frame of this work from Henrike Stutzki who assisted during mouse retina preparation. Experimental layout was created in close collaboration with Günther Zeck. All other parts of this project were performed by myself. These tasks were:

- setting up of the CMOS-MEA 5000 system for electrical stimulation and recording as well as setting up and configuration of the CoolLed system for optical stimulation
- defining of stimulation protocols
- performing of experiments, i.e. applying of electrical and optical stimulation and recordings neuronal activity
- filtering, analyzing and interpreting of data
- developing of software components for filtering, analyzing and illustration of data

## **Effects of continuous sinusoidal stimulation**

This experiment was designed in discussion with Günther Zeck. Mice sacrificed in the frame of this work were euthanized by trained personnel. Preparation of mouse retina was performed as a joint task amongst Meng-Jung Lee, Larissa Höfling, and me. All other work presented in this section was performed by myself. This included the experimental setup, i.e. configuration of hardware, preparing and mounting of mouse retina, design of stimulation profiles as well as applying of electrical stimuli and recording of cellular activity. Furthermore included were transformation, filtering, evaluation and interpretation of recorded data as well as development of all required software components. This includes design of all filtering steps and creating of figures.

## **Encoding of letter-shaped objects**

Design and parameters for this experimental series were developed in regular exchange with Günther Zeck. Mice were euthanized by trained personnel. All mouse retina used during this experiment was prepared either by Meng-Jung Lee, Larissa Höfling or myself. I set up and configured the CMOS-MEA system used for stimulation and recording of neuronal activity and ran the experiment. All stimulation patterns used were created by myself. Data was filtered and analyzed, and results were illustrated by me using software components developed on my own.

# Acknowledgements

Während meiner Jahre am NMI durfte ich viele Menschen treffen, die dazu beigetragen haben, diese Zeit für mich zu einer großen Bereicherung zu machen. All diese Menschen hätten einen persönlichen Dank verdient, nur ist der Platz dieser Seite leider begrenzt. Daher möchte ich mich hiermit von ganzem Herzen bei all jenen Ungenannten bedanken! Einige spezielle Menschen möchte ich nun im Folgenden aber dennoch besonders hervorheben:

Zuerst möchte ich mich ganz herzlich bei **Dr. Günther Zeck** für die Vergabe der Doktorarbeit und für die hervorragende Betreuung bedanken, und darüber hinaus bei der gesamten Forschungsgruppe Neurophysik, bei allen aktuellen & ehemaligen Mitgliedern, für die tolle Arbeitsatmosphäre und gute Laune im Team. Ich habe mich bei euch sehr wohlgefühlt.

Ich danke **Prof. Dr. Cornelius Schwarz** und **Prof. Dr. Boris Hofmann** für Ihre Unterstützung im Advisory Board, für das hilfreiche Feedback und die fruchtbaren Diskussionen sowie dem Team des GTC, für die kompetent und überaus sympathische Betreuung.

Mein sportlicher Dank geht an **Larissa Höfling**, **Thoralf Herrmann** und **Maximilian Becker** für spannende Begegnungen am Tischkicker sowie an **Pauline Jeckel**, **Werner Dreher** und **die gesamte Lauftruppe** für die unzähligen tollen, gemeinsam gelaufenen Kilometer.

**Dr. Richard Griesbach** danke ich für all die tollen Unterhaltungen über Astronomie und das Windelnwechseln bis hin zu CRISPR-CAS9. Ich habe jede davon sehr genossen!

**Meinen Eltern und meinem Bruder Philipp.** Trotz aller Schwierigkeiten konnte ich in jeglicher Hinsicht auf euren Rückhalt zählen und auch das Studium stand nie zur Diskussion. Mir wird zunehmend bewusst, dass dieser Zusammenhalt alles andere als selbstverständlich ist. Danke!

Und schließlich geht mein tiefster Dank an meine drei, **Nadine, Emil und Anton.** Ich weiß nicht, wo ich bei all dem Erwähnenswerten anfangen und wie ich es darüber

hinaus in einen einzelnen Satz verpacken sollte. Daher sage ich einfach "Danke! Es ist schön, euch bei mir zu haben!"

# Appendix

Frequency [Hz]	10	25	40	100
$c_s$ [ $\mu\text{F cm}^{-2}$ ]	6.11	5.92	5.82	5.03

**Table 1:** Specific capacitance values obtained for various frequencies for recordings during stimulation using a CMOS-MEA with native oxide and interfaced RD10 mouse retina. Values were obtained as inclination from  $I(V)$  divided by the total stimulation area used.

	electrodes	area [mm <sup>2</sup> ]	N <sub>x0</sub>	N <sub>x30</sub>	N <sub>x50</sub>	N <sub>vs</sub>
10 Hz	2x2	0.003	8	37	18	11
	4x4	0.010	6	19	13	26
	5x5	0.016	5	15	8	15
	6x6	0.023	26	56	31	52
	8x8	0.040	15	46	35	39
	10x10	0.063	41	64	53	63
	32x32	0.648	68	99	78	88
25 Hz	2x2	0.003	2	13	6	16
	4x4	0.010	15	33	20	51
	5x5	0.016	9	19	13	23
	6x6	0.023	31	47	40	87
	8x8	0.040	24	50	37	60
	10x10	0.063	35	57	44	69
	32x32	0.648	121	133	115	135
40 Hz	2x2	0.003	1	41	30	17
	4x4	0.010	37	50	36	82
	5x5	0.016	13	23	17	21
	6x6	0.023	44	76	49	88
	8x8	0.040	36	53	41	65
	10x10	0.063	64	74	58	86
	32x32	0.648	88	99	96	104

**Table 2:** This table lists the number of RGCs used for obtaining stimulation thresholds for RD10-type mice in Table 3.1.

	electrodes	area [mm <sup>2</sup> ]	N <sub>x0</sub>	N <sub>x30</sub>	N <sub>x50</sub>	N <sub>vs</sub>
10 Hz	2x2	0.003	1	11	5	18
	3x3	0.006	6	7	2	12
	4x4	0.010	25	31	22	43
	5x5	0.016	15	16	14	27
	6x6	0.023	35	38	28	62
	8x8	0.040	25	27	23	32
	10x10	0.063	74	82	69	108
	32x32	0.648	77	81	72	79
25 Hz	2x2	0.003	4	3	2	22
	3x3	0.006	13	14	4	34
	4x4	0.010	19	30	27	52
	5x5	0.016	23	27	20	32
	6x6	0.023	44	50	42	69
	8x8	0.040	33	34	28	39
	10x10	0.063	76	80	70	86
	32x32	0.648	43	63	61	49
40 Hz	2x2	0.003	9	12	9	27
	3x3	0.006	11	14	12	23
	4x4	0.010	32	42	30	57
	5x5	0.016	19	21	17	31
	6x6	0.023	48	53	45	53
	8x8	0.040	30	35	32	30
	10x10	0.063	26	32	30	26
	32x32	0.648	37	56	56	39

**Table 3:** This table lists the number of RGCs used for obtaining stimulation thresholds for C57BL6/J-type mice in Table Table 3.2

frequency	electrodes	area	$x_0$	$x_{30}$	$x_{50}$	$vs_{x_0}$
10 Hz	2x2	0.003	0.010	0.011	0.011	0.010
	4x4	0.010	0.030	0.022	0.024	0.035
	5x5	0.016	0.066	0.043	0.046	0.063
	6x6	0.023	0.183	0.170	0.174	0.152
	8x8	0.040	0.219	0.097	0.092	0.166
	10x10	0.063	0.305	0.171	0.188	0.194
	32x32	0.648	0.491	0.408	0.435	0.238
25 Hz	2x2	0.003	0.021	0.016	0.016	0.018
	4x4	0.010	0.030	0.022	0.021	0.020
	5x5	0.016	0.065	0.045	0.060	0.045
	6x6	0.023	0.171	0.109	0.162	0.105
	8x8	0.040	0.180	0.151	0.155	0.103
	10x10	0.063	0.242	0.170	0.199	0.125
	32x32	0.648	0.421	0.243	0.254	0.159
40 Hz	2x2	0.003	0.027	0.008	0.006	0.013
	4x4	0.010	0.027	0.019	0.019	0.023
	5x5	0.016	0.070	0.045	0.043	0.043
	6x6	0.023	0.157	0.115	0.131	0.093
	8x8	0.040	0.144	0.086	0.099	0.091
	10x10	0.063	0.229	0.155	0.140	0.082
	32x32	0.648	0.444	0.142	0.184	0.123

**Table 4:** Stimulation thresholds obtained for RD10 RGCs for sinusoidal stimuli relative to results obtained for RD10 RGCs during pulsatile stimulation.



frequency	electrodes	area	$x_0$	$x_{30}$	$x_{50}$	$VS_{x_0}$
10 Hz	2x2	0.003	0.005	0.017	0.012	0.017
	3x3	0.006	0.021	0.020	0.029	0.022
	4x4	0.010	0.032	0.029	0.035	0.022
	5x5	0.016	0.061	0.036	0.045	0.040
	6x6	0.023	0.183	0.114	0.108	0.120
	8x8	0.040	0.179	0.096	0.106	0.074
	10x10	0.063	0.210	0.132	0.139	0.105
	32x32	0.648	0.313	0.143	0.166	0.106
25 Hz	2x2	0.003	0.019	0.011	0.013	0.016
	3x3	0.006	0.025	0.026	0.020	0.016
	4x4	0.010	0.027	0.018	0.026	0.017
	5x5	0.016	0.045	0.047	0.055	0.026
	6x6	0.023	0.146	0.097	0.110	0.061
	8x8	0.040	0.157	0.107	0.090	0.071
	10x10	0.063	0.190	0.124	0.139	0.074
	32x32	0.648	0.289	0.102	0.105	0.107
40 Hz	2x2	0.003	0.020	0.014	0.014	0.014
	3x3	0.006	0.019	0.013	0.018	0.012
	4x4	0.010	0.028	0.022	0.021	0.013
	5x5	0.016	0.045	0.040	0.053	0.024
	6x6	0.023	0.129	0.093	0.097	0.066
	8x8	0.040	0.153	0.070	0.081	0.047
	10x10	0.063	0.191	0.068	0.075	0.059
	32x32	0.648	0.249	0.057	0.089	0.079

**Table 5:** Stimulation thresholds obtained for C57BL/6J RGCs for sinusoidal stimuli relative to results obtained for RD10 RGCs during pulsatile stimulation.

REVIEW

Electrical Imaging

ADVANCED  
BIOSYSTEMS  
www.adv-biosys.com

## Electrical Imaging: Investigating Cellular Function at High Resolution

Günther Zeck,\* Florian Jetter, Lakshmi Channappa, Gabriel Bertotti, and Roland Thewes

Electrical imaging of extracellular potentials reveals the activity of electrogenic cells and of networks thereof over several orders of magnitude, both in space and time. On a spatial scale, electrical activity propagates in nanometer-sized nerve fibers (axons, dendrites), which connect cells in a biological network over several millimeters. On a temporal scale, changes of the extracellular potential caused by action potentials occur on a sub-millisecond scale, while network activity may be modulated over seconds. Here, different electrode arrays are described, which are designed to image modulations of the electrical potentials over a wide spatiotemporal range. In the second part, typical applications and scientific questions in neuroscience research addressed so far are reviewed. The review ends with an outlook on expected developments.

### 1. Biotechnological Constrains of “Electrical Imaging”

Electrical imaging refers to the recording of electrical signals at a spatial resolution matching the size of individual electrogenic cells and at a temporal resolution matching the frequency response of these cells.<sup>[1–3]</sup> From a physical perspective electrical imaging comprises the recording and visualization of extracellular potential changes caused by the activity of electrogenic cells (or compartments thereof) using appropriate electrode arrays. The visualization of the recorded voltage changes is achieved using false color coding of the recorded signal.<sup>[4]</sup>

“Electrogenic cell” is a collective term for different cell types, which produce transmembrane ionic currents upon changing their cell membrane potential. Well studied electrogenic cells are the many neuronal cell types<sup>[5]</sup> or heart muscle cells.<sup>[6]</sup> More

recently membrane currents from skeletal myotubes,<sup>[7]</sup> from glia or from glia-derived cancerogenic glioma cells<sup>[8]</sup> or from pancreatic beta cells<sup>[9]</sup> have been reported. In brain or muscle tissues different cell types interact. As a consequence the generated electrical signals comprise a rich frequency content ranging from few Hertz to several kilohertz.<sup>[10]</sup> Electrical signaling on sub-millisecond time scale occurs during so-called action potentials, when the transmembrane potential changes rapidly due to the opening and closing of voltage-gated sodium channels.

In this review we will discuss biotechnological aspects relevant for the “electrical imaging” technique and highlight applications in neuroscience. Related recent reviews discussed some of the technological backgrounds of microelectrode arrays<sup>[11]</sup> and some of their applications.<sup>[6]</sup>


To estimate the requirements needed to image the electrical activity in neurons and networks, we summarize important scales and numbers. A typical neuron comprises a cell body, which integrates the presynaptic signals using an elaborate dendritic network (dendritic tree) and sends an action potential (stereotyped transmembrane voltage signal) activity to synaptically connected neurons using a thin axonal cable-like fiber. Mammalian cell bodies are typically about 10–20  $\mu\text{m}$  in diameter, while the cable-like dendritic and axonal structures have diameters ranging between a few tens of nanometers up to several micrometers.<sup>[12]</sup> The entire dendritic tree of one neuron or of a synaptically connected neuronal network may cover an area ranging between few tens of micrometers up to tens of square millimeter.<sup>[12]</sup> Within the retinal ganglion cell layer or hippocampal cell layers the neuronal density may be as high as 5000–10 000 cells  $\text{mm}^{-2}$  (mouse retinal ganglion cells,<sup>[13]</sup> granule cells)<sup>[14]</sup> to name just two prominent neural tissues studied so far using electrical imaging. These numbers highlight the spatial range and resolution to be achieved for imaging the electrical activity generated and propagating therein at (sub) cellular resolution.

Optical imaging—the most common imaging modality in life sciences—achieves high-resolution digital imaging by magnifying and recording the light signal using a complementary metal-oxide semiconductor (CMOS) camera chip. Relevant parameters for optical imaging comprise (i) a large field of view, (ii) a high signal-to-noise ratio (SNR), and (iii) high spatial and (iv) high temporal resolution. The ratio between the sensitivity of the CMOS sensors (i.e., minimal number of detected photons) and the corresponding pixel noise sets the sensitivity limit.

Electrical imaging—potentially a complementary or alternative technique of optical imaging—deals with the same constrains. Here, instead of a light-detecting CMOS camera chip, the changing

Dr. G. Zeck, F. Jetter, Dr. L. Channappa  
Neurophysics, Natural and Medical Sciences Institute  
at the University Tübingen  
72770 Reutlingen, Germany  
E-mail: guenther.zeck@nmi.de

G. Bertotti, Prof. R. Thewes  
Chair of Sensor and Actuator Systems  
Technical University of Berlin  
10587 Berlin, Germany

 The ORCID identification number(s) for the author(s) of this article can be found under <https://doi.org/10.1002/adbi.201700107>.

© 2017 The Authors. Published by WILEY-VCH Verlag GmbH & Co. KGaA, Weinheim. This is an open access article under the terms of the Creative Commons Attribution-NonCommercial-NoDerivs License, which permits use and distribution in any medium, provided the original work is properly cited, the use is non-commercial and no modifications or adaptations are made.

The copyright line for this article was changed on 21 December 2017 after original online publication

DOI: 10.1002/adbi.201700107

Adv. Biosys. 2017, 1, 1700107

1700107 (1 of 8)


© 2017 The Authors. Published by WILEY-VCH Verlag GmbH & Co. KGaA, Weinheim

extracellular potential above recording electrodes is amplified using dedicated CMOS-based microelectrode arrays (MEAs).

State-of-the art microelectrode arrays integrate several thousand sensors within the recording area, which typically ranges from one to few square millimeters.<sup>[15–19]</sup> Cell size (10–20  $\mu\text{m}$ ) and cell density (5000–10 000 cells  $\text{mm}^{-2}$ ) dictate the high spatial resolution of about 10  $\mu\text{m}$ . This high spatial resolution is achieved by a small electrode separation/pitch and on-chip multiplexing electronics which reduces the number of interconnects between electrodes and amplification stages. Two different types of CMOS-based microelectrode arrays (MEAs) are schematically shown in Figure 1.

In the first approach (Figure 1A) all recording electrodes are covered by a thin dielectric. The extracellular voltage change caused by the active electrogenic cell is amplified using an underlying sensing field effect transistor.<sup>[15,16]</sup> In the second approach (Figure 1B) openings for the metal electrodes are processed in an oxide passivation layer. To ensure long-term stability the electrodes are separated from the CMOS contacts using dedicated metal-interconnects.<sup>[17,20,21]</sup> These two CMOS MEA types also represent the two major recording modes currently used: full-imaging CMOS MEAs, where the number of available electrodes largely corresponds to the number of simultaneous readout channels<sup>[15,16,18,22]</sup> and CMOS MEAs where the all electrodes are recorded in a sequential way using the so-called switch-matrix approach.<sup>[17,20]</sup> A comprehensive list of state-of-the art CMOS-based MEAs is given in Table 1.

Two technological constrains of electrical imaging were discussed in greater detail over the last decade and will be reviewed in the following: (i) the SNR and (ii) the frequency range of the recording. The improvement of SNR is typically tackled by reducing the electrode noise. A common argument claims that low-impedance electrodes are required for



**Günther Zeck** was born in Garbova/Urwegen, Romania, in 1973. He studied physics and received a Ph.D. degree in biophysics from the Technical University München, Germany. As a postdoctoral fellow at the Massachusetts General Hospital, Boston, USA, he started investigating healthy and blind retinas. Since 2010, he is head of the Research Group Neurophysics at the Natural and Medical Sciences Institute at the University Tübingen, Germany. His main interest is the development and application of electrodes, tools, and protocols for neuroscience and neurotechnology.

high-quality recording.<sup>[11,23]</sup> For a planar, substrate-integrated metal-based electrode the impedance is inverse proportional to the electrode capacitance.<sup>[24]</sup> For MEAs the interconnect from the sensing electrode to the first amplification stage is insulated by a thin oxide layer, which represents a stray capacitance. The stray capacitance and the electrode capacitance sum up to the final capacitance “seen” by the first amplification stage. To avoid recording of parasitic signals the electrode capacitance needs to be much larger than the stray capacitance. Typical electrode materials such as fractal-like titanium nitride (TiN) or carbon-nanotube electrodes have specific capacitances of 2.5–10  $\text{mF cm}^{-2}$ ,<sup>[25]</sup> which translates to 2–10 nF for an electrode diameter of 10  $\mu\text{m}$ . This value is about two to

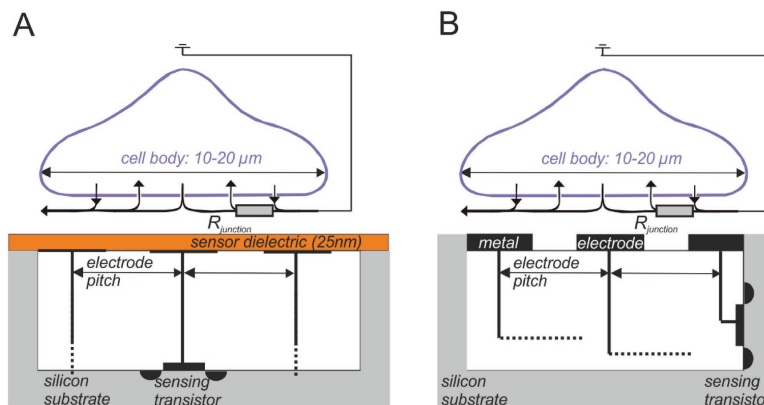


**Figure 1.** Schematic cross-sections of two different types of CMOS MEA used for electrical imaging. The electrodes record voltage changes caused by the current flow (indicated by arrows) in the resistive junction between cell membrane and electrode surface. A) Sensing electrodes are capacitively coupled to sensing transistors (field effect transistors) embedded in a CMOS chip. The entire chip surface is covered by a thin dielectric. CMOS MEA principle corresponds to refs. [15] and [16]. B) Metal electrodes are in direct contact to the electrolyte and shifted away from the locations of the original CMOS contacts to ensure long-term stability. CMOS MEA principle corresponds to refs. [17] and [20], see also Table 1. The vertical connections between electrodes and sensing transistors enable electrode pitches of  $\approx 10 \mu\text{m}$ . In both schematics, the electronics for sensor selection and AD conversion are not shown. The junction resistance  $R_{\text{junction}}$  between cell membrane and dielectric determines the signal quality and contributes to the noise of the recorded signal.

**Table 1.** Review of recent CMOS-based MEAs including the reported noise levels and signal amplitudes.

Reference	[16]	[17]	[18]	[19]	[15]	[22]	[20]
Sensing type	eEOSFET	Metal electrode	Metal electrode	Metal electrode	eEOSFET	Metal electrode	Metal electrode
Readout mode	Col. Multiplex	Switch matrix	APS		Col. Multiplex	APS	Switch matrix
Electrode pitch [ $\mu\text{m}$ ]	7.8	18	42	30	16	18.1	13.5
Number electrodes	16 384	11 011	4096	16 384	4225	8640	59 760
Simultaneous readout electrodes	16 384	126	4096	1	4225	9216	2048
Sampling rate [kHz]	2	20	8	22	77	6.5	20
Noise band width [kHz]	n/a	0.001–100	n/a	0.0004–5	0.01–77	0.01–3.3	0.3–10
Input noise [ $\mu\text{V}$ ]	<200	n/a	26	15	44	17	3.2
Signal amplitudes [ $\mu\text{V}$ ]	200–2000	50–100	100–600	50–200	200–2000	200–500	50–150

three orders of magnitude higher than that values for compact metal electrodes<sup>[23]</sup> or of insulated capacitive electrodes, where the sensing electrode is covered by a thin insulating dielectric (Figure 1A).<sup>[16,26]</sup> However, the high electrode capacitance in conjunction with the junction (spreading) resistance above the electrode may act as an “intrinsic” low-pass filter of the recorded signal. Thus, the low electrode noise obtained by low impedance electrode may be attributed to intrinsic filter properties, which, however, also reduce signal amplitude, as will be discussed below.

The electrode noise does not represent the only noise source in electrical imaging. The electronic amplifier represent a noise source, which however, in state-of-the art amplifiers is by about an order of magnitude smaller than the electrode noise.<sup>[11]</sup> Second, continuous operation of thousands of sensors (“full imaging”) requires a multiplexing readout scheme. Each sensor out is sampled at frequencies exceeding 1 MHz, which then leads to an increased high-frequency noise.<sup>[16]</sup> An additional noise source arises from the “spreading” resistance<sup>[27]</sup> caused by the interfaced resistive tissue or by the junction resistance of the resistive cleft between adhesion cell membrane and electrode surface.<sup>[28,29]</sup> The adhesion noise has been reported to increase the total noise by up to 50%<sup>[27]</sup> but can be actively used to image noninvasively cell or tissue adhesion.<sup>[27,29]</sup> The listed noise sources (amplifier, electrode, multiplexing, adhesion) have not quantified for different CMOS MEAs under similar experimental conditions. Specifically, the noise values summarized in Table 1 are reported for different frequency bands and without accounting for the adhesion noise.

In the following, we argue that absolute noise values are misleading when assessing recording quality. The improvement of the signal-to-noise ratio may also be tackled by increasing the signal amplitude. The recorded signal originates from the voltage drop above the recording electrode caused by that part of the transmembrane current which flows into the cleft between cell membrane and electrode surface. This voltage drop is large if the junction resistance  $R_{\text{junction}}$  between cell membrane and electrode is large, as theoretically formulated in the so-called point-contact model.<sup>[30]</sup> Values for the signal amplitude have been intensively debated for different electrode arrays and cell-electrode configurations.<sup>[31,32]</sup> Extracellular voltage amplitudes recorded underneath one single cultured rat neuron can reach several millivolts (ref. [33] and Figure 2A). For comparison we

illustrate a typical recording of cultured rat neurons using a metal-based electrode (see ref. [34] and Figure 2B) with signal amplitudes ranging between 80 and 100  $\mu\text{V}$ . Millivolt-sized amplitudes have been obtained using mushroom-shaped metal electrodes, which are engulfed by the interfaced neuron<sup>[35]</sup> or by electrodes which transiently electroporate the neuronal membrane.<sup>[36,37]</sup> Large axonal signal have been reported if the space between axonal membrane and recording electrode is confined using micrometer-sized tunnels,<sup>[38,39]</sup> thus probably reducing the extracellular space and thus increasing the seal resistance. For recording of action potentials generated by neurons embedded in brain tissue the point-contact model does not apply, given that now the cleft between cell membrane and electrode is in the same range or larger than the cell size. The signal amplitude recorded from pyramidal neurons in hippocampal slices ranges between 0.1 and 0.3 mV, both in vitro<sup>[40]</sup> and in vivo.<sup>[41]</sup>

The signal amplitude recorded from retinal ganglion cells, which are embedded in the high-resistive retinal tissue ( $\approx 1\text{--}3\text{ k}\Omega\text{ cm}$ )<sup>[27,44]</sup> reaches up to few millivolts<sup>[42,45]</sup> in recordings using capacitive CMOS MEAs. In Figure 2C the recording from a mouse retina ganglion cell is presented with signal amplitudes exceeding 1 mV.<sup>[46]</sup> Surprisingly, much smaller amplitudes have been reported when using metal-based electrodes.<sup>[47,48]</sup> To clarify this discrepancy we recorded from the same retina using a metal-based MEAs (comprising 252 TiN-based electrodes, electrode diameter 10  $\mu\text{m}$ , spatial separation: 60  $\mu\text{m}$ )<sup>[43]</sup> under otherwise identical recording conditions (Figure 2D). As noted above, the (large) capacitance of the recording electrode and interconnect together with the cleft resistance lead to an “electrode-intrinsic” filter with a time constant given by the product of capacitance and resistance<sup>[28]</sup> thus low-pass filtering the recorded voltage.

Assuming that the specific resistance corresponds to the specific resistivity of the recording medium (66  $\Omega\text{ cm}$ ) and a specific capacitance of 2 mF  $\text{cm}^{-2}$  the time constant of the metal electrode is  $\approx 0.06\text{ ms}$  only. The mammalian retina, however, has a high specific resistivity of 1.5  $\text{k}\Omega\text{ cm}$ <sup>[27,44]</sup> and consequently a time constant of about 1.3 ms. We apply a low-pass filter (cut-off frequency: 1 kHz) to the recording shown in Figure 2C,E. The low-pass filtered extracellular voltage recorded from a retinal ganglion cell using a capacitive electrode matches the signal recorded by a metal-based electrode (Figure 2E).

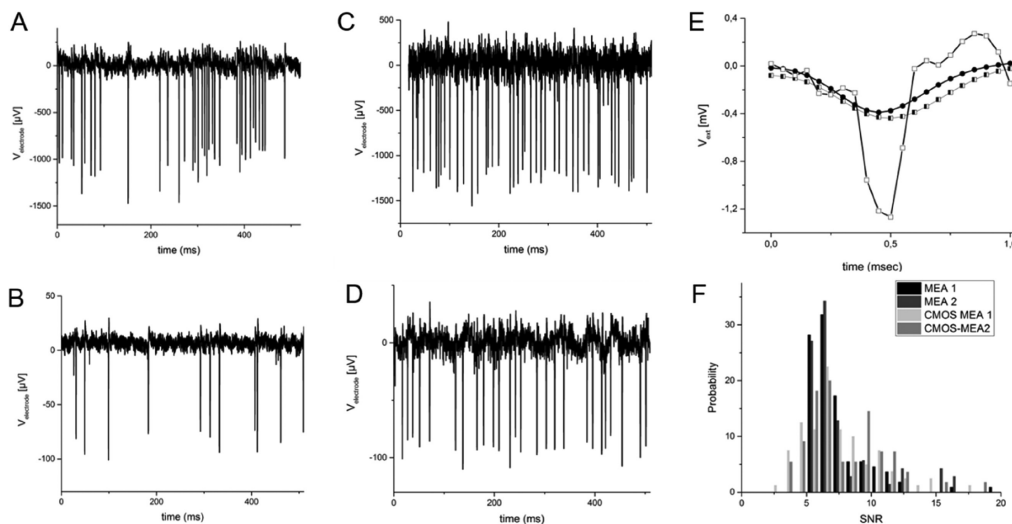


**Figure 2.** Extracellular recording from dissociated neuronal cultures and from ganglion cells in ex vivo retina. A) Signal trace recorded from a cultured neuron (10 d in vitro) by one electrode of a CMOS-based MEA. Signal amplitude is about 1 mV. B) Signal trace recorded from cultured neurons (10 d in culture) by one electrode of a passive MEA as described in.<sup>[34]</sup> Signal amplitude ranges between 80 and 100 μV. C) Signal trace of retinal ganglion cell activity recorded by one electrode of a CMOS-based MEA following the description provided in.<sup>[15]</sup> D) Signal trace recorded by a metal-based TiN electrode of a passive MEA, following the protocol described in ref. [43]. E) Single extracellular voltage trace recorded underneath one retinal ganglion cell using a capacitive CMOS MEA electrode (open square symbols) and a TiN electrode (filled square). The low-pass filtered voltage recorded by the capacitive CMOS MEA is shown using hashed symbols. F) Distribution of signal-to-noise ratios estimated for ganglion cell populations (≈100 cells per population) in four different recordings, two of them with passive metal-based electrode arrays and two of them using data recorded with capacitive CMOS-based MEAs. The median values obtained for the four SNR distributions in four ex vivo retinas are identical.

Finally, we calculated the SNR for populations of retinal ganglion cells using the two described types of MEA. The evaluation of the SNR may be biased when considering individual electrodes, which pick up signals from multiple cells. Therefore, we first performed a so-called spike sorting, i.e., the assignment of the detected signals to the generating cell.<sup>[49–51]</sup> The preprocessing steps for CMOS MEA and MEA recordings are the same, i.e., the raw data are band pass filtered (low pass 3 kHz, high pass 10 Hz). The spike sorting algorithms are different for CMOS MEA,<sup>[51]</sup> and MEA respectively.<sup>[52]</sup> The two different approaches lead to a small bias, because for the MEA data a fixed threshold enforcing an SNR larger 5 has been selected. Next, for each cell a mean signal amplitude was calculated as well as the noise of that electrode recording the maximal amplitudes.<sup>[53]</sup> For each cell within a population of 50–100 cells mm<sup>-2</sup> we obtained one SNR value. The histogram of SNR values for four retinas is shown in Figure 2F. Given that the distribution is asymmetric we evaluate the median SNR for the four independent recordings, two using CMOS MEAs and two using metal-based MEAs. The median SNR for ganglion cell signals recorded by metal-based or by capacitive electrodes was ≈6.5, independent of the measurement. In summary, by carefully reviewing and analyzing recordings under identical conditions we have shown here that for one neuronal tissue (the retina) and two biophysically different approaches of electrical imaging the recording quality (SNR) are identical. A comprehensive SNR list comprising recordings from other MEA

types cannot be given here. In the references cited in Table 1, only selected recordings are presented, often without stating the filter settings. Therefore, only the range of reported signal amplitudes is presented.

The last physical parameter to be considered for electrical imaging is the recording frequency. Relevant electrical signals in electrical imaging span several decades—from a few hertz found in slow-wave oscillatory brain activity up to kilohertz regime for mapping axonal signals.<sup>[27,29]</sup> A sampling frequency below 1 Hz may be used for the detection of slow signals generated by glioma cells<sup>[6]</sup> while very fast sampling of ≈20 kHz may be used to reveal the shape of the action potential waveforms. If the high sampling rate of ≈20 kHz is requested for all electrodes (i.e., full imaging) it comes at the cost of high noise level of the recording system and a high data rate (Table 1). Two approaches may alleviate this problematic. Full imaging may be reduced to imaging selected electrode fields using a switch matrix approach<sup>[17]</sup> and appropriate filters may be implemented on the recording hardware to select the desired frequency range and reduced the amount of data storage.<sup>[54]</sup>

To conclude, we have discussed different technological constrains for electrical imaging and how they may affect the interpretation of the data. (i) Filter properties of the recording electrode/sensor, (ii) signal-to-noise ratios, and (iii) spatial and temporal sampling of CMOS MEAs. In the following paragraph, we discuss recent neuroscientific applications of the electrical imaging.

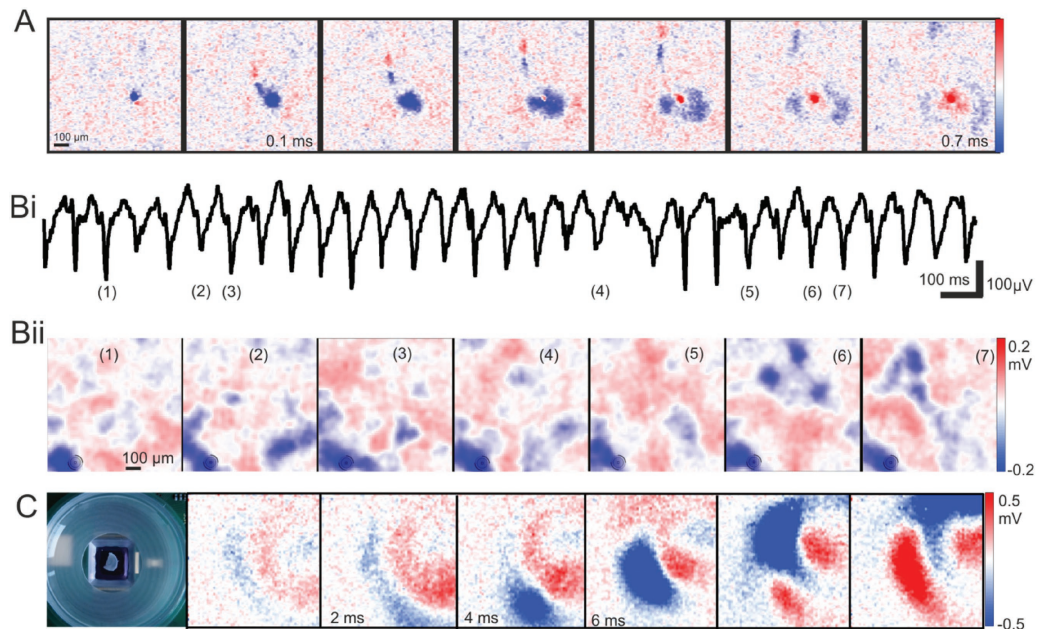


**Figure 3.** Electrical imaging of neuronal activity at different temporal and spatial levels. A) Electrical imaging the propagation of a single action potential along an unmyelinated retinal axon. Adapted with permission.<sup>[43]</sup> Copyright 2010, Frontiers Media. B) Electrical imaging the propagation of local field potentials in blind mouse retina. Frames are presented at selected intervals to demonstrate the oscillatory character but also to visualize yet to be explored differences. Adapted with permission.<sup>[56]</sup> Copyright 2016, Frontiers Media. C) Electrical imaging the propagation of local field potentials along the hippocampal formation. Reproduced with permission.<sup>[57]</sup> Copyright 2014, NMI, Natural and Medical Sciences Institute.

## 2. Applications of Electrical Imaging in Neuroscientific Research

Extracellular recording using electrode arrays, first introduced in 1972 by Thomas et al.<sup>[35]</sup> has by now a long tradition in neuroscientific research and application. The difference between extracellular recording and electrical imaging becomes evident when comparing classical “electrophysiological traces” (Figure 2A–D) to the 2D sequences of electrical images comprising the simultaneously recorded voltages within a defined area. Examples of such electrical images are shown in Figure 3. Instead of displaying hundreds of individual traces

the evolution of the spatiotemporal extracellular voltage is displayed in movie-like manner.

In the following we review work from our lab making use of the high spatial density and the high temporal resolution characteristic for electrical imaging. A comprehensive list of application examples for electrical imaging in neuroscientific research is given in Table 2.

Three applications are reviewed in detail: (i) Electrical imaging of cellular activity propagating within axons (nerve fibers), (ii) electrical imaging of low-frequency field potentials, and (iii) electrical imaging of both—single unit activity and local field potentials.

**Table 2.** Review of published applications using CMOS-based MEAs and electrical imaging.

Application	Results (keywords)	References	Electrical imaging (CMOS MEA)
Retina coding	Functional cell types, axonal conduction, neural coding, correlation analysis	[45,48,58,59]	Yes (eEOSFET–MEA, APS–MEA) no (SM–MEA)
Retinal waves	Oscillatory field potentials, retinal waves, receptive field estimation	[60,61]	Yes (eEOSFET–MEA, APS–MEA)
Brain slices	Disease modeling, analysis local field potentials, single cell identification	[21,40,62,63]	Yes (eEOSFET–MEA, APS–MEA, SM–MEA)
Neuronal cultures	Axonal conduction, cell connectivity, network dysfunction, disease modeling	[64–67]	Yes (eEOSFET–MEA, APS–MEA, SM–MEA)
(iPSC-derived) cardiomyocytes	Drug-induced cardiotoxicity, disease modeling	[68,69]	Not shown
Stem cells	Network dysfunction, disease modeling	[70]	Not shown



Probably the most impressive example of electrical imaging relies on the ability to visualize the activity in subcellular compartments, i.e., the activity within axons and neurites. The visualization of propagating activity has been demonstrated first in retinal axons (Figure 3A),<sup>[45,71,72]</sup> followed by studies on dissociated neuronal cultures<sup>[39,64]</sup> and most recently the electrical images within identified neurons in hippocampal slices.<sup>[40]</sup> While in the retina signals propagate largely nonattenuated within the unmyelinated axons at a speed of 1–2 m s<sup>-1</sup>,<sup>[45,71–73]</sup> the propagation in neurites of neuronal cultures appears to vary on a short local scale due to the kinked structure of the neurites.<sup>[64]</sup> Most recently, the combination of electrical imaging the neurite structure of individual neurons and precise stimulation protocols enabled the identification of presynaptic contribution at multiple sites.<sup>[74]</sup>

The changes of the extracellular voltage caused by correlated transmembrane currents are recorded as local field potentials (LFPs). LFPs represent spatially restricted changes of the extracellular voltage and last, depending on the brain structure between few milliseconds and seconds for slow-wave brain oscillations.

LFPs have been electrically imaged in various brain areas, such as the well-known propagation along the trisynaptic hippocampal formation<sup>[62,63]</sup> or in cortical structures<sup>[75]</sup> revealing epileptiform activities. An example of a propagating LFP along the hippocampal CA region is Figure 3C.<sup>[57]</sup> LFPs in cultured, organotypic<sup>[62]</sup> and in acute hippocampal slices<sup>[63]</sup> have been used to analyze and quantify the effect of antiepileptic drugs. Electrical imaging at a coarser spatial scale discussed the possibility of nonsynaptic propagation of epileptiform activity in the unfolded hippocampus.<sup>[76]</sup>

Another goal of electrical imaging the different layers of the hippocampus is the inference about neuronal circuits. One strategy how this could be achieved has been suggested by electrically imaging the layer-specific distribution of LFP signal power in freely behaving animals.<sup>[77]</sup> Crucial for the inference of neuronal circuitries is the simultaneous recording of both, single unit spiking and low-frequency activity. One example, where this has been achieved is discussed in the following.

Among the first results revealed by electrical imaging in the developing retina was the wave-like activity (“retinal wave”) detected in the ganglion cell layer.<sup>[78]</sup> This activity reflects near-synchronous ganglion cell activity over several millimeters, separated by second-long periods of inactivity. Recently, the electrical imaging at high spatiotemporal resolution revealed shrinkage of these waves during ontogeny down to the size of the spatial receptive fields of retinal ganglion cells,<sup>[60]</sup> indicating a loss of synaptic inputs to the retinal ganglion cell. Whereas in the healthy retina the synchronous output largely disappears it is consistently detected in photoreceptor-degenerated retinas. However, the ganglion cell spiking alone does not provide a complete description of the functional changes occurring in these retinas. Strong subthreshold oscillations of transmembrane potential<sup>[79]</sup> lead to local field potentials, which emerge spontaneously and propagate at different speeds across the retinal layers. A quantitative analysis of the detected LFP indicates a spatial spread over an area of ≈200 μm (see Figure 3B and ref. [61]) suggesting that only a few cells contribute to the initiation of the rhythm. The LFPs recorded in different strains

of photoreceptor-degenerated retinas either propagate due to aberrant electrical coupling or remain largely stationary.<sup>[80]</sup> The electrically imaged LFPs in photoreceptor-degenerated retina occur in synchrony with the detected ganglion cell spiking. Pharmacological blockade of the spiking but not of the LFPs demonstrates that presynaptic cells are responsible for the aberrant oscillatory activity, which in turn leads to rhythmic spiking in the postsynaptic neurons.<sup>[61,80]</sup>

### 3. Future Developments

From a technological perspective electrical imaging has been performed using substrate-integrated, planar electrodes. This restricts the investigation of neuronal networks to 2D cultures or slice preparations. Recently, arrays with 3D nanoelectrodes have been reported, which protrude cardiomyocyte cultures and image the propagation of intracellular voltages within a densely connected culture.<sup>[81]</sup> However, the reported electrode spacing larger 100 μm questions the application of this approach for electrical imaging. Future nanoscale arrays may achieve a resolution in 10 μm range thus extending the capacity of electrical imaging into the third dimension.

Toward circuit reconstruction the described electrical imaging needs to be combined with other neurotechniques. Innovations in optogenetics provide valuable tools for cell-specific modulation. Optogenetic and optical stimulation has been applied in conjunction with CMOS-based MEA,<sup>[82]</sup> demonstrating that the light induced artefact in the recording electrodes can be suppressed, thus revealing single cell spiking. Another, recent application employed recording using high-density microelectrode arrays to investigate the efficiency of firing rate modulation in blind retinas.<sup>[42,83]</sup> Although no full electrical imaging of network activity during optical stimulation has been demonstrated yet, the presented evidence suggests that this will be achieved in the near future.

Here, we reviewed the technique of electrical imaging as a powerful tool for selected applications in neuroscience basic research and technological applications. We foresee applications extending beyond the ones reviewed here when combined with other techniques. Although the examples reviewed here were taken from neuroscience, many other electrogenic cells and networks thereof will be investigated, potentially including the emerging field of stem-cell derived microphysiological systems.<sup>[84]</sup>

### Conflict of Interest

The authors declare no conflict of interest.

### Keywords

brain tissue, electrical imaging, microelectrode arrays, neurons, signal-to-noise ratios

Received: June 5, 2017

Revised: July 27, 2017

Published online: October 9, 2017

- [1] A. Hierlemann, in *2017 IEEE 30th Int. Conf. on Microelectromechanical Systems (MEMS)*, IEEE, Piscataway, NJ **2017**, 199.
- [2] A. Maccione, M. Gandolfo, S. Zordan, H. Amin, S. Di Marco, T. Nieuw, G. N. Angotzi, L. Berdondini, *Brain Res. Bull.* **2015**, *119*, 118.
- [3] R. Thewes, G. Bertotti, N. Dodel, S. Keil, S. Schröder, K.-H. Boven, G. Zeck, M. Mahmud, S. Vassanelli, in *2016 IEEE Int. Symp. on Circuits and Systems (ISCAS)*, IEEE, Piscataway, NJ **2016**, 1826.
- [4] A. Lambacher, V. Vitzthum, R. Zeitler, M. Eickenscheidt, B. Eversmann, R. Thewes, P. Fromherz, *Appl. Phys. A* **2004**, *79*, 1607.
- [5] U. Sumbul, S. Song, K. McCulloch, M. Becker, B. Lin, J. R. Sanes, R. H. Masland, H. S. Seung, *Nat. Commun.* **2014**, *5*, 3512.
- [6] M. E. Spira, A. Hai, *Nat. Nanotechnol.* **2013**, *8*, 83.
- [7] N. Rabieh, S. M. Ojovan, N. Shmoel, H. Erez, E. Maydan, M. E. Spira, *Sci. Rep.* **2016**, *6*, 36498.
- [8] P. R. Rocha, P. Schlett, U. Kintzel, V. Mailänder, L. K. Vandamme, G. Zeck, H. L. F. Gomes, F. Biscarini, D. M. De Leeuw, *Sci. Rep.* **2016**, *6*, 34843.
- [9] S. Schonecker, U. Kraushaar, M. Dufer, A. Sahr, C. Hardtner, E. Guenther, R. Walther, U. Lendeckel, W. Barthlen, P. Krippel-Drews, G. Drews, *Integr. Biol.* **2014**, *6*, 540.
- [10] G. Buzsáki, C. A. Anastassiou, C. Koch, *Nat. Rev. Neurosci.* **2012**, *13*, 407.
- [11] M. E. Obien, K. Deligkaris, T. Bullmann, D. Bakkum, U. Frey, *Front. Neurosci.* **2014**, *8*, 423.
- [12] J. C. Fiala, K. M. Harris, *Dendrite Structure*, Oxford University Press Inc., New York **1999**.
- [13] C.-J. Jeon, E. Strettoi, R. H. Masland, *J. Neurosci.* **1998**, *18*, 8936.
- [14] G. Kempermann, H. G. Kuhn, F. H. Gage, *Nature* **1997**, *386*, 493.
- [15] G. Bertotti, D. Velychko, N. Dodel, S. Keil, D. Wolansky, B. Tillak, M. Schreiter, S. Röhler, G. Zeck, R. Thewes, in *2014 IEEE Biomedical Circuits and Systems Conf. (BioCAS)*, IEEE, Piscataway, NJ **2014**, 304.
- [16] B. Eversmann, M. Jenkner, F. Hofmann, C. Paulus, R. Brederlow, B. Holzapfel, P. Fromherz, M. Merz, M. Brenner, M. Schreiter, R. Gabl, K. Plehnert, M. Steinhauser, G. Eckstein, D. Schmitt-Landsiedel, R. Thewes, *IEEE J. Solid-State Circuits* **2003**, *38*, 2306.
- [17] F. Heer, S. Hafizovic, T. Ugniwenko, U. Frey, W. Franks, E. Perriard, A. Blau, C. Ziegler, A. Hierlemann, *Biosens. Bioelectron.* **2007**, *22*, 2546.
- [18] L. Berdondini, K. Imfeld, A. Maccione, M. Tedesco, S. Neukom, M. Koudelka-Hep, S. Martinoia, *Lab Chip* **2009**, *9*, 2644.
- [19] R. Huys, D. Braeken, D. Jans, A. Stassen, N. Collaert, J. Wouters, G. Callewaert, *Lab Chip* **2012**, *12*, 1274.
- [20] V. Viswam, J. Dragas, A. Shadmani, Y. Chen, A. Stettler, J. Müller, A. Hierlemann, in *2016 IEEE Int. Solid-State Circuits Conf. (ISSCC)*, IEEE, Piscataway, NJ **2016**, 394.
- [21] U. Frey, U. Egert, F. Heer, S. Hafizovic, A. Hierlemann, *Biosens. Bioelectron.* **2009**, *24*, 2191.
- [22] X. Yuan, S. Kim, J. Juyon, M. D'Urbino, T. Bullmann, Y. Chen, A. Stettler, A. Hierlemann, U. Frey, in *2016 IEEE Symp. on VLSI Circuits*, IEEE, Piscataway, NJ **2016**.
- [23] R. Gerwig, K. Fuchsberger, B. Schröppel, G. S. Link, G. Heusel, U. Kraushaar, W. Schuhmann, A. Stett, M. Stelzle, *Front. Neuroeng.* **2012**, *5*, 8.
- [24] W. Franks, I. Schenker, P. Schmutz, A. Hierlemann, *IEEE Trans. BME* **2005**, *52*, 1295.
- [25] T. Gabay, M. Ben-David, I. Kalifa, R. Sorkin, Z. R. Abrams, E. Ben-Jacob, Y. Hanein, *Nanotechnology* **2007**, *18*, 035201.
- [26] M. Eickenscheidt, M. Jenkner, R. Thewes, P. Fromherz, G. Zeck, *J. Neurophysiol.* **2012**, *107*, 2742.
- [27] R. Zeitler, P. Fromherz, G. Zeck, *Appl. Phys. Lett.* **2011**, *99*, 263702.
- [28] M. Voelker, P. Fromherz, *Phys. Rev. Lett.* **2006**, *96*, 228102.
- [29] R. Zeitler, P. Fromherz, *Langmuir* **2013**, *29*, 6084.
- [30] P. Fromherz, in *Bioelectronics: From Theory to Applications* (Eds: I. Willner, E. Katz), Wiley, Weinheim, Germany **2005**, pp. 339–394.
- [31] P. Fromherz, M. Voelker, *Science* **2009**, *323*, 1429.
- [32] B. P. Timko, F. Patolsky, C. M. Lieber, *Science* **2009**, *323*, 1429.
- [33] M. Voelker, P. Fromherz, *Small* **2005**, *1*, 206.
- [34] J. Wuchter, S. Beuter, F. Treindl, T. Herrmann, G. Zeck, M. Templin, H. J. Volkmer, *J. Neurosci.* **2012**, *32*, 14821.
- [35] N. Shmoel, N. Rabieh, S. M. Ojovan, H. Erez, E. Maydan, M. E. Spira, *Sci. Rep.* **2016**, *6*, 27110.
- [36] M. Jenkner, P. Fromherz, *Phys. Rev. Lett.* **1997**, *79*, 4705.
- [37] C. Xie, Z. Lin, L. Hanson, Y. Cui, B. Cui, *Nat. Nanotechnol.* **2012**, *7*, 185.
- [38] L. Pan, S. Alagapan, E. Franca, T. DeMarse, G. J. Brewer, B. C. Wheeler, *IEEE Trans. Neural Syst. Rehabil. Eng.* **2014**, *22*, 453.
- [39] M. K. Lewandowska, D. J. Bakkum, S. B. Rompani, A. Hierlemann, *PLoS One* **2015**, *10*, e0118514.
- [40] W. Gong, J. Sencar, D. J. Bakkum, D. Jackel, M. E. Obien, M. Radivojevic, A. Hierlemann, *Front. Neurosci.* **2016**, *10*, 537.
- [41] D. A. Henze, Z. Borhegyi, J. Csicsvari, A. Mamiya, K. D. Harris, G. Buzsáki, *J. Neurophysiol.* **2000**, *84*, 390.
- [42] G. Bertotti, F. Jetter, S. Keil, N. Dodel, M. Schreiter, D. Wolansky, C. Boucsein, G. Zeck, R. Thewes, *IEEE Electron Device Lett.* **2017**, *38*, 967.
- [43] H. Stutzki, C. Leibig, A. Andreadaki, D. Fischer, G. Zeck, *Front. Cell. Neurosci.* **2014**, *8*, 38.
- [44] H. Kasi, R. Meissner, A. Babalian, H. Van Lintel, A. Bertsch, P. Renaud, *J. Electr. Bioimpedance* **2011**, *1*, 84.
- [45] G. Zeck, A. Lambacher, P. Fromherz, *PLoS One* **2011**, *6*, 20810.
- [46] F. Jetter, G. Bertotti, R. Thewes, G. Zeck, *Front. Neurosci.* **2016**, *97*, <https://doi.org/10.3389/conf.fnins.2016.93.00097>.
- [47] A. M. Litke, N. Bezayiff, E. J. Chichilnisky, W. Cunningham, W. Dabrowski, A. A. Grillo, M. Grivich, *IEEE Trans. Nucl. Sci.* **2004**, *51*, 1434.
- [48] M. Fiscella, F. Franke, K. Farrow, J. Müller, B. Roska, R. A. da Silveira, A. Hierlemann, *J. Neurophysiol.* **2015**, *114*, 2485.
- [49] F. Franke, M. Natora, C. Boucsein, M. H. J. Munk, K. Obermayer, *J. Comput. Neurosci.* **2010**, *29*, 127.
- [50] O. Marre, D. Amodei, N. Deshmukh, K. Sadeghi, F. Soo, T. E. Holy, M. J. Berry, *J. Neurosci.* **2012**, *32*, 14859.
- [51] C. Leibig, T. Wachtler, G. Zeck, *J. Neurosci. Methods* **2016**, *271*, 1.
- [52] K. D. Harris, D. A. Henze, J. Csicsvari, H. Hirase, G. Buzsáki, *J. Neurophysiol.* **2000**, *84*, 401.
- [53] R. Q. Quiroga, Z. Nadasdy, Y. Ben-Shaul, *Neural Comput.* **2004**, *16*, 1661.
- [54] I. Gupta, A. Serb, A. Khait, R. Zeitler, S. Vassanelli, T. Prodnomakis, *Nat. Commun.* **2016**, *7*, 12805.
- [55] C. A. Thomas, P. A. Springer, G. E. Loeb, Y. Berwald-Netter, L. M. Okun, *Exp. Cell Res.* **1972**, *74*, 61.
- [56] G. Zeck, *Front. Cell. Neurosci.* **2016**, *10*, 25.
- [57] L. Channappa, F. Helmhold, G. Zeck, in *Proc. 9th Int. Meeting on Substrate-Integrated Microelectrodes* (Ed: A. Stett), NMI, Reutlingen, Germany **2014**.
- [58] F. Franke, M. Fiscella, M. Sevelev, B. Roska, A. Hierlemann, R. A. da Silveira, *Neuron* **2016**, *89*, 409.
- [59] G. Portelli, J. M. Barrett, G. Hilgen, T. Masquelier, A. Maccione, S. Di Marco, L. Berdondini, K. Kornprobst, E. Sernagor, *eNeuro* **2016**, *3*, 0134.
- [60] A. Maccione, M. H. Hennig, M. Gandolfo, O. Muthmann, J. van Coppenhagen, S. J. Eglén, L. Berdondini, E. Sernagor, *J. Physiol.* **2014**, *592*, 1545.
- [61] J. Menzler, G. Zeck, *J. Neurosci.* **2011**, *31*, 2280.
- [62] M. Hutzler, A. Lambacher, B. Eversmann, M. Jenkner, R. Thewes, P. Fromherz, *J. Neurophysiol.* **2006**, *96*, 1638.
- [63] E. Ferrea, A. Maccione, L. Medrihan, T. Nieuw, D. Ghezzi, P. Baldelli, F. Benfenati, L. Berdondini, *Front. Neural Circuits* **2012**, *6*, 80.



- [64] D. J. Bakkum, U. Frey, M. Radivojevic, T. L. Russell, J. Müller, M. Fiscella, H. Takahashi, A. Hierlemann, *Nat. Commun.* **2013**, *4*, 2181.
- [65] A. Lambacher, V. Vitzthum, R. Zeitler, M. Eickenscheidt, B. Eversmann, R. Thewes, P. Fromherz, *Appl. Phys. A* **2011**, *102*, 1.
- [66] A. Maccione, M. Garofalo, T. Nieuws, M. Tedesco, L. Berdondini, S. Martinoia, *J. Neurosci. Methods* **2012**, *207*, 161.
- [67] M. Radivojevic, D. Jackel, M. Altermatt, J. Müller, V. Viswam, A. Hierlemann, D. J. Bakkum, *Sci. Rep.* **2016**, *6*, 31332.
- [68] D. Jans, G. Callewaert, O. Krylychkina, L. Hoffman, F. Gullo, D. Prodanov, D. Braeken, *J. Pharmacol. Toxicol. Methods* **2017**, *87*, 48.
- [69] C. D. Sanchez-Bustamante, U. Frey, J. M. Kelm, A. Hierlemann, M. Fussenegger, *Tissue Eng., Part A* **2008**, *14*, 1969.
- [70] H. Amin, T. Nieuws, D. Lonardoni, A. Maccione, L. Berdondini, *Sci. Rep.* **2017**, *7*, 2460.
- [71] M. Greschner, G. D. Field, P. H. Li, M. L. Schiff, J. L. Gauthier, D. Ahn, A. Sher, A. M. Litke, E. J. Chichilnisky, *J. Neurosci.* **2014**, *34*, 3597.
- [72] M. Greschner, A. K. Heitman, G. D. Field, P. H. Li, D. Ahn, A. Sher, A. M. Litke, E. J. Chichilnisky, *Curr. Biol.* **2016**, *26*, 1935.
- [73] P. H. Li, J. L. Gauthier, M. Schiff, A. Sher, D. Ahn, G. D. Field, M. Greschner, E. M. Callaway, A. M. Litke, E. J. Chichilnisky, *J. Neurosci.* **2015**, *35*, 4663.
- [74] D. Jackel, D. J. Bakkum, T. L. Russell, J. Müller, M. Radivojevic, U. Frey, F. Franke, A. Hierlemann, *Sci. Rep.* **2017**, *7*, 978.
- [75] J. Viventi, D. H. Kim, L. Vigeland, E. S. Frechette, J. A. Blanco, Y. S. Kim, A. E. Avrin, V. R. Tiruvadi, S. W. Hwang, A. C. Vanleer, D. F. Wulsin, K. Davis, C. E. Gelber, L. Palmer, J. Van der Spiegel, J. Wu, J. Xiao, Y. Huang, D. Contreras, J. A. Rogers, B. Litt, *Nat. Neurosci.* **2012**, *14*, 1599.
- [76] M. Zhang, T. P. Ladas, C. Qiu, R. S. Shivacharan, L. E. Gonzalez-Reyses, D. M. Durand, *J. Neurosci.* **2014**, *34*, 1409.
- [77] A. Berényi, Z. Somogyvári, A. J. Nagy, L. Roux, J. D. Long, S. Fujisawa, E. Stark, A. Leonardo, T. D. Harris, G. Buzsáki, *J. Neurophysiol.* **2014**, *111*, 1132.
- [78] M. Meister, R. O. Wong, D. A. Baylor, C. J. Shatz, *Science* **1991**, *252*, 939.
- [79] H. Choi, L. Zhang, D. Butts, J. H. Singer, H. Riecke, *J. Neurophysiol.* **2014**, *112*, 1492.
- [80] J. Menzler, L. Channappa, G. Zeck, *PLoS One* **2014**, *9*, e106047.
- [81] J. Abbott, T. Ye, L. Qin, M. Jorgolli, R. S. Gertner, D. Ham, H. Park, *Nat. Nanotechnol.* **2017**, *12*, 460.
- [82] M. Welkenhuysen, L. Hoffman, Z. Luo, A. De Proft, C. Van den Haute, V. Baekelandt, Z. Debyser, G. Gielen, R. Puers, D. Braeken, *Sci. Rep.* **2016**, *6*, 20353.
- [83] J. M. Barrett, G. Hilgen, E. Sernagor, *Sci. Rep.* **2016**, *6*, 33565.
- [84] J. P. Wikswo, *The Relevance and Potential Roles of Microphysiological Systems in Biology and Medicine*, SAGE Publications, **2014**.



# Optical Stimulation Effects on TiO<sub>2</sub> Sensor Dielectric Used in Capacitively-Coupled High-Density CMOS Microelectrode Array

Gabriel Bertotti, Florian Jetter, Stefan Keil, Normal Dodel, Matthias Schreiter, Dirk Wolansky, Clemens Boucsein, Karl-Heinz Boven, Günther Zeck, and Roland Thewes

**Abstract**—The effect of optical stimulation of neural tissue is considered in capacitively coupled CMOS microelectrode arrays used for *in vitro* extracellular recording from neural tissue. Using a 25-nm high-k TiO<sub>2</sub> sensor dielectric with 20% ZrO<sub>2</sub>, light-induced currents through the dielectric are found at short wavelengths within the visible and relevant spectrum for the above-mentioned purpose. Purely capacitive behavior is obtained for green light and longer wavelength, leakage-induced artifacts at shorter wavelengths are avoided by using optimized operating conditions of recording sites and entire system.

**Index Terms**—Microelectrode array (MEA), CMOS-MEA, nerve signals, neural tissue recording and stimulation, optical stimulation, dielectric interface.

## I. INTRODUCTION

SUBSTRATE-INTEGRATED microelectrode arrays (MEAs) are widely used for in-vitro interfacing experiments with nerve cells and neural tissue [1]–[4]. They consist of a number of recording sites distributed in a 2D plane to monitor nerve signals, i.e. action potentials and/or local field potentials.

Aiming for increased spatial resolution, CMOS MEAs have been developed with active areas of order 1 – 10 mm<sup>2</sup>, up to several 10 000 interfacing sites, and active circuitry to amplify, multiplex, and process signals directly on-chip [5]–[12]. At the interface to the world of biology they either use noble metal electrodes [7]–[11] or purely-capacitively coupled sites consisting of a thin high-k dielectric covering thin metal layers on the surface of fully processed CMOS chips [5], [6], [12].

Manuscript received April 11, 2017; accepted April 27, 2017. Date of publication May 8, 2017; date of current version June 23, 2017. This work was supported by the German Ministry of Education and Research and Projektträger Jülich under Grant 031L0059C and Grant 031L0059A. The review of this letter was arranged by Editor C. V. Mouli. (Corresponding author: Roland Thewes.)

G. Bertotti, S. Keil, N. Dodel, and R. Thewes are with the Chair of Sensor and Actuator Systems, Technical University of Berlin, 10623 Berlin, Germany (e-mail: roland.thewes@tu-berlin.de).

F. Jetter and G. Zeck are with the Natural and Medical Sciences Institute, University of Tübingen, 72074 Reutlingen, Germany.

M. Schreiter is with the Siemens AG Corporate Technology, 81739 Munich, Germany.

D. Wolansky is with the for High Performance Microelectronics/Leibniz-Institut für innovative Mikroelektronik, 15236 Frankfurt (Oder), Germany. C. Boucsein and K.-H. Boven are with the Multi Channel Systems GmbH, 72770 Reutlingen, Germany.

Color versions of one or more of the figures in this letter are available online at <http://ieeexplore.ieee.org>.

Digital Object Identifier 10.1109/LED.2017.2701901

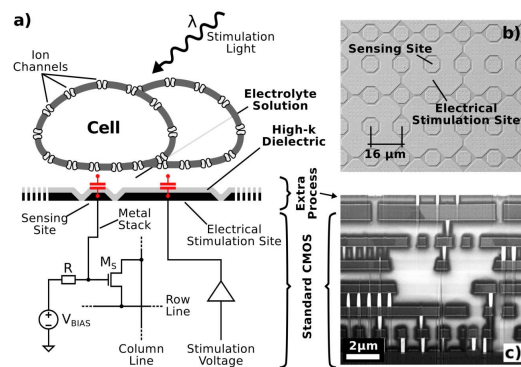


Fig. 1. a) Schematic overview of the entire considered system. (65 × 65 recording sites, 32 × 32 stimulation sites. Recording site diameter ≈ 8 µm, recording site pitch 16 µm, further details cf. [12]). b) Top view of the chip surface. c) Cross-section of the manufactured and post-processed CMOS chip.

In many MEA applications, not only recording is required but also neural tissue stimulation capability. Electrical stimulation is enabled by applying suitable signals to the recording sites or dedicated stimulation sites. As electrical stimulation signals are orders of magnitude bigger than recorded neural signals, recording capability during and directly after application of a stimulus may severely suffer from electrical artifacts like cross-talk, electrode polarization, etc ... [13], [14]. In the case of optical stimulation of light-sensitive ion channels (optogenetics) or of light-sensitive neural tissue (i.e. retina) a wide range of wavelengths are used. Optogenetic activation occurs in the range between 470 nm and 600 nm [15], whereas optical stimulation of retinal tissue is based on the spectral sensitivity of the light-detecting photoreceptors and ranges from 370 nm to 650 nm [16].

In this letter, we report on the impact of optical stimulation applied to a CMOS MEA equipped with a high-k dielectric interface as depicted in Fig. 1 [12]. Moreover, we consider the consequences for chip operation. The related chips are manufactured on the basis of a standard 180 nm, 1.8 V CMOS process with six metal layers. A TiN layer with approx. 25 nm thickness is deposited and structured in a post-CMOS-process on top of the CMOS wafer followed by sputtering of a 25 nm high-k ( $\epsilon_r \approx 40$ ) TiO<sub>2</sub> dielectric with 20% Zr.

**II. EXPERIMENTAL**

I/V characteristics of the dielectric are measured as a function of the potential applied to the electrolyte solution on the chip's surface - in a real experiment the culture medium with biological content. For this purpose, a custom potentiostat is used with Pt counter electrode and Ag/AgCl reference electrode, and a voltage is applied to the potentiostat's input (for simplicity called "bath voltage" in the following). All TiN stimulation and sensing sites of the post-processed CMOS chip are held at ground potential using a semiconductor analyzer (Agilent B1500A) to measure the current through the dielectric. The measured current is normalized to the total area of the TiN sites (approx. 4.1 mm<sup>2</sup>). If not otherwise specified, all measurements are performed with a 1 M solution of NaCl. The chip is operated in a light-shielded setup. To illuminate its surface, LEDs are used with center wavelengths of 875 nm (infrared), 625 nm (red), 525 nm (green), 475 nm (blue), and 412 nm (violet), and full-width half-maximum (FWHM) values of 37 nm, 25 nm, 30 nm, 25 nm, and 5 nm, respectively. In all cases, an irradiance of 100 μW mm<sup>-2</sup> is applied. This value corresponds to retinal stimulation in bright, daylight conditions [17] but is smaller than in most optogenetic applications [15].

**III. RESULTS AND DISCUSSION**

In Fig. 2a), I/V characteristics of our dielectric in contact with different electrolyte solutions are depicted performed in the dark. The results agree very well with the data published in [12], [18], [19]. Within a 4 V wide voltage window centered around -2V excellent insulation is achieved with dielectric leakage current densities below 10 nA cm<sup>-2</sup>. For comparison, the data of an uncovered TiN electrode without dielectric are shown as well.

The effect of illumination on the dielectric leakage current is highlighted in Fig. 2b) as a function of light wavelength and applied bath voltage. Within the range of infrared to green irradiance the measured I/V curves do not show relevant deviations from the data measured without illumination. Using blue illumination (475 nm ± 12.5 nm FWHM), a maximum leakage current of 25 nA cm<sup>-2</sup> is achieved. Whereas this effect is detectable by adequate instrumentation its strength is sufficiently small so that the chip's interface to the biological world can still be considered to behave mainly capacitively. In contrast, using violet illumination (412 nm ± 2.5 nm FWHM), the leakage current through the dielectric significantly increases and a clear bath voltage dependence is found for values between -2V and -0.5V. In order to report the related relationship of the considered parameters in a comprehensive manner, in the inset of Fig. 2b) the leakage current is plotted as a function of applied biasing voltage for the different illumination wavelengths.

The effect of illumination at short wavelengths (blue and violet) is further investigated by means of a cyclic voltammetry experiment. Here, the bath voltage is swept force and back between -1.0V and +0.5V with a scan rate of 33.3 mV s<sup>-1</sup> and the resulting current is measured. Results are shown in Fig. 3. As can be seen from the voltammogram in Fig. 3a), except for the region around 0V the data without and with blue light illumination are very similar. The plateaus of the respective curves indicate that here mainly a displacement current occurs, i.e. the dielectric is predominantly characterized by capacitive behavior. The by far more tilted

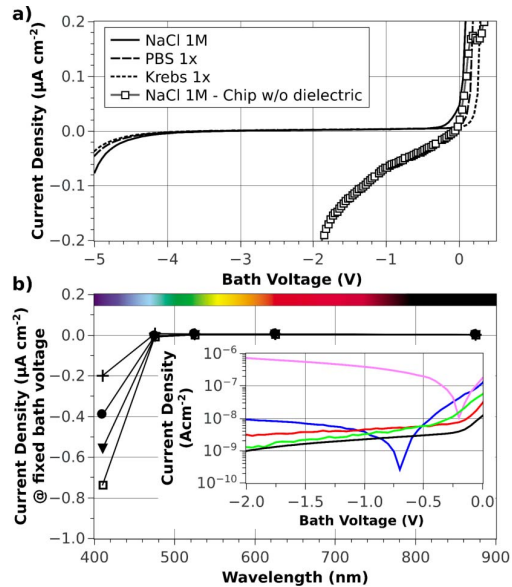


Fig. 2. a) Measured dielectric leakage current as a function of bath voltage for various electrolyte solutions. Moreover, for comparison a measurement without dielectric is shown with the TiN electrodes of the chip being in direct contact to a 1M NaCl electrolyte solution. b) Measured dielectric leakage current under illumination at 100 μW mm<sup>-2</sup> as a function of illumination wavelength for various bath voltages: -0.5V (+), -1.0V (•), -1.5V (▼), -2.0V (□). Inset: leakage current as a function of applied biasing voltage for the illumination wavelengths used: 875 nm (black), 625 nm (red), 525 nm (green), 475 nm (blue), 412 nm (violet).

curves in the case of violet light reveal that other components than pure displacement effects contribute to the total current. In order to study this behavior in more detail, the small signal conductance per area,  $\partial(\text{current density})/\partial(\text{bath voltage})$ , is computed and displayed in Fig. 3b).

For negative values of  $\partial(\text{bath voltage})/\partial(\text{time})$  [Fig 3b)], within the entire depicted bath voltage window the data without and with blue light illumination show approximately zero conductance. For violet light, however, always a value above zero conductance is found which originates from non-capacitive mechanisms. For positive values of  $\partial(\text{bath voltage})/\partial(\text{time})$  [Fig. 3c)], for bath voltages below -0.5V again a purely capacitive behavior is obtained without and with blue light illumination. For bath voltages close to 0V, both currents show an increase above zero due to cyclovoltamm-typical redox reactions in the electrolyte. For violet light, significantly higher current densities are found throughout the entire bath voltage regime confirming that in this case other mechanisms but pure displacement currents provide a non-negligible contribution.

The non-displacement current related portion of the total current measured under violet illumination can be explained in terms of (i) electrons in the solution surpassing the dielectric-solution energy barrier, and (ii) electron-hole pair generation inside the dielectric [20], [21]. To a first order approximation, electron-hole pairs are only generated by absorbed photons with an energy higher than the dielec-

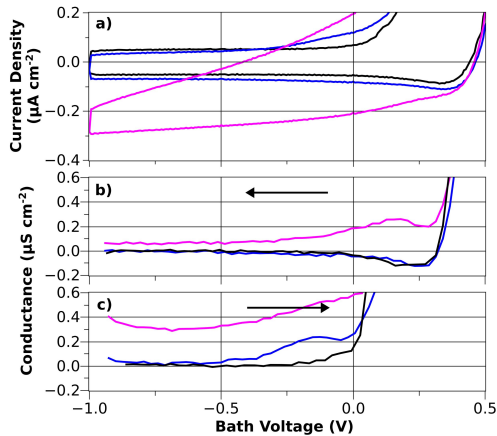


Fig. 3. a) Voltammogram without (black curve) and with illumination at different wavelengths (blue and violet light, blue and violet curves). Scan rate =  $33.3 \text{ mV s}^{-1}$ . b) Small signal conductance per area computed from the voltammogram in a) for decreasing ( $\leftarrow$ ) bath voltages with time. c) Same as b), but for increasing ( $\rightarrow$ ) bath voltages with time. Color code same as in a).

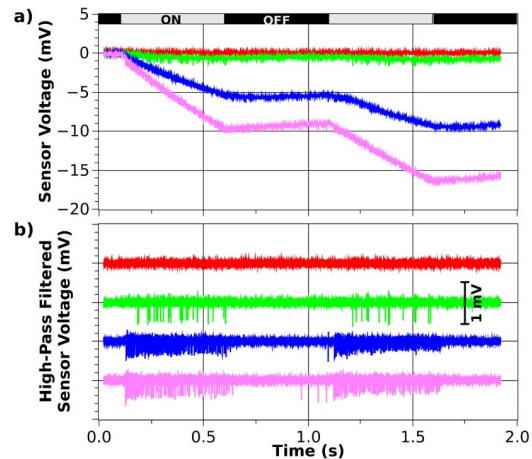


Fig. 4. Measured light-induced neural activity in retinal ganglion cells (RGC) from mouse. An on-off full-field stimulus is used. The color code refers to the wavelength used in this experiment: red = 635 nm, green = 525 nm, blue = 470 nm, violet = 405 nm. Due to the cells' chromatic sensitivity spike activity is not elicited by red light [25]. Same retina and same recording site for all data shown here. a) Raw data. b) High-pass filtered data (cutoff frequency = 100 Hz).

trical energy bandgap. Considering pure TiO<sub>2</sub> (bandgap  $\approx 3.0 \text{ eV}$  [22]), the maximum wavelength which is able to bear electron-hole pair generation in the dielectric is 413 nm. This value correlates well with the findings in Fig. 2b) where the abrupt increase in the dielectric's current occurs at a wavelength shorter than 475 nm. We therefore speculate that the current increase at short wavelengths is mainly driven by electron-hole pair generation rather than electrons in the electrolyte surpassing the dielectric-solution energy barrier.

In order to evaluate the impact of these findings on biological applications, the electrical activity of retinal ganglion cells (RGCs) from mouse retina is recorded under optical stimulation using the capacitively-coupled CMOS MEA considered in this work. In the mouse retina studied here the selectivity of RGCs to stimulation of S-cone cells (violet and blue light) and M-cone cells (blue and green light) is investigated [23]. More than 100 retinal ganglion cells per  $\text{mm}^2$  can be identified, with several distinct chromatic sensitivities [24]. In Fig. 4 we present the chromatic response of one single cell, identified on several adjacent sites. Only the voltage recorded by the sensing site located most closely to the cell is shown. Bath voltage equals 0 V here. As can be seen in Fig. 4a) under violet illumination a shift of the operating point of approx.  $20 \text{ mV s}^{-1}$  is obtained. Given the dynamic range of our entire system, this shift does not lead to measurement deteriorations for at least  $5 \dots 10 \text{ s}$  under 50% duty-cycle illumination. This time interval is noticeably prolonged when lower irradiance values are used. Moreover, given that resistor R in Fig. 1a) is a MOSFET in the practical implementation controlled by an externally applied signal, the node voltage can be reset if the total drift is too large. Last but not least, from the inset in Fig. 2b) it can be seen that for a bath voltage of  $-250 \text{ mV}$  an optimum is achieved with overall 7-fold lower leakage compared to the leakage under violet illumination at a bath voltage of 0 V.

In conclusion, fortunately the CMOS MEA's recording capability is not compromised by the dielectric's leakage at short wavelengths. We would like to mention that the impact of illumination directly on the CMOS circuitry can be excluded: for this purpose the layout of the six metal layers is arranged in a way that these do not only serve as electrical interconnects but also provide an efficient light shield for the active CMOS devices in the silicon substrate. For long wavelengths there is no drift of the operating point at all as reported in Fig. 4a). To investigate the CMOS chip's behavior at short wavelengths, a chip without dielectric is illuminated with blue and violet light, but drift is not obtained.

#### IV. CONCLUSION

The effect of light stimuli has been investigated on the electrical properties of a 25 nm high-k TiO<sub>2</sub> sensor dielectric with 20% ZrO<sub>2</sub> in capacitively coupled CMOS MEAs. Illumination from near infrared to visible light with wavelengths down to approx. 500 nm does not change the dielectric's insulation behavior at all. For shorter wavelengths the onset of additional voltage-dependent leakage currents through the dielectric is observed which is weak for blue (475 nm) and more pronounced for violet light (412 nm). Proper recording capability, however, has been demonstrated for all wavelengths even under violet illumination.

#### REFERENCES

- [1] A. Stett, U. Ebert, E. Guenther, F. Hofmann, T. Meyer, W. Nisch, and H. Haemmerle, "Biological application of microelectrode arrays in drug discovery and basic research," *Anal. Bioanal. Chem.*, vol. 377, no. 3, pp. 486–495, 2003.
- [2] M. Taketani and M. Baudry, *Advances in Network Electrophysiology: Using Multi-Electro Arrays*. New York, NY, USA: Springer, 2006.

- [3] M. E. J. Obien, K. Deligkaris, T. Bullmann, D. J. Bakkum, and U. Frey, "Revealing neuronal function through microelectrode array recordings," *Frontiers Neurosci.*, vol. 8, pp. 1–423, Jan. 2014, doi: 10.3389/fnins.2014.00423.
- [4] R. Thewes, G. Bertotti, N. Dodel, S. Keil, S. Schröder, K.-H. Boven, G. Zeck, M. Mahmud, and S. Vassanelli, "Neural tissue and brain interfacing CMOS devices—An introduction to state-of-the-art, current and future challenges," in *Proc. IEEE Int. Symp. Circuits Syst. (ISCAS)*, May 2016, pp. 1826–1829.
- [5] B. Eversmann, M. Jenkner, F. Hofmann, C. Paulus, R. Bredlerow, B. Holzapfl, P. Fromherz, M. Brenner, M. Schreiter, R. Gabl, K. Plehnert, M. Steinhauser, G. Eckstein, D. Schmitt-Landsiedel, and R. Thewes, "A 128×128 CMOS bio-sensor array for extracellular recording of neural activity," in *Proc. IEEE Int. Solid-State Circuits Conf.*, Feb. 2003, pp. 2306–2317, doi: 10.1109/ISSC.2003.819174.
- [6] B. Eversmann, A. Lambacher, T. Gerling, A. Kunze, P. Fromherz, and R. Thewes, "A neural tissue interfacing chip for in-vitro applications with 32 k recording/stimulation channels on an active area of 2.6 mm<sup>2</sup>," in *Proc. Eur. Solid-State Circuits Conf.*, Sep. 2011, pp. 211–214, doi: 10.1109/ESSCIRC.2011.6044902.
- [7] K. Imfeld, S. Neukom, A. Maccione, Y. Bornat, S. Martinoia, P. A. Farine, M. Koudelka-Hep, and L. Berdonini, "Large-scale, high-resolution data acquisition system for extracellular recording of electrophysiological activity," *IEEE Trans. Biomed. Eng.*, vol. 55, no. 8, pp. 2064–2073, Aug. 2008, doi: 10.1109/TBME.2008.919139.
- [8] U. Frey, J. Sedivy, F. Heer, R. Pedron, M. Ballini, J. Mueller, D. Bakkum, S. Hafizovic, F. D. Faraci, F. Greve, K. U. Kirstein, and A. Hierlemann, "Switch-matrix-based high-density microelectrode array in CMOS technology," *IEEE J. Solid-State Circuits*, vol. 45, no. 2, pp. 467–482, Feb. 2010, doi: 10.1109/JSSC.2009.2035196.
- [9] A. Maccione, A. Simi, T. Nieuw, M. Gandolfo, K. Imfeld, E. Ferrea, E. Sernagor, and L. Berdonini, "Sensing and actuating electrophysiological activity on brain tissue and neuronal cultures with a high-density CMOS-MEA," in *Proc. 17th Int. Conf. Solid-State Sensors, Actuators, Microsystems (TRANSDUCERS)*, Jun. 2013, pp. 752–755, doi: 10.1109/Transducers.2013.6626875.
- [10] M. Ballini, J. Müller, P. Livi, Y. Chen, U. Frey, A. Stettler, A. Shadmani, V. Viswam, I. L. Jones, D. Jackel, M. Radivojevic, M. K. Lewandowska, W. Gong, M. Fiscella, D. J. Bakkum, F. Heer, and A. Hierlemann, "A 1024-channel CMOS microelectrode array with 26,400 electrodes for recording and stimulation of electrogenic cells in vitro," *IEEE J. Solid-State Circuits*, vol. 49, no. 11, pp. 2705–2719, Nov. 2014, doi: 10.1109/JSSC.2014.2359219.
- [11] V. Viswam, J. Dragas, A. Shadmani, Y. Chen, A. Stettler, J. Müller, and A. Hierlemann, "Multi-functional microelectrode array system featuring 59,760 electrodes, 2048 electrophysiology channels, impedance and neurotransmitter measurement units," in *Proc. IEEE Int. Solid-State Circuits Conf. (ISSCC)*, Jan./Feb. 2016, pp. 394–396, doi: 10.1109/ISSCC.2016.7418073.
- [12] G. Bertotti, D. Velychko, N. Dodel, S. Keil, D. Wolansky, B. Tillak, M. Schreiter, A. Grall, P. Jesinger, S. Rohler, M. Eickenscheidt, A. Stett, A. Moller, K.-H. Boven, G. Zeck, and R. Thewes, "A CMOS-based sensor array for in-vitro neural tissue interfacing with 4225 recording sites and 1024 stimulation sites," in *Proc. IEEE Biomed. Circuits Syst. Conf. (BioCAS)*, Oct. 2014, pp. 304–307, doi: 10.1109/BioCAS.2014.6981723.
- [13] D. R. Merrill, M. Bikson, and J. G. R. Jefferys, "Electrical stimulation of excitable tissue: design of efficacious and safe protocols," *J. Neurosci. Methods*, vol. 141, no. 2, pp. 171–198, 2005, doi: 10.1016/j.jneumeth.2004.10.020.
- [14] S. F. Cogan, "Neural stimulation and recording electrodes," *Annu. Rev. Biomed. Eng.*, vol. 10, no. 1, pp. 275–309, 2008, doi: 10.1146/annurev.bioeng.10.061807.160518.
- [15] O. Yizhar, L. Fenno, T. J. Davidson, M. Mogri, and K. Deisseroth, "Optogenetics in neural systems," *Neuron*, vol. 71, no. 1, pp. 9–34, 2011, doi: 10.1016/j.neuron.2011.06.004.
- [16] J. K. Bowmaker and H. J. Dartnall, "Visual pigments of rods and cones in a human retina," *J. Physiol.*, vol. 29, no. 1, pp. 501–511, 1980.
- [17] T. Santos-Ferreira, K. Postel, H. Stutzki, T. Kurth, G. Zeck, and M. Ader, "Daylight vision repair by cell transplantation," *STEM CELLS*, vol. 33, no. 1, pp. 79–90, Jan. 2015, doi: 10.1002/stem.1824.
- [18] F. Wallrapp, P. Fromherz, F. Wallrap, and P. Fromherz, "TiO<sub>2</sub> and HfO<sub>2</sub> in electrolyte-oxide-silicon configuration for applications in bioelectronics," *J. Appl. Phys.*, vol. 99, no. 11, p. 114103, Jun. 2006, doi: 10.1063/1.2199707.
- [19] S. Schröder, Ö. Dogan, J. Schneidewind, G. Bertotti, S. Keil, H. Gargouri, M. Arens, E. Brose, J. Bruns, D. Wolanski, B. Tillack, S. Vassanelli, B. Szyszka, and R. Thewes, "Three dimensional ALD of TiO<sub>2</sub> for in-vivo biomedical sensor applications," in *Proc. IEEE Int. Workshop Adv. Sensors Interfaces*, Jun. 2015, pp. 21–24, doi: 10.1109/IWASI.2015.7184978.
- [20] H. Gerischer, "The impact of semiconductors on the concepts of electrochemistry," *Electrochim. Acta*, vol. 35, nos. 11–12, pp. 1677–1699, 1990, doi: 10.1016/0013-4686(90)87067-C.
- [21] R. Memming, *Semiconductor Electrochemistry*. Hoboken, NJ, USA: Wiley, 2008, doi: 10.1002/9783527613069.
- [22] F. A. Grant, "Properties of rutile (titanium dioxide)," *Rev. Mod. Phys.*, vol. 36, pp. 646–674, Jul. 1959, doi: 10.1103/RevModPhys.31.646.
- [23] L. Chang, T. Breuninger, and T. Euler, "Chromatic coding from cone-type unselective circuits in the mouse retina," *Neuron*, vol. 77, no. 3, pp. 559–571, 2013. [Online]. Available: <http://dx.doi.org/10.1016/j.neuron.2012.12.012>
- [24] C. Leibig, T. Wachtler, and G. Zeck, "Unsupervised neural spike sorting for high-density microelectrode arrays with convolutive independent component analysis," *J. Neurosci. Methods*, vol. 271, pp. 1–13, Sep. 2016, doi: 10.1016/j.jneumeth.2016.06.006.
- [25] F. Jetter, G. Bertotti, R. Thewes, and G. Zeck, "Wavelength-sensitivity of mouse retinal ganglion cells recorded by a high-density micro electrode array (MEA)," *Frontiers Neurosci.*, pp. 1–97, Jun. 2016, doi: 10.3389/conf.fnins.2016.93.00097.